INFORMATION TO USERS

The most advanced technology has been used to photograph and reproduce this manuscript from the microfilm master. UMI films the original text directly from the copy submitted. Thus, some dissertation copies are in typewriter face, while others may be from a computer printer.

In the unlikely event that the author did not send UMI a complete manuscript and there are missing pages, these will be noted. Also, if unauthorized copyrighted material had to be removed, a note will indicate the deletion.

Oversize materials (e.g., maps, drawings, charts) are reproduced by sectioning the original, beginning at the upper left-hand corner and continuing from left to right in equal sections with small overlaps. Each oversize page is available as one exposure on a standard 35 mm slide or as a 17" × 23" black and white photographic print for an additional charge.

Photographs included in the original manuscript have been reproduced xerographically in this copy. 35 mm slides or 6" × 9" black and white photographic prints are available for any photographs or illustrations appearing in this copy for an additional charge. Contact UMI directly to order.

Electron transport and optical emissions in the aurora

Lummerzheim, Dirk, Ph.D.

University of Alaska Fairbanks, 1987

PLEASE NOTE:

In all cases this material has been filmed in the best possible way from the available copy. Problems encountered with this document have been identified here with a check mark __√__.

1. Glossy photographs or pages _____

2. Colored illustrations, paper or print _____

3. Photographs with dark background __✓__

4. Illustrations are poor copy _____

5. Pages with black marks, not original copy _____

6. Print shows through as there is text on both sides of page _____

7. Indistinct, broken or small print on several pages __✓__

8. Print exceeds margin requirements _____

9. Tightly bound copy with print lost in spine _____

10. Computer printout pages with indistinct print _____

11. Page(s) _____ lacking when material received, and not available from school or author.

12. Page(s) _____ seem to be missing in numbering only as text follows.

13. Two pages numbered _____. Text follows.

14. Curling and wrinkled pages _____

15. Dissertation contains pages with print at a slant, filmed as received __✓__

16. Other_____

_____

_____

U·M·I

ELECTRON TRANSPORT AND OPTICAL EMISSIONS

IN THE AURORA

A

THESIS

Presented to the Faculty of the University of Alaska

in Partial Fulfillment of the Requirements

for the Degree of

DOCTOR OF PHILOSOPHY

By

Dirk Lummerzheim, Dipl. Geophys.

Fairbanks, Alaska

December 1987

ELECTRON TRANSPORT AND OPTICAL EMISSIONS

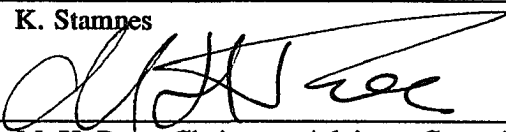# IN THE AURORA

by

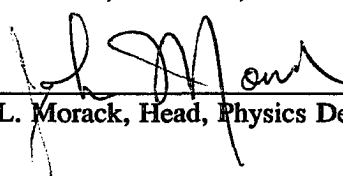Dirk Lummerzheim

RECOMMENDED:
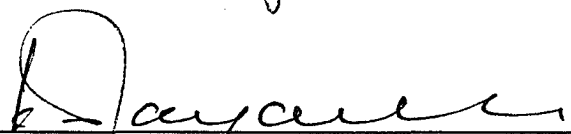
L. C. Lee

J. V. Olson

T. C. Royer

K. Stamnes

M. H. Rees, Chairman, Advisory Committee
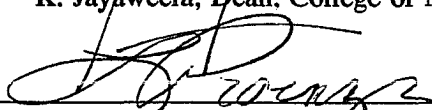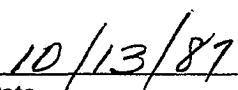
J. L. Morack, Head, Physics Department

APPROVED:

K. Jayaweera, Dean, College of Natural Sciences

L. Proenza, Dean of the Graduate School

10/13/87

Date

Abstract

A one-dimensional, steady state auroral model is developed based on a linear electron transport calculation. A set of cross sections for electron neutral collisions describing elastic scattering, energy loss, and photon emission is compiled and used in conjunction with a discrete ordinate transport code. Calculated electron intensities are compared with *in situ* rocket measurements. Auroral optical emissions that result from direct electron impact on neutrals are calculated for synthetic and observed electron spectra. A systematic dependence of the brightness of auroral features on energy flux, characteristic energy, and atmospheric composition is found and parameterized. A method for interpreting the brightness and the ratio of brightnesses of certain auroral emissions in terms of the energy flux, characteristic energy, and relative oxygen density is described. Application of this method to auroral images acquired by nadir viewing instruments aboard a satellite is discussed and the distribution of energy flux, characteristic energy, and ionospheric conductances over the auroral oval is determined. Emissions that are suitable for analysing auroral spectra in terms of the atomic oxygen abundance in the auroral zone are identified.

Table of Contents

List of Figures

List of Tables

Acknowledgments

The research underlying this thesis and completion of the work was only possible because of the steady advice and encouragement of the chairman of my advisory committee, Prof. M. H. Rees. Combining guidance with patience and a long leash, he allowed me as much freedom as I wished, yet directed me through the maze of auroral physics. Not only did he support my struggling with this research project, he also encouraged me and gave me ample opportunity to interact with scientists in other parts of the world. Working with him made my stay in Alaska most rewarding.

Prof. K. Stamnes of Tromsø University provided much help with the construction and implementation of the numerical scheme that was used to solve the transport equation. He also acted as a kind host when I spent a month in Tromsø to iron out some remaining numerical problems.

Many thanks are extended to the members of my advisory committee, Profs. L. C. Lee, J. V. Olson, and T. C. Royer. Last not least I want to thank the students and staff of the Geophysical Institute for their help with numerous problems and discussions which were not exclusively related to the problems addressed in this thesis: Ghee Fry, Mark Mandt, Bob Sica, Rodney Viereck, Channon Price, who advanced to Assistant Professor in the Physics Department, Jim Baldridge, Cliff Moore, and Debi Lee Wilkenson. Dick Million and Celia Rohwer assisted me with advice on numerical problems. The names are too numerous to list them all.

Profs. L. A. Frank and J. D. Craven of the Dynamics Explorer team (University of Iowa) kindly provided me with images from the DE-satellite, and Prof. J. D. Winningham (Southwest Research Institute) sent electron spectra taken by the DE-satellite. Prof. H. R. Anderson (Science Application International) made the data from the sounding rocket flight 29.007 available.

The computations were preformed on the computers of the Geophysical Institute (VAX 780 and VAX 785) and of the University of Alaska (VAX 8800). The manuscript was typeset with TEX. Financial support came from NSF grants ATM 87 01192 and ATM 83 12883 and the Geophysical Institute Graduate Student Travel Fund.

Hofstadter's Law: It always takes longer than you expect, even

when you take into account Hofstadter's Law

Hofstadter, 1980
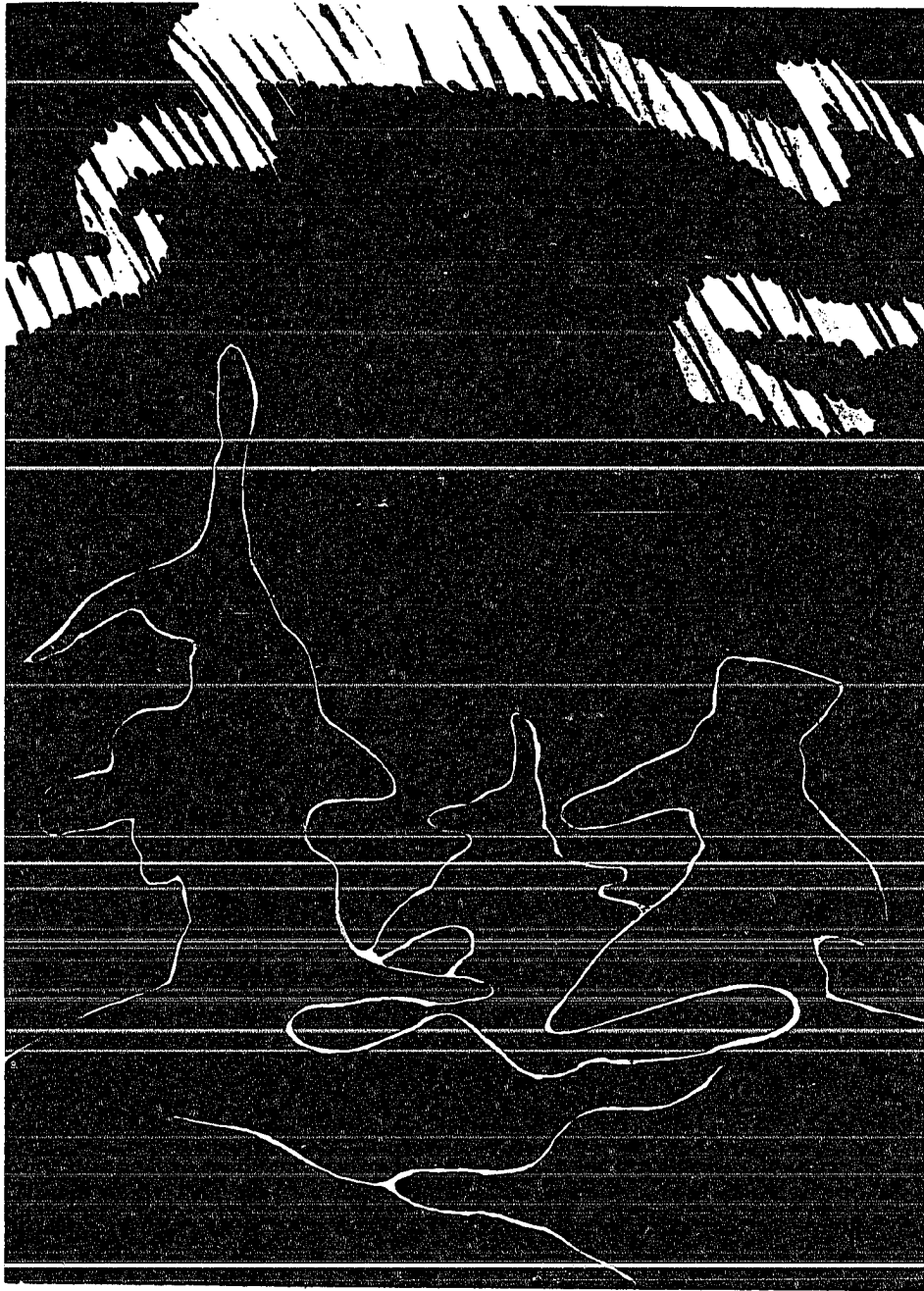
JILL BACKUS © 1987

Chapter 1. Introduction

Observations of the aurora date back to the first century A.D. when Seneca described flames with changing colors in the sky over southern Europe (Störmer, 1955). Gauss hypothesized a dependence of the aurora on the earth's magnetic field but only the discovery of the electron by J. J. Thompson in 1897 led to the understanding of the aurora as the radiant manifestation of energetic particles penetrating into the atmosphere. A breakthrough in modelling auroral processes occurred when Birkeland combined the ideas of previous investigators and conducted his terrella experiments (Birkeland, 1901). The terrella experiments were successful in explaining the general morphology of the aurora. The development of auroral physics required contributions from a large number of disciplines, including the study of solar phenomena, solar wind in the interplanetary space, magnetospheric phenomena, and processes in the upper atmosphere.

Some aspects of the last step in the chain of events from the initial energy release on the sun to the energy deposition in the atmosphere that leads to the formation of the aurora will be considered in this thesis.

Spectral emissions in an aurora originate from excited states produced by particle impact on the neutral atoms and molecules as well as by chemical reactions. Precipitating electrons constitute the major energy source for the visible aurora. Electron and proton precipitation can be distinguished by their spectroscopic signature, because the protons are converted to excited hydrogen atoms by electron capture giving rise to hydrogen emission lines. Eather and Mende (1972) used the H_β emission to study the morphology of the proton and electron precipitation. Discrete auroral arcs are caused by electrons while the proton aurora is associated with diffuse luminosity. The present work is limited to the study of the electron aurora. The first question posed is: how do energetic electrons from

1

an unspecified source penetrate into the atmosphere and what optical emissions result during this process?

Relating the brightness and the ratio of brightnesses of different emissions to the characteristics of the precipitating electrons was pioneered by Rees (e.g. Rees, 1959; Rees 1963; Rees and Luckey, 1974; Rees and Roble, 1987) and Vallance Jones (e.g. Gattinger and Vallance Jones, 1972; Vallance Jones, 1974). Model calculations and combined particle and optical observations (Kasting and Hays, 1977; Rees and Abreu, 1984) reveal a systematic dependence of the brightness of emissions on the energy flux and the mean energy of the precipitating electrons. The approaches to model this relationship are based on electron transport calculations which yield the electron intensity as a function of altitude and energy. With the electron intensity, the volume emission rates of emissions that result from direct electron impact on neutrals can be calculated, provided the relevant emission cross sections and neutral densities are known.

Most electron transport calculations are applied to the study of the effects of photoelectrons on the ionosphere. Auroral electrons have a much larger energy than photoelectrons so that photoelectron transport results are not easily transferred to auroral applications. The transport calculation can be carried out using a Monte Carlo simulation (Berger et al., 1970) or by solving the transport equation numerically. Banks and Nagy (1970) and Nagy and Banks (1970) developed a two-stream transport code for photoelectrons which they extended to higher energies to include auroral electrons (Banks et al., 1974). In this method the electron intensity is divided into an upstreaming and a downstreaming component. At low energies (below 500 eV) discrete energy losses in excitation and ionization processes are taken into account, while at high energies a continuous energy loss is described by a Fokker-Planck diffusion equation.

A different approach is taken by Strickland and Kepple (1974), who solve the transport equation as a function of energy, altitude, and pitch angle. Approximating the intensity

by analytic functions over the intervals of a discrete computational grid in energy and pitch angle, they arrive at a set of differential equations with altitude as the independent variable and coefficients that depend on energy and pitch angle. This set of differential equations is solved using a second order predictor-corrector scheme. An improvement of this method was achieved by a refinement of the piecewise analytical representation of the intensity (Strickland *et al.*, 1976).

Recognizing the formal equivalence of the electron transport equation to the radiative transfer equation, Stamnes (1977, 1980) developed an alternative numerical method to solve the electron transport equation. The work of Stamnes and his co-workers (see Chapter 3.3) forms the basis for the electron transport code that is developed in the present work.

Common to all approaches for solving the electron transport and energy degradation of electrons in the atmosphere is a need for knowledge of the densities and collision cross sections. Some of the early work on electron transport used analytic approximations for the cross sections for electron neutral collisions (Green and Stolarski, 1972), but in the present model laboratory measurements are adopted, if available.

Empirical density models are available that specify the density of the individual neutral species and the temperature as a function of altitude in the upper atmosphere. The model of Jacchia (1977) calculates the densities for a given exospheric temperature, while the MSIS (Mass Spectrometer and Incoherent Scatter) model (Hedin, 1983; 1986), which is based on incoherent scatter radar and satellite measurements, calculates the densities for a given location, time, and solar activity.

These density models are suitable for describing average and global conditions but fail to account for localized changes in the density and temperature that are induced by the aurora. One of the objectives of this thesis is therefore to establish a procedure by which the inversion of the previously stated "forward problem" is made possible: how can

characteristics of the precipitating electrons and neutral densities in the upper atmosphere be inferred from observed brightnesses of auroral emissions?

In order to provide a tool for the interpretation of auroral optical observations an electron transport equation is derived in Chapter 2. No time lags occur in the electron transport and excitation process in the aurora, and the energetic electrons are guided by the geomagnetic field. A one-dimensional steady state transport equation is therefore an adequate basis for an auroral model. A set of cross sections for elastic scattering and excitation and ionization by electron impact is compiled from a large number of sources.

The procedure for solving the simplified electron transport and energy degradation equation is described in Chapter 3. A two-stream method is discussed, but emphasis is placed on the multi-stream method which solves the transport equation for the electron intensity as a function of altitude, energy, and pitch angle. Electron intensity data from a sounding rocket that traversed through an auroral arc are compared to the results of the transport calculations.

The auroral model is completed by the calculation of optical emissions in Chapter 4. The incident electron spectrum and the density model are parameterized, and the parameters can be inferred from the brightness of auroral emissions. This inversion is applied to satellite images of the auroral oval to infer the energy flux into the atmosphere, the characteristic energy of the precipitating electrons, and ionospheric conductances. Two examples of an interpretation of ground based optical observations are also discussed and the possibility for inferring the density of atomic oxygen is outlined.

Chapter 5 contains a summary of the thesis and some concluding remarks. The evaluation of the energy degradation function on a discrete energy grid and some details of the derivation of the two-stream differential equation are provided in the appendices.

The units that are adopted throughout the thesis are the Gaussian cgs units which are most commonly used in the field of aeronomy. Wavelengths are given in Ångstrom

$(1\text{Å} = 10^{-10}\text{m})$, number densities are measured in cm^{-3}, and energy flux density is measured in $\text{erg cm}^{-2}\text{sec}^{-1}$ ($1\text{ erg cm}^{-2}\text{sec}^{-1} = 10^{-3}\text{ Wm}^{-2}$).

Chapter 2. Transport Equation

2.1 Derivation of the Electron Transport Equation

A transport equation is the mathematical formulation of the transport of particles through matter. It can, among other possibilities, be derived from the Liouville equation. For most transport phenomena it is sufficient to describe the state of a particle by its position and velocity. The internal state (spin etc.) usually does not contribute to the motion of freely streaming particles between collisions, and can be neglected. For electron transport in the presence of electromagnetic fields the charge of the electron is important but remains constant throughout the transport process. It can therefore be omitted from the characterization of the state of the electron. It suffices to define a distribution function that depends only on phase-space position (location r and velocity v) and time t to describe N streaming electrons

$$f_N(\mathbf{r}_1,\ldots,\mathbf{r}_N,\mathbf{v}_1,\ldots,\mathbf{v}_N,t).$$

The Liouville equation states that the distribution function is a constant of the motion, i.e. $df_N/dt = 0$. This equation cannot be solved if one deals with a large number of particles. The BBGKY Hierarchy (Nicholson, 1983) arises from Liouville's equation and expresses the distribution function of a number of particles k in terms of the distribution function for $k + 1$ particles. Closing this hierarchy at the level $k = 1$, with an approximation allowing only paired interaction of particles, i.e. neglecting all three or more body interactions,

6

leads to the Boltzmann equation. Writing f for $f_1(\mathbf{r},\mathbf{v},t)$ gives

$$\frac{df}{dt} = \left(\frac{\delta f}{\delta t}\right)_{\text{coll}}.$$

The Boltzmann collision term on the right hand side describes the changes of the distribution function due to paired collisions. Both sides of this equation will be discussed in detail in the following paragraphs.

By expanding the substantial derivative on the left hand side into the partial derivatives that are contained in dt we arrive at the Boltzmann equation

$$\frac{df}{dt} = \frac{\partial f}{\partial t} + \mathbf{v}\cdot\nabla_r f + \frac{1}{m}\mathbf{F}\cdot\nabla_v f = \left(\frac{\delta f}{\delta t}\right)_{\text{coll}}. \tag{2.1}$$

Here is $\mathbf{v}$ the velocity, $\mathbf{F}$ external forces, m the electron mass and ∇_r, ∇_v are gradient operators which take derivatives with respect to $\mathbf{r}$ and $\mathbf{v}$. The external force $\mathbf{F}$ combines the sum of all electromagnetic and pressure gradient forces. The latter is of no consequence for auroral electron transport and can be neglected. In the absence of macroscopic electric fields and in homogeneous magnetic fields (neglecting the gyration of the electron, i.e. representing it as an imaginary particle at the guiding center) this term reduces to the forces due to microscopic electromagnetic fields that result from an inhomogeneously charged environment. A continuous energy loss from the streaming electrons to the ambient thermal electrons can be included using this term. For the case of an inhomogeneous magnetic field an additional force arises from the convergence of the field (mirror force) which affects the angular behavior of the streaming electrons.

Although the distribution function describes the state of the streaming electrons uniquely it is not directly measurable. Other quantities such as number density and flux density are better suited to describe and understand physical processes. These two observables are given by the first two velocity moments of the distribution function. Thus

they are integrated quantities. In the following treatment intensity, which is a differential analogue to flux density, will be used to describe the electrons.

In order to find the relationship of the intensity to the distribution function, the variable $\mathbf{v}$ is first transformed to the variables kinetic energy E and unity direction vector $\Omega = \mathbf{v}/v$:

$$f(\mathbf{r}, E, \Omega, t) = \frac{v}{m} f(\mathbf{r}, \mathbf{v}, t).$$

Then the intensity is defined by multiplying the distribution function with the velocity analogous to the definition of the flux as the first velocity moment

$$I(\mathbf{r}, E, \Omega, t) = \frac{v^2}{m} f(\mathbf{r}, \mathbf{v}, t). \tag{2.2}$$

This definition of the intensity (Duderstadt and Martin, 1970) is consistent with more descriptive definitions, where the intensity is constructed to be the number of electrons per energy and per time in a unit solid angle, that pass through a unit surface.

For the treatment of auroral electron transport a number of approximations can be made to simplify the non-linear Boltzmann equation in order to arrive at a linear transport equation. The time that it takes auroral electrons to penetrate the collision dominated atmospheric region is small compared to changes in the host medium as a response to electron impact. This justifies assuming a steady state and neglecting explicit time dependence of the distribution function ($\partial f/\partial t = 0$). The geomagnetic field imposes an anisotropy on the motion of electrons. For the field strength and the average mean free path at auroral altitudes the gyrofrequency is much larger than the collision frequency. This allows specifying the motion of an individual electron by the motion of its guiding center. Consequently, the average motion is symmetric with respect to azimuth and one-dimensional along the direction of the magnetic field.

Introducing these approximations into equation (2.1) and replacing the distribution function with the intensity (Eq. 2.2) yields

$$\frac{1}{v}\frac{dI(s,E,\mu)}{dt} = \frac{1}{v}\left(\frac{\delta I}{\delta t}\right)_{coll},$$

where s is a spatial variable along the path of the guiding center and μ is the cosine of the pitch angle, i.e. $ds/dt = \mu v$. Expanding the substantial derivative on the left hand side gives

$$\frac{1}{v}\frac{dI}{dt} = \frac{1}{v}\left(\frac{\partial I}{\partial s}\frac{ds}{dt} + \frac{\partial I}{\partial \mu}\frac{d\mu}{dt} + \frac{\partial I}{\partial E}\frac{dE}{dt}\right). \qquad (2.3)$$

The first term of this expansion becomes

$$\frac{1}{v}\left(\frac{\partial I}{\partial s}\mu v\right) = \mu\frac{\partial I}{\partial s}.$$

Lejeune and Wormser (1976) transformed the second term using the conservation of the first adiabatic invariant $(1 - \mu^2)/B = $ const. so that

$$\frac{\partial \mu}{\partial s} = -\frac{1-\mu^2}{\mu}\frac{1}{2B}\frac{\partial B}{\partial s},$$

then

$$\frac{d\mu}{dt} = \frac{\partial \mu}{\partial s}\frac{ds}{dt} = -\frac{1-\mu^2}{\mu}\frac{1}{2B}\frac{\partial B}{\partial s}\mu v,$$

and the second term becomes

$$\frac{1}{v}\frac{\partial I}{\partial \mu}\frac{d\mu}{dt} = -(1-\mu^2)b(s)\frac{\partial I}{\partial \mu} \qquad \text{with} \qquad b(s) = \frac{1}{2B}\frac{\partial B}{\partial s}.$$

The function $b(s)$ describes the divergence of the magnetic field. For a homogeneous field $b(s) = 0$.

In the absence of macroscopic electric fields the change of momentum is due to interaction of the streaming electrons with the ambient electron gas. This can be approximated

by a continuous energy loss process. With n_e the ambient electron density and $L(E)$ the stopping power the change in momentum is

$$m\frac{\partial \mathbf{v}}{\partial t} = -n_e L(E)\frac{\mathbf{v}}{v}.$$

Stamnes and Rees (1983) have used this approximation to transform the last term of equation (2.3) to

$$-n_e(s)\frac{\partial}{\partial E}\left(L(E)I(s, E, \mu)\right).$$

Collecting all terms, the left hand side of the transport equation reads

$$\frac{1}{v}\frac{dI}{dt} = \mu\frac{\partial I}{\partial s} - (1 - \mu^2)b(s)\frac{\partial I}{\partial \mu} - n_e\frac{\partial (L\,I)}{\partial E}. \tag{2.4}$$

The right hand side of the Boltzmann equation describes the collisional interaction of the streaming electrons with the atmospheric environment. This includes excitation, ionization and elastic collisions with neutrals. The ion densities are sufficiently small to allow neglecting electron-ion collisions. Also neglected are electron-neutral attachment and superelastic collisions because the collision rates are small. Photoionization gives rise to additional streaming electrons, which can be included as an internal source. The Boltzmann collision term is the sum of these terms:

$$\left(\frac{\delta f}{\delta t}\right)_{\text{coll}} = \left(\frac{\delta f}{\delta t}\right)_{\text{e-nel}} + \left(\frac{\delta f}{\delta t}\right)_{\text{e-nex}} + \left(\frac{\delta f}{\delta t}\right)_{\text{e-nion}} + Q_{\text{Photo}}.$$

In general, a collision term consists of two parts describing the loss of a particle from a point in phase-space and the recreation of this particle at another point in phase-space. In a collision the momentum of the particle changes so that the transition in phase-space is $(\mathbf{r},\mathbf{v}) \rightarrow (\mathbf{r},\mathbf{v}')$. If $\Sigma(\mathbf{r},\mathbf{v})\,d^3r\,d^3v$ denotes the probability for a particle interaction per unit distance traveled by an electron from the phase-space volume $d^3r\,d^3v$ around $(\mathbf{r},\mathbf{v})$, the loss of particles from this phase-space volume is $J = v\Sigma(\mathbf{r},\mathbf{v})f(\mathbf{r},\mathbf{v})$. The phase function

$p(\mathbf{v} \rightarrow \mathbf{v'})\, d^3v$ is defined as the probability of emitting secondary particles with velocity $\mathbf{v'}$ from an incident particle at velocity $\mathbf{v}$ (Duderstadt and Martin, 1979). The number of secondary particles emitted in such a process is $c(\mathbf{r},\mathbf{v})$. For an excitation collision or an elastic collision $c = 1$ and for ionization $\int c(\mathbf{r},\mathbf{v}) d^3v = 2$. With these definitions the collision term can be written as

$$\left(\frac{\delta f}{\delta t}\right)_{\text{coll}} = Q - J = \int v'\Sigma(\mathbf{r},\mathbf{v'}) p(\mathbf{v'} \rightarrow \mathbf{v}) c(\mathbf{r},\mathbf{v}) f(\mathbf{r},\mathbf{v'})\, d^3v' - v\Sigma(\mathbf{r},\mathbf{v}) f(\mathbf{r},\mathbf{v}).$$

An expression for Σ in terms of the microscopic cross section σ is $\Sigma(\mathbf{r},\mathbf{v}) = n(\mathbf{r})\sigma(\mathbf{v})$ with $n(\mathbf{r})$ the density of the ambient medium. Assuming that the collision frequency is independent of the direction of the incident particle, the cross sections become a function of energy

$$\Sigma(\mathbf{r},\mathbf{v}) = n(\mathbf{r})\sigma(|\mathbf{v}|) \rightarrow \begin{cases} n(\mathbf{r})\sigma^{\text{el}}(E) & \text{elastic} \\ n(\mathbf{r})\sigma^{\text{ex}}(E) & \text{excitation} \\ n(\mathbf{r})\sigma^{\text{ion}}(E) & \text{ionization.} \end{cases}$$

The sum of the loss terms is then

$$J = n(\mathbf{r})\sigma^{\text{tot}}(E)\frac{m}{v} I(\mathbf{r}, E, \mu),$$

where $\sigma^{\text{tot}}(E)$ is the sum of all cross sections.

In the following the collision integral for the source term Q will be specified for the three processes under consideration. The variables will be changed from $\mathbf{v}$ to (E,μ) and the intensity is introduced according to equation (2.2).

For elastic collisions with cross section $\sigma^{\text{el}}(E)$ the collision kernel becomes

$$\Sigma(\mathbf{r},\mathbf{v'})p_{\text{el}}(\mathbf{v'} \rightarrow \mathbf{v})c(\mathbf{r},\mathbf{v}) = n(\mathbf{r})\sigma^{\text{el}}(E')p_{\text{el}}(\mu' \rightarrow \mu)\delta(E' - E).$$

The Dirac delta function $\delta(E' - E)$ arises from the assumption that the collision partners have a much larger mass than the electrons and can be treated as stationary so that no

energy transfer due to recoil between the atom or molecule and the electron occurs. After integrating over energy the elastic collision term becomes

$$\frac{v}{m}\left(\frac{\delta f}{\delta t}\right)_{\text{el}} = n(\mathbf{r})\sigma^{\text{el}}(E)\int p_{\text{el}}(\mu' \rightarrow \mu)I(\mathbf{r}, E, \mu')\,d\mu' - n(\mathbf{r})\sigma^{\text{el}}(E)I(\mathbf{r}, E, \mu).$$

In excitation collisions with cross section $\sigma^{\text{ex}}(E)$ the incident particle loses the energy W. The collision kernel has the same structure as for an elastic collision. The energy loss is described by a δ-function $\delta(E' - (E + W))$ and the angular redistribution is characterized by a phase function $p_{\text{ex}}(\mu' \rightarrow \mu)$. The integration over energy can immediately be carried out and the collision integral becomes

$$\frac{v}{m}\left(\frac{\delta f}{\delta t}\right)_{\text{ex}} = n(\mathbf{r})\sigma^{\text{ex}}(E+W)\int p_{\text{ex}}(\mu' \rightarrow \mu)I(\mathbf{r}, E+W, \mu')\,d\mu' - n(\mathbf{r})\sigma^{\text{ex}}(E)I(\mathbf{r}, E, \mu).$$

The first term describes the gain of electrons at energy E due to scattering from electrons at energy $E' = E + W$, while the second term represents the loss of electrons with energy E.

In the case of an ionizing collision with cross section $\sigma^{\text{ion}}(E)$ there is one electron lost per unit path length $n(\mathbf{r})\sigma^{\text{ion}}(E)$ and two electrons are created at lower energies. These two electrons emerge with energies E_d and E_s governed by $\sigma^{\text{deg}}(E' \rightarrow E_d)$ and $\sigma^{\text{sec}}(E' \rightarrow E_s)$ (for degraded and secondary) and the collision kernel becomes

$$n(\mathbf{r})\sigma^{\text{deg}}(E' \rightarrow E_d)p_{\text{deg}}(\mu' \rightarrow \mu) + n(\mathbf{r})\sigma^{\text{sec}}(E' \rightarrow E_s)p_{\text{sec}}(\mu' \rightarrow \mu).$$

The production cross sections σ^{deg} and σ^{sec} are normalized to the total ionization cross section σ^{ion}

$$\int \sigma^{\text{deg}}(E' \rightarrow E)\,dE = \sigma^{\text{ion}}(E')$$

$$\int \sigma^{\text{sec}}(E' \rightarrow E)\,dE = \sigma^{\text{ion}}(E'). \tag{2.5}$$

To shorten the notation, the source terms for the various processes are denoted by Q_{el}, Q_{ex} and Q_{ion} and the sum of all loss cross sections by $\sigma^{tot}(E)$. Then the right hand side of the Boltzmann equation becomes

$$\frac{v}{m}\left(\frac{\delta f}{\delta t}\right)_{coll} = -n(\mathbf{r})\sigma^{tot}(E)I(\mathbf{r}, E, \mu) + Q_{el} + Q_{ex} + Q_{ion}.$$

Together with equation (2.4) this establishes the general one-dimensional linear transport equation for electrons:

$$\mu\frac{\partial I}{\partial s} - (1-\mu^2)b(s)\frac{\partial I}{\partial \mu} - n_e\frac{\partial(LI)}{\partial E} = -n\sigma^{tot}I + Q_{el} + Q_{ex} + Q_{ion} + Q_{Photo}. \qquad (2.6)$$

To solve this equation the cross sections, phase functions, and the loss-function $L(E)$ need to be specified.

2.2 Cross sections

Electron impact cross sections of the main constituents of the neutral atmosphere are essential input parameters for the transport equation. To analyse scattering alone, the total cross sections of the species are sufficient. Electron transport, however, depends on energy degradation which requires detailed knowledge of the cross sections and associated energy losses of each individual excited state of the atom or molecule.

An extensive compilation of cross sections and phase functions for elastic scattering of electrons with the three major constituents N_2, O_2, and O is given by Wedde (1976). To extend these cross sections to higher energies Wedde and Strand (1974) inferred an energy dependence proportional to $E^{-0.65}$ with E measured in eV. The cross sections for H and He are summarized by Takayanagi and Itikawa (1970), and are extrapolated to higher energies using the measurements by Wingerden et al. (1977) for hydrogen and de Heer and Jansen (1977) for helium.

Using a two-stream approximation to solve the transport equation for the energy range of photoelectrons (0.5 to 100 eV) Stamnes and Rees (1983) computed the electron heating rate resulting from adopting several sets of cross sections. They concluded that a set, which was compiled by Phelps (see Pitchford and Phelps, 1982) and included cross sections for elastic scattering, excitation, and ionization of N_2 and O_2, was best suited for their purpose. The same set was also adopted for this work with some modifications. This set is based on experimental data as well as theoretical work. References for the cross sections are summarized in Table 1 at the end of this chapter.

Cross sections for the excitation of the triplet states of N_2 ($A^3\Sigma_u^+$, $B^3\Pi_g$, $W^3\Delta_u$, and $C^3\Pi_u$) were measured by Cartwright et al. (1977). Tachibana and Phelps (1979) recommend scaling the cross sections for the A, B, and W triplet states by a factor of 0.8 and using the data for the C state unscaled. Dissociation of N_2 by electron impact is the major source of atomic nitrogen. The singlet predissociation states are lumped together into one cross section that equals the total N_2 dissociation cross section, with a common averaged energy loss (Zipf and McLaughlin, 1978). Since a recent measurement for the $a^1\Pi_g$ state is available, the results of Ajello and Shemansky (1985) are substituted into the Phelps set. In spite of their small cross section the processes that lead to the excited ion states $N^+(^3F)$ and $N^+(^3D_3)$ via $N_2 + e^- \rightarrow N_2^{+*} + 2e^-$ are included in the set. These states give rise to 5001 Å and 5680 Å radiation, both of which are observed in the aurora. The cross sections are almost identical in shape and are lumped together (Filippelli et al., 1982). Fig. 2.1a shows the individual excitation cross sections as a function of the impact energy and Fig. 2.2a displays the sum of all excitation together with the ionization, vibration, and elastic cross sections.

The total ionization cross section is taken from measurements by Rapp and Englander-Golden (1965) and Märk (1975). For a correct treatment of the energy degradation it is necessary to account for ions that are left in excited states after the collision. The

15
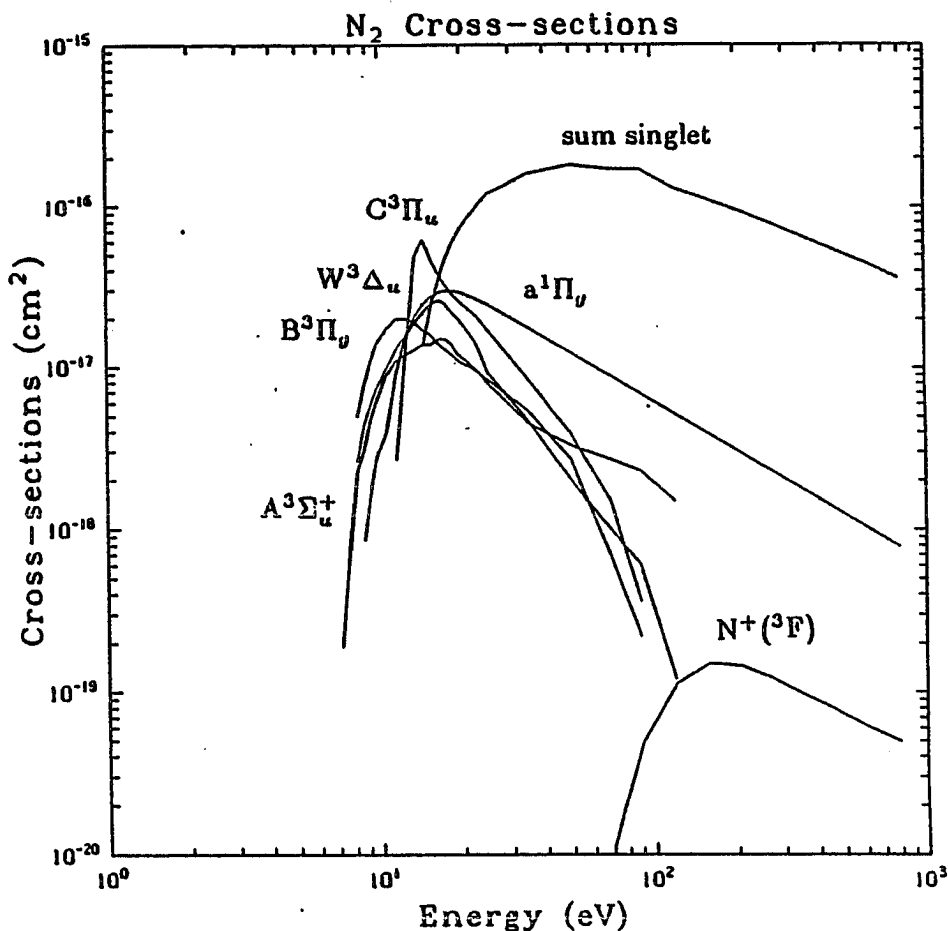
Fig. 2.1a Excitation cross sections of N_2 as a function of electron impact energy.

energy dependence of a cross section for an excited ion state is nearly the same as for total ionization, with some deviation near threshold. It can therefore be represented by the total ionization cross section and a proper branching ratio (see Table 2). Besides the ground state $N_2^+(X^2\Sigma_g^+)$, two excited states are considered. The branching ratios are based on measurements of optical emissions of the Meinel band for the $N_2^+(A^2\Pi_u)$ (Holland and Maier, 1972) and the first negative band for the $N_2^+(B^2\Sigma_g^+)$ (Borst and Zipf, 1970).

The cross sections for the excitation of the O_2 singlet states $a^1\Delta_g$ and $b^1\Sigma_g^+$ are taken from Trajmar et al. (1971), whose measurements are supported by the results of Linder and Schmidt (1971). Four more non-ionizing cross sections are included in the

Reproduced with permission of the copyright owner. Further reproduction prohibited without permission.
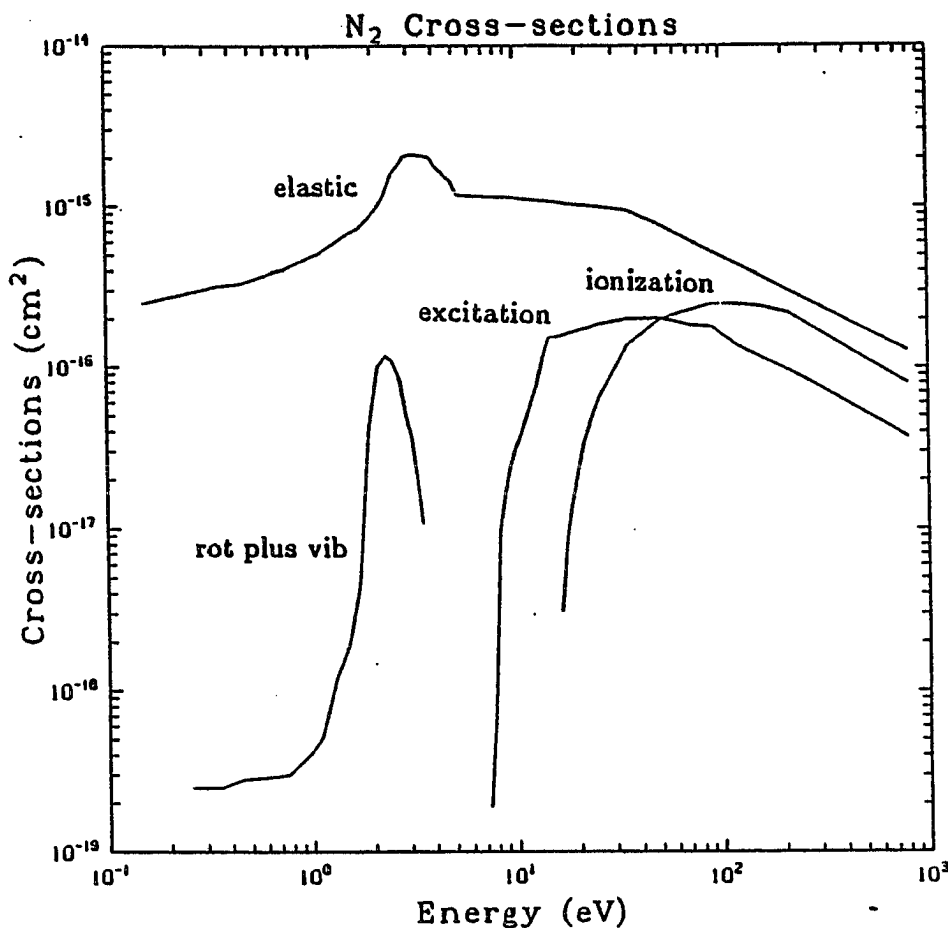
N₂ Cross-sections

Fig. 2.2a Elastic, ionization, vibrational excitation, and the sum of all excitation cross sections of N₂ as a function of electron impact energy.

Phelps set, which are identified by their energy losses: 4.5, 6, 8.4, and 9.97 eV (Hake and Phelps, 1977 and Lawton and Phelps, 1978). Since the dissociation potential for O_2 is only 5.12 eV (as compared to 9.76 eV for N_2) most of these processes lead to excitation followed by dissociation. The 4.5 eV and 6 eV energy losses are associated with the excitation of the $A^3\Sigma_u^+$ and $c^1\Sigma_u^-$ states which lead to the Herzberg I and II continuum emissions and the dissociation of $O_2 \rightarrow O(^3P)+O(^3P)$. The Herzberg continuum, however, is not observed in the auroral spectrum. Trajmar $et\ al.$ (1972) identify the 8.4 eV cross section to be mostly due to the $X^3\Sigma_g \rightarrow B^3\Sigma_u^-$ transition and the subsequent dissociation
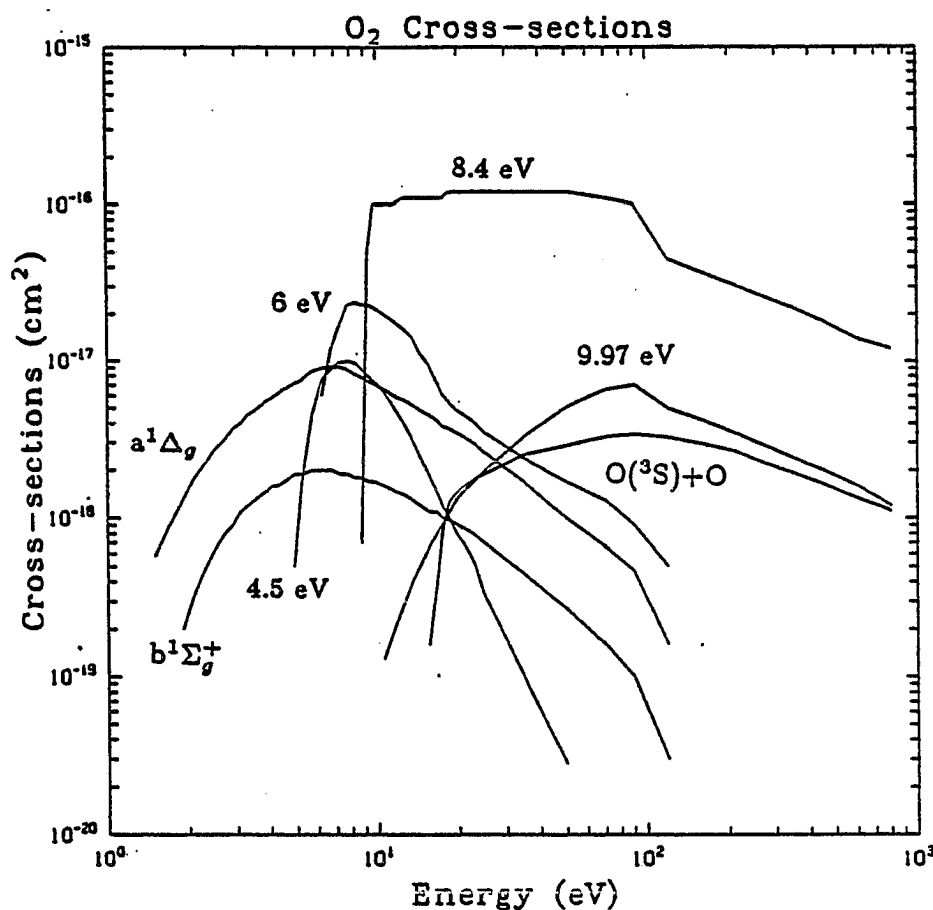
Fig. 2.1b Excitation cross sections of O_2 as a function of electron impact energy.

$O_2 \rightarrow O(^3P) + O(^1D)$. The Schumann-Runge continuum that originates from $O_2(B^3\Sigma_u^-)$ is, like the Herzberg emission, not observed in the aurora. Although the 9.97 eV transition has a sharply defined energy loss, it is not clearly identified. Trajmar et al. (1972) suggest that it yields $O(^1S)$ as a final dissociation product.

Because of its contribution to the emission of the OI 1304 Å triplet the dissociative process $O_2 \rightarrow O(^3S) + O$ is also included, with the cross section taken from Ajello (1971). The O_2 ionization cross section in the Phelps set comes from Rapp and Englander-Golden (1965). The cross sections for the excited ion states are specified by branching ratios for five ion states (Watson et al., 1967), analogous to the procedure adopted for N_2.
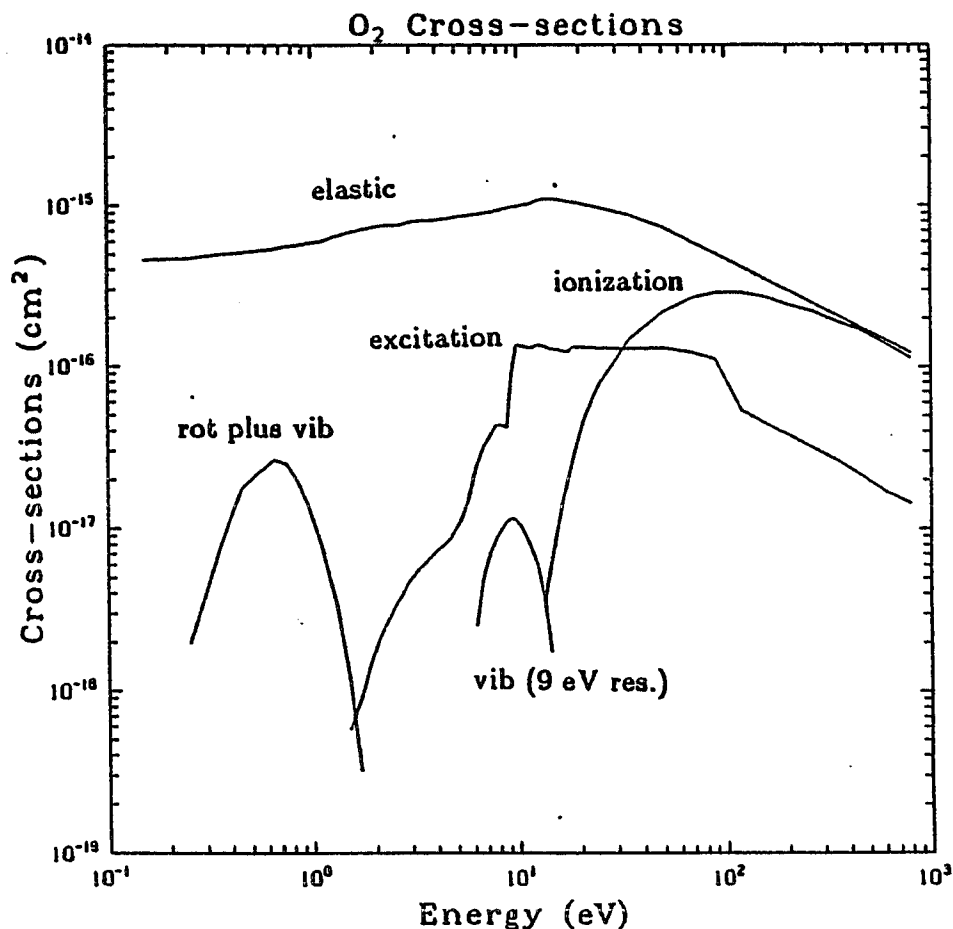
Fig. 2.2b Elastic, ionization, vibrational excitation, and the sum of all excitation cross sections of O_2 as a function of electron impact energy.

For atomic oxygen a set of excitation cross sections is not as readily available. Many authors (Nagy *et al.*, 1969; Banks *et al.*, 1974; Stamnes and Rees, 1983) rely on semi-empirical formulas for the cross sections, like the one given by Green and Stolarski (1972). In this work the $O(^1D)$ excitation cross section is represented by Green and Stolarski's formula, which is in good agreement with the experimental results of Shyn and Sharp (1986). The measurements of the cross section for excitation of $O(^1S)$ (Shyn *et al.*, 1986) suggest that Green and Stolarski's cross section, which is based on theoretical calculations, has to be multiplied by a factor of two. Green and Stolarski also specify three cross sections
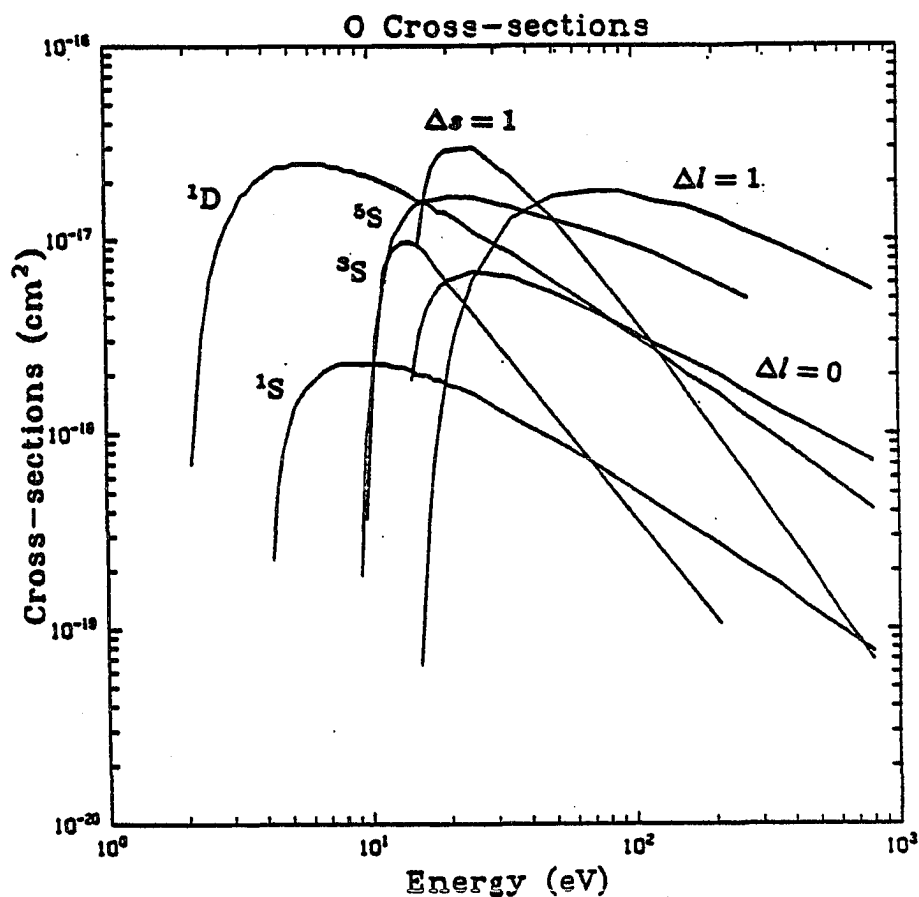
Fig. 2.1c Excitation cross sections of O as a function of electron impact energy.

which are identified by the change of angular momentum of the corresponding transition, with energy losses of 13.5, 14.2, and 14.7 eV. Cross sections for the excitation of the ^{3}S and ^{5}S states were measured by Stone and Zipf (1974). According to a recent study (Zipf and Erdman, 1985) a revision of the 1974 measurements is necessary by scaling them by a factor of 0.34. The ionization cross section is based on a semi-empirical formula by Banks *et al.* (1974), with the branching ratios into different excited ion states given by Burnett and Rountree (1979) (see Table 2). The excitation cross sections for molecular and atomic oxygen are displayed in Fig. 2.1b and c and their sum, together with the ionization and elastic cross section, in Fig. 2.2b and c.
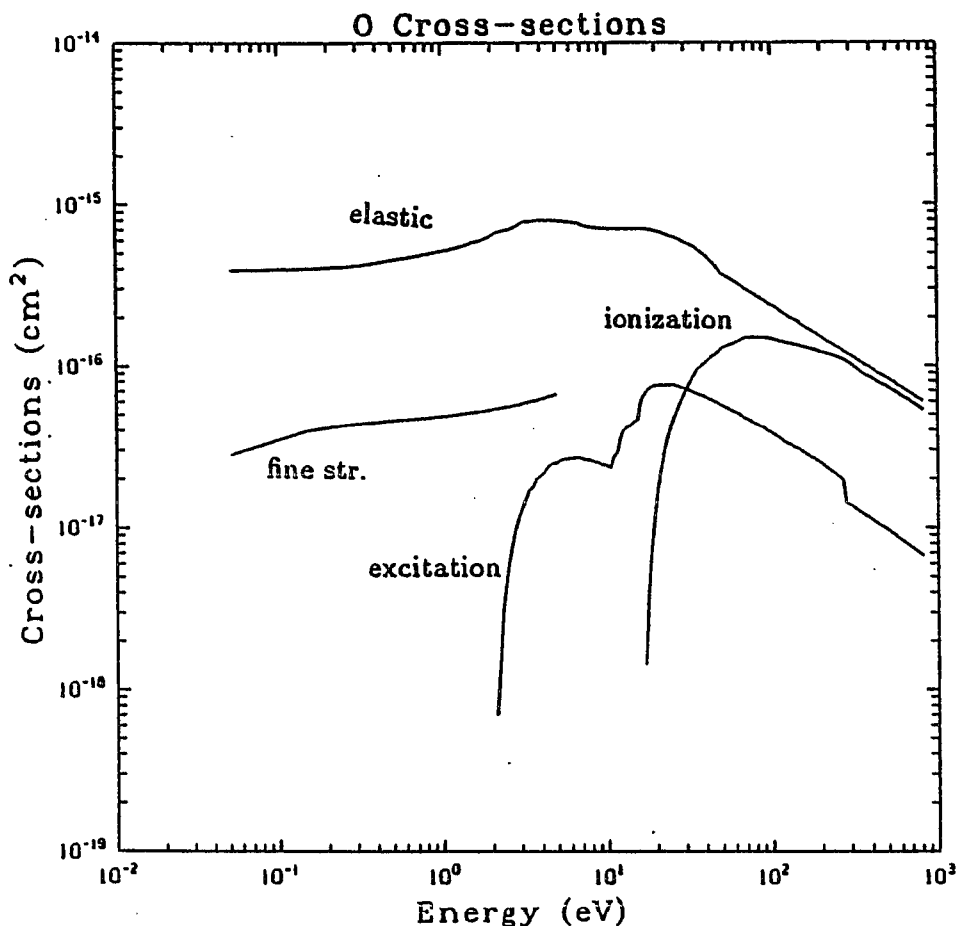
O Cross−sections

Fig. 2.2c Elastic, ionization, fine structure excitation, and the sum of all excitation cross sections of O as a function of electron impact energy.

The most important constituents of the atmosphere from the standpoint of energy degradation of electrons and auroral emissions due to electron impact are N_2, O_2, and O. At high altitude (above 500 km), however, the density of hydrogen and helium become significant. These two species are therefore included in the transport calculation. The hydrogen cross sections are taken from Fite et al. (1959) for the excitation of n=2 (Lyman α) and ionization, and from Mahan et al. (1976) for the excitation of n=3 (Balmer H_α).

The cross sections for helium are taken from de Heer and Jansen (1977) for the 2^1P state, from St.John et al. (1964) for the 3^1P state, from Holt and Krotkov (1966) for the
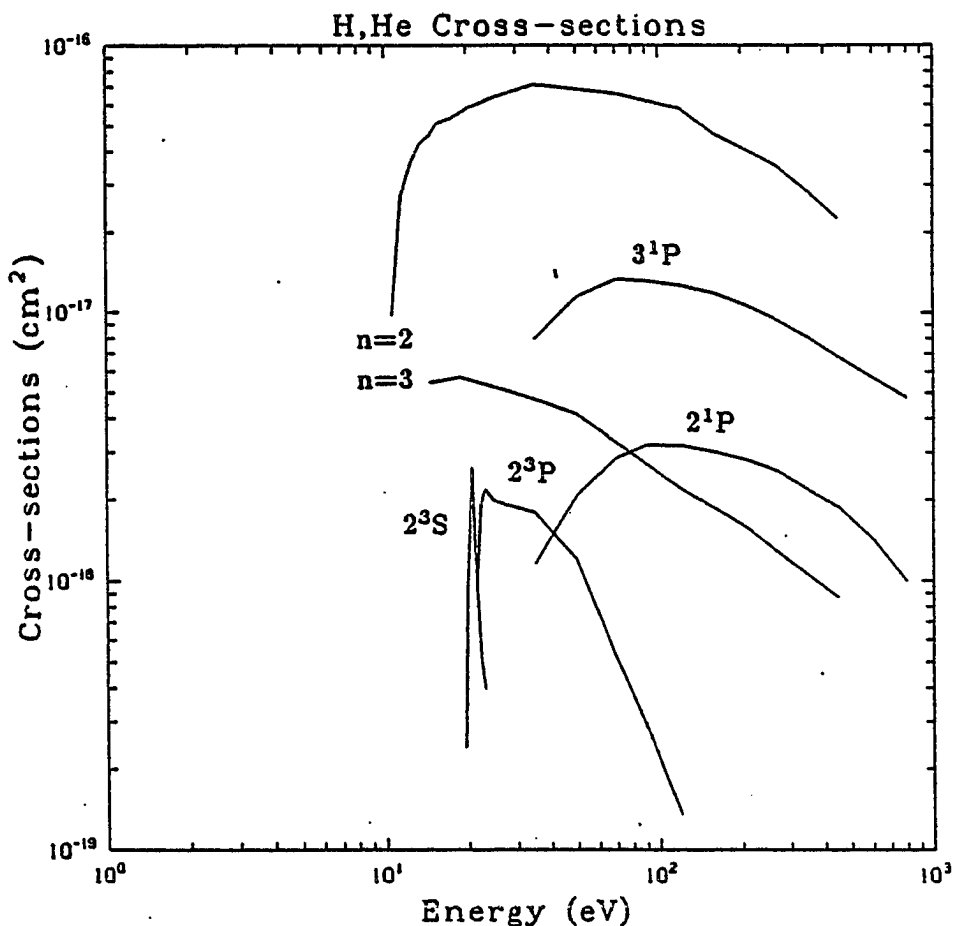
Fig. 2.1d   Excitation cross sections of H and He as a function of electron impact energy.

2^3S state, from Jobe and St.John (1967) for the 2^3P state and from Hasted (1972) for the ionization. To extrapolate the data for the 3^1P state of St.John *et al.* to 1000 eV, the data given by Takayanagi and Itikawa (1970) are used. These cross sections are shown together with the hydrogen cross sections in Fig. 2.1d. Excited ion states are not included for helium.

In addition to the excitation and ionization cross sections, some low energy loss processes are considered: the energy loss due to interaction with the ambient electrons, the rotational and vibrational excitation of the ground states of N_2 and O_2, and the fine structure excitation of O.

In the energy range 0.2 eV to 3.6 eV the rotational and vibrational excitation cross sections of N_2 and O_2 are highly structured (Schulz, 1964; Hake and Phelps, 1967; Linder and Schmidt, 1971). The O_2 ground state vibrational excitation cross sections consist of several sharp peaks (Spence and Schulz, 1970). To resolve these peaks an energy stepsize of the order of 0.01 eV is required. Limitations due to CPU-memory capability prohibit the use of such a fine grid for the transport calculation. It is necessary to interpolate and average these cross sections to a coarser grid with a stepsize of 0.1 eV to 0.5 eV in the energy range below 5 eV. In addition, the rotational and vibrational cross sections are treated as a combined energy loss process.

The interpolated cross sections conserve $\int \sigma \, dE$ for each state after expressing the integral as a sum on a discrete grid. These mean cross sections are shown in Fig. 2.3 for O_2, together with the sum over all states (rotational and $v = 1, 2, 3, 4$). A linear interpolation is used to define the cross section at any point on a given energy grid. The average energy loss W of this lumped cross section is the mean energy loss of the individual states W_v, weighted by the relative integral of the individual cross sections. With $W_{rot} = 0.02$ eV, $W_1 = 0.19$ eV, $W_2 = 0.38$ eV, $W_3 = 0.57$ eV, $W_4 = 0.75$ eV and the cross sections given in Fig. 2.3, the average energy loss becomes $W = 0.24$ eV.

The N_2 rotational and vibrational excitation cross sections are ordered into two groups which are distinguished by their energy loss. The first group combines the rotational and the $v = 1$ excitation with a mean energy loss of 0.29 eV. The remaining vibrational levels, $v = 2$ to $v = 8$, are combined into a group with 1.1 eV energy loss.

The vibrational ground state of O_2 can also be excited by electrons in the 4 to 15 eV energy range via the 9 eV resonance excitation. The energy loss for this process is very small compared to excitation of other states in the same energy range, but is included in the transport calculation because the cross section itself is relatively large. The cross sections for the excitation of the 9 eV resonance were measured by Wong *et al.* (1973).
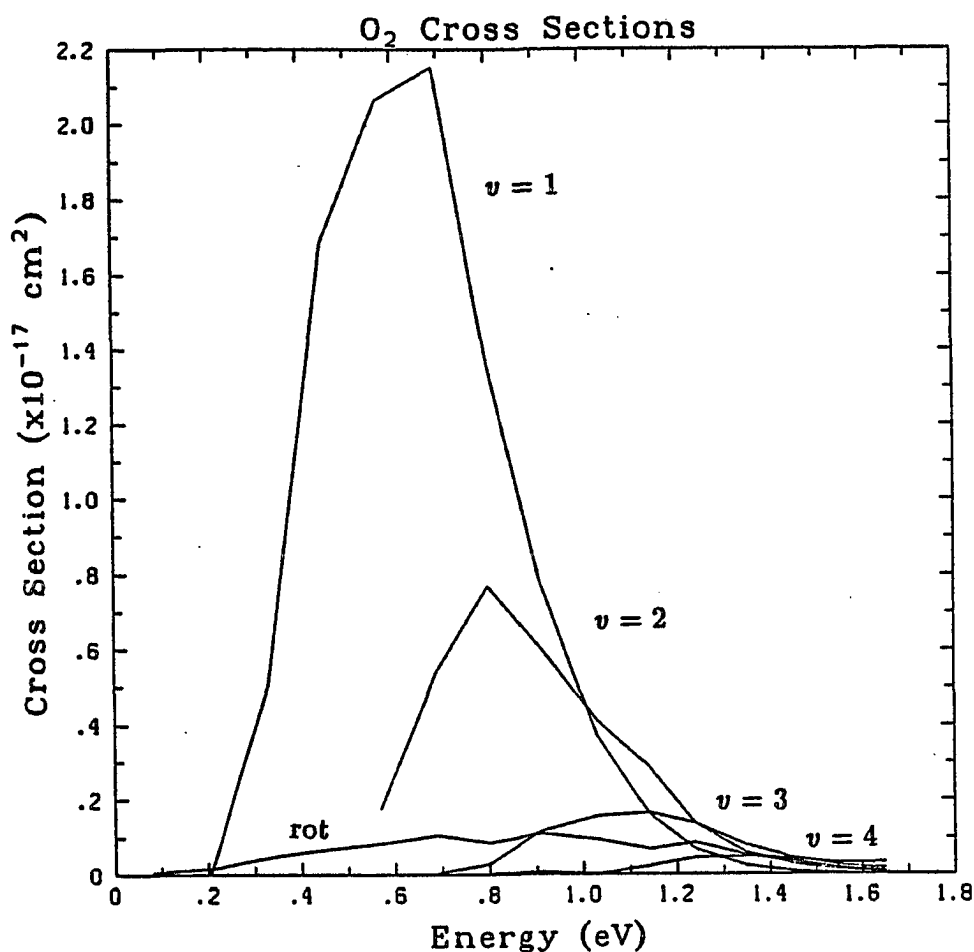
Fig. 2.3 The cross sections for excitation of the ground state vibrational levels $v = 1, 2, 3, 4$ of O_2 after averaging.

They are treated in the same way as the other vibrational excitation cross sections and are combined into a single cross section with an associated energy loss of 0.64 eV.

The atomic oxygen fine structure excitation of the ground state provides a low energy loss process below 2.5 eV. LeDourneuf and Nesbet (1976) give the collision strengths for the three angular momentum transitions $^3P_J \rightarrow {}^3P_{J'}$ for $(J, J') \in (2,1)$, $(2,0)$, $(1,0)$. From these the cross sections can be evaluated (Hoegy, 1976) and combined into a single loss mechanism (Fig. 2.2c). The energy loss of 0.018 eV is calculated in the same manner as for the low energy losses in N_2 and O_2 by a weighted average over the three angular momentum transitions.

A third loss process at very small electron energies arises from the interaction of the streaming electrons with the ambient electron gas. This process represents a continuous energy loss. The loss function given by Aono and Itikawa (1966) is based on collisional interaction and Çerenkov wave generation. Its application is discussed by Schunk and Hays (1971a, 1971b). The rather cumbersome evaluation of Aono and Itikawa's formula can be avoided by adopting an approximate empirical expression given by Swartz *et al.* (1971):

$$L(E) = \frac{3.37 \cdot 10^{-12}}{E^{0.94} n_e^{0.03}} \left(\frac{E - T_e}{E - 0.53\, T_e} \right)^{2.36} . \tag{2.7}$$

Here T_e is the ambient electron temperature in eV, n_e is the electron density in cm^{-3} and E is the energy of the incident electrons in eV. The units of the constant are such that the loss function has units of cm^2eV.

The phase functions, which determine the angular redistribution of electrons in a collision with an atom or molecule, will be discussed in the following chapter, together with their application to the methods of solution for the transport equation.

Table 1

Summary of Electron Impact Cross Sections

Process	Energy Loss (eV)	Cross-section Maximum (cm^2)	Reference
Molecular Nitrogen			
elastic		2.1 (-15)*	Wedde (1976)
rot plus (v=1)	0.171	5.7 (-17)	Schulz (1964)
(v=2...8)	1.102	6.3 (-17)	–"–
$A^3\Sigma_u^+$	7.0	1.5 (-17)	Cartwright et al. (1977)
$B^3\Pi_g$	7.35	2.0 (-17)	–"–
$W^3\Delta_u$	7.36	2.6 (-17)	–"–
$a^1\Pi_g$	8.55	3.0 (-17)	Ajello (1985)
$C^3\Pi_u$	11.03	6.3 (-17)	Cartwright et al. (1977)
sum singlet	13.0	1.8 (-16)	Zipf, McLaughlin (1978)
$N^+(^3F)$	56.5	1.5 (-19)	Filippelli et al. (1982)
ionization	see Tab. 2	2.5 (-16)	Rapp, Englander (1965)
Molecular Oxygen			
elastic		1.1 (-15)	Wedde (1976)
rot plus vib	0.244	2.6 (-17)	Linder, Schmidt (1971)
vib (9 eV res.)	0.635	1.2 (-17)	Wong et al. (1973)
$a^1\Delta_g$	0.977	9.2 (-18)	Trajmar et al. (1971)
$b^1\Sigma_g^+$	1.627	2.0 (-18)	–"–
4.5 eV loss	4.5	1.0 (-17)	Lawton, Phelps (1978)
6 eV loss	6.0	2.4 (-17)	–"–
8.4 eV loss	8.4	1.2 (-16)	Hake, Phelps (1967)
9.97 eV loss	9.97	7.0 (-18)	Trajmar et al. (1972)
$O(^3S)+O$ (diss.)	14.67	3.4 (-18)	Ajello (1971)
ionization	see Tab. 2	2.9 (-16)	Rapp, Englander (1965)

* Read 2.1 (-15) as $2.1 \cdot 10^{-15}$

Table 1 (continued)

Process	Energy Loss (eV)	Cross-section Maximum (cm^2)	Reference
Atomic Oxygen			
elastic		8.0 (-16)	Wedde (1976)
fine str.	0.0178	6.7 (-17)	Hoegy (1976)
^{1}D	1.96	2.5 (-17)	Shyn, Sharp (1986)
^{1}S	4.17	2.3 (-18)	Shyn et al. (1986)
^{5}S	9.15	9.0 (-18)	Stone, Zipf (1973)
^{3}S	9.53	1.8 (-17)	–"–
$\Delta l = 0, \Delta s = 0$	13.5	6.9 (-18)	Green, Stolarsky (1971)
$\Delta l = 1, \Delta s = 0$	14.2	1.8 (-17)	–"–
$\Delta s = 1$	14.7	3.0 (-17)	–"–
ionization	see Tab. 2	1.5 (-16)	Banks et al. (1974)
Hydrogen			
elastic		5.0 (-15)	Takayanagi, Itikawa (1970)
n=2	10.35	7.1 (-17)	Fite et al. (1959)
n=3	13.8	5.7 (-18)	Mahan et al. (1976)
ionization	13.6	7.0 (-17)	Fite, Brackmann (1958)
Helium			
elastic		6.2 (-16)	Takayanagi, Itikawa (1970)
2^{3}S	19.8	2.0 (-18)	Holt, Krotkov (1966)
2^{3}P	20.9	2.1 (-18)	Jobe, St.John (1967)
2^{1}P	21.2	1.3 (-17)	De Heer, Jansen (1977)
3^{1}P	23.1	3.2 (-18)	St.John et al. (1964)
ionization	23.1	3.7 (-18)	Hasted (1972)

Table 2

Branching Ratios for Excited Ion States

Ion State	Energy Loss (eV)	Branching Ratio	Reference
Molecular Nitrogen Ion			
$X^2\Sigma_g^+$	15.58	0.50	Märk (1975)
$A^2\Pi_u$	16.73	0.39	Holland, Maier (1972)
$B^2\Sigma_u^+$	18.75	0.11	Borst, Zipf (1970)
Molecular Oxygen Ion			
$X^2\Pi_g$	12.1	0.25	Watson et al. (1967)
$a^4\Pi_u$	16.1	0.37	—"—
$A^2\Pi_u$	16.9	0.22	—"—
$b^4\Sigma_g^-$	18.2	0.07	Zipf et al. (1985)
$B(^4\Sigma_u,^2\Sigma_g)$	23.0	0.09	Watson et al. (1967)
Atomic Oxyden Ion			
^4S	13.61	0.4	Burnett, Roundtree (1979)
^2D	16.92	0.4	—"—
^2P	18.61	0.2	—"—

Chapter 3. Solution of the Transport Equation

The electron transport equation is a linear integro-differential equation in three variables, s, μ, and E. The assumption that electrons do not gain energy in a collision allows separation of the energy dependence from the transport aspect. Two different approaches will be used to solve the transport equation.

The first method, the two-stream approximation, removes the variable μ by averaging over two angular intervals, seperating the intensity into upstreaming and downstreaming electrons. The remaining system of two coupled ordinary differential equation in s is solved numerically at all energies.

The second approach is based on the discrete ordinate method of Chandrasekhar (1960) which is usually applied to radiative transfer problems (e.g. Chandrasekhar, 1960 or Stamnes, 1986). Electron transport and radiative transfer are related problems, and Stamnes (1978) has shown that the discrete ordinate method can be applied to electron transport. With this approach, the phase functions are expanded into Legendre polynomials and the angular integrals in the transport equation are represented by sums. This leads to a system of coupled differential equations for the intensity. The solution is sought in the form of a finite series which leads to a system of linear algebraic equations. The corresponding matrix is numerically inverted and the intensities are then constructed from its coefficients.

3.1 The Energy Degradation

Common to both approaches is the treatment of the energy dependence. Examination of equation (2.6) shows that the determination of the energy dependent source term can

28

be separated from the transport aspect by excluding superelastic collisions, i.e. it is required that electrons do not gain energy in a collision. To evaluate the source term $Q_{\deg} = Q_{ex} + Q_{ion}$ at a given energy, knowledge of the intensity at higher energies is required and sufficient. Assuming that the energy grid of the numerical treatment extends to an energy E_N above which the intensity almost vanishes, the source $Q_{\deg}(s, E{=}E_N)$ due to degradation can be set to zero. The remaining homogeneous equation is then solved subject to boundary conditions in s. With knowledge of this solution the source term at the next lower energy level E_{N-1} can be evaluated. Proceeding in this way downward through the whole energy grid the complete solution is acquired.

The only other explicit energy dependence enters in the electron-electron loss term. On a discrete energy grid the differential is expressed as the difference of two terms

$$\frac{\partial}{\partial E} L(E) I(s, E) \longrightarrow \left(\frac{L_{n+1} I_{n+1}(s)}{\Delta E_n} - \frac{L_n I_n(s)}{\Delta E_n} \right)$$

with $I_n(s) = I(s, E_n)$ and $\Delta E_n = E_{n+1} - E_n$. Observing the sign of the two terms, the first one can be identified as a "source" which is dependent on the energy at the next higher level and can thus be included in the general source term Q. The second term is a "loss-term" at the current energy which can therefore be included in the general loss term $-n\sigma^{tot} I$. To simplify the notation we define $\Lambda(E_n) = \Lambda_n = L(E_n)/\Delta E_n$.

The geomagnetic field in the altitude range of interest and at high latitudes is almost homogeneous so that the second term in equation (2.6) vanishes. The path s along which the electrons are guided is a straight line through the atmosphere. If the angle between the horizontal and this path is α, the altitude z is given by $z = s \sin \alpha$. Substituting the scattering depth τ for the altitude z by

$$d\tau = - \sum_j \left(n_j(z) \sigma_j^{tot}(E) + n_e(z) \Lambda(E) \right) \, dz, \qquad (3.1)$$

where the sum j extends over all species, the transport equation (2.6) is simplified to read:

$$\frac{\mu}{\sin\alpha}\frac{\partial I(\tau,E,\mu)}{\partial\tau} = I(\tau,E,\mu) - \frac{\omega}{2}\int p(\mu\to\mu')I(\tau,E,\mu')\,d\mu' + Q(\tau,E,\mu;I). \qquad (3.2)$$

The elastic scattering albedo ω is defined by:

$$\omega = \frac{\sum_j n_j(z)\sigma_j^{el}(E)}{\sum_j n_j(z)\sigma_j^{tot}(E) + n_e(z)\Lambda(E)}. \qquad (3.3a)$$

The source term $Q_n = Q(\tau,E_n,\mu;I)$ at energy E_n is given by:

$$Q_n = Q_{\mathrm{Photo}}(\tau,E_n)\frac{dz}{d\tau} + \sum_{i=n+1}^{N} R_{in}I(\tau,E_i)\Delta E_i + n_e(\tau)\Lambda_{n+1}(\tau)I(\tau,E_{n+1})\frac{dz}{d\tau}. \qquad (3.3b)$$

The angular dependence has been omitted in this expression in order to highlight the energy degradation. The energy redistribution function

$$R_{in} = \frac{\sum_j n_j(z)\left(\sigma_j^{ex}(E_i+W) + \sigma_j^{deg}(E_i\to E_n) + \sigma_j^{sec}(E_i\to E_n)\right)}{\sum_j n_j(z)\sigma_j^{tot}(E_n) + n_e(z)\Lambda_n}$$

should, however, also include the angular redistribution of the degraded electrons, i.e. the phase functions p_{ex}, p_{deg}, and p_{sec}. If R_{in} is written in the form $R_{in} = \sum_\nu R_{in}^\nu$, where ν stands for 'ex', 'deg', and 'sec', the middle term of equation (3.3b) is expressed in more detail by

$$\sum_{i=n+1}^{N}\sum_\nu R_{in}^\nu \frac{1}{2}\int_{-1}^{1} p_\nu(E_i,\mu'\to\mu)I(\tau,E_i,\mu')\,d\mu'.$$

Under the assumption that the incident electron in an inelastic collision experiences only very small angular deflection, the phase functions p_{ex} and p_{deg} can be represented by δ-functions. After integrating over μ the expression for Q_n given above is recovered. The only correction stems from the term for the secondary electrons which are assumed to be produced with an isotropic distribution, independent of the incident electron. This means that the phase function is constant $p_{sec}(\mu) = 1$. Rather than multiplying $\sigma^{sec}(E_i)$ with just the intensity in equation (3.3b), the intensity has to be averaged over angle first.

The solution of the transport equation (3.2) consists of two major tasks. It requires solving the energy independent transport problem, i.e. the integro-differential equation in r and μ, and the energy degradation problem, i.e. the evaluation of the source function Q. The energy redistribution function $R(E' \to E)$ describes how the intensity cascades in energy due to excitation and ionization collisions. To accommodate the discrete and continuous losses of such interactions on a fixed energy grid, a careful discretization of R is necessary. The energy loss of an electron in a single collision is typically much smaller than the difference between adjacent energy cells of the energy grid. For the description of a large number of collisions by a large number of electrons, Swartz (1985) suggested a numerical scheme which describes the energy degradation on a discrete grid. This scheme is designed to conserve energy. An effective cross section is defined for the probability of degrading the intensity to an existing energy cell. For the energy degradation and the production of secondary electrons in ionizing collisions, two electrons have to be accommodated on the discrete grid and the normalization requirement (Eq. 2.5) has to be satisfied by the discretized energy redistribution function R. The definition of the effective cross section and the discretization of the energy redistribution function is shown in Appendix 1.

The transport problem that remains to be solved for each energy level, with Q given, is treated by two methods which will be described in the next two sections.

3.2 Two-Stream Approximation

The two-stream approximation has been applied by many authors (Nagy et al., 1969; Banks and Nagy, 1970; Nagy and Banks, 1970; Banks et al., 1974; Stamnes, 1981a) and may serve as an introduction to the understanding of electron transport within the atmosphere. It is well suited for this purpose because of its conceptual simplicity, and still leads to meaningful results for certain problems.

Instead of solving the angular dependent equation, an approximate solution is found for angle-averaged upward and downward intensities. In this binary treatment, where the intensity is either up or down, the phase functions reduce to single numbers, the backscatter ratios β. For inelastic collisions pure forward scattering is assumed so that in this case the backscatter ratio becomes zero, $\beta_{ex} = \beta_{deg} = 0$. The secondary electrons from ionizing collisions are assumed to be produced isotropically, i.e. $\beta_{sec} = 0.5$. The coupling between upward and downward intensities is primarily due to elastic scattering with a weak contribution from the production of secondaries.

The two equations for the up- and downward intensities are obtained by integrating the transport equation (3.2) over μ for the two intervals $-1 < \mu < 0$ and $0 < \mu < +1$. The upward intensity is defined by

$$I^+(\tau, E) = \int_0^1 I(\tau, E, \mu)\, d\mu,$$

the downward intensity is

$$I^-(\tau, E) = \int_{-1}^0 I(\tau, E, \mu)\, d\mu,$$

and the elastic backscatter ratio is given by

$$\beta(\mu) = \frac{1}{2} \int_0^1 p_{el}(\mu \to \mu')\, d\mu' \qquad \text{for } -1 < \mu < 0.$$

For the implementation of the two-stream approximation the μ-dependent backscatter ratio is integrated over a half sphere

$$\beta = \int_0^1 \beta(\mu)\, d\mu$$

to yield a constant backscatter ratio. From the normalization of the phase function it follows

$$\frac{1}{2} \int_0^1 p_{el}(\mu \to \mu')\, d\mu' = 1 - \beta \qquad \text{for } 0 < \mu < 1.$$

Carrying out the integration of the transport equation (3.2) over a half sphere ($0 < \mu < 1$) gives the following terms:

$$\int_0^1 \frac{\mu}{\sin\alpha} \frac{\partial I}{\partial \tau}\, d\mu = \frac{\bar{\mu}}{\sin\alpha} \frac{\partial I^+(\tau, E)}{\partial \tau}$$

with a mean value $\bar{\mu}$ such that

$$\bar{\mu} \int_0^1 I(\mu)\, d\mu = \int_0^1 \mu I(\mu)\, d\mu.$$

For the terms involving phase functions the integration over μ is done first, yielding the constant backscatter ratio, which is then pulled out of the integral over $d\mu'$:

$$\frac{\omega}{2} \int_{-1}^1 \int_0^1 p(\mu' \to \mu)\, d\mu\, I(\tau, E, \mu')\, d\mu'$$

$$= \frac{\omega}{2} \int_{-1}^0 \int_0^1 p(\mu' \to \mu)\, d\mu\, I(\tau, E, \mu')\, d\mu' + \frac{\omega}{2} \int_0^1 \int_0^1 p(\mu' \to \mu)\, d\mu\, I(\tau, E, \mu')\, d\mu'$$

$$= \omega\beta I^-(\tau, E) + \omega(1 - \beta) I^+(\tau, E).$$

These last two terms describe the intensity which is elastically backscattered from the "other" direction ($\omega\beta I^-$) and the intensity which is elastically forward scattered, maintaining its direction ($\omega(1 - \beta)I^+$). The analogous procedure for the downward direction ($-1 < \mu < 0$) leads to a system of two coupled equations:

$$\bar{\mu}\frac{\partial I^+}{\partial \tau} = I^+ - \omega(1 - \beta)I^+ - \omega\beta I^- - Q^+ \tag{3.4a}$$

$$-\bar{\mu}\frac{\partial I^-}{\partial \tau} = I^- - \omega(1 - \beta)I^- - \omega\beta I^+ - Q^-. \tag{3.4b}$$

The sources $Q^\pm$, which are a function of τ, E, and $I^\pm(\tau, E' > E)$, stand for the sum of all energy-degraded intensities and internal sources due to photoionization (Eq. 3.3b).

The derivation of the two-stream equations presented here differs from most conventional ways by the definition of I^+ and I^-. Rather than integrating over the angular dependent equation, one can define I^+ and I^- taken at some value $\bar{\mu}$ ($I^\pm = I(\pm\bar{\mu})$)

(Stamnes, 1978) and arrive at the same set of equations. Kusida and Kamiyama (1985) compare three approaches that differ by assumptions regarding the isotropy of the intensity and the phase function: Eddington, Gauss, and double-Gauss. The Eddington approach (Goody, 1964) assumes I to be hemispherically isotropic* which leads to $\bar{\mu} = 1/2$. No restrictions apply to the backscatter ratio β which is, as in this work, given by the integral over the phase function. Both the Gauss and double-Gauss approaches are based on the assumption that the intensity and the phase function can be approximated by polynomials, so that integrals over μ are exactly represented by sums. The Gauss approach gives exact results if the intensity $I(\mu)$ is a polynomial of order 2 and $p_{el}(\mu \rightarrow \mu')$ is a polynomial of order 1 over the entire range $-1 < \mu < 1$. In the double-Gauss case the interval is split into two hemispheres and the double-Gauss method produces exact results if $I(\mu)$ is a polynomial of order 1 for each hemisphere separately. Both Gauss and double-Gauss methods are special cases of a multi-stream treatment, while the Eddington approximation (Goody's definition) is a distinctive two-stream approach.

The differences that are introduced into the two-stream equations by these methods are reflected in the value of $\bar{\mu}$ and the backscatter ratio β. Instead of using an average value, $\bar{\mu}$ becomes the quadrature angle. The Gaussian case has $\bar{\mu} = 1/\sqrt{3}$, while the double-Gauss case gives $\bar{\mu} = 1/2$. Similarly, the phase function is represented by the moments of its Legendre polynomial expansion

$$g_l = \frac{1}{2} \int_{-1}^{1} p_{el}(\mu) P_l(\mu) \, d\mu$$

---

* Goody's definition of the 'Eddington approach' differs from other authors. Rather than assuming hemispherical isotropic intensity, the Eddington approach is defined as $I(\mu) = I_0 + \mu I_1$ (Shettle and Weinman, 1970; Joseph *et al.*, 1976). The only difference between this method and the double-Gaussian method lies in the definition of the boundary conditions, which are applied to the flux in the Eddington approach while the double-Gauss method applies boundary conditions to the intensity.

with P_l the Legendre polynomial of order l. The backscatter ratio then becomes, depending on the integration method:

$$\beta = \begin{cases} \frac{1}{2}(1 - g_1) & \text{Gauss} \\ \frac{1}{2}(1 - \frac{3}{4}g_1) & \text{double-Gauss.} \end{cases}$$

The general derivation of the two-stream equations given in this work includes all of these cases. Following Kusida and Kamiyama (1985), who conclude that the homogeneous transport equation is best approximated by the Gaussian method, and in agreement with Stamnes (1981a) I use $\bar{\mu} = 1/\sqrt{3}$ for the two-stream equations.

At every energy level equations (3.4a) and (3.4b) can be decoupled by taking the derivative with respect to τ of equation (3.4b) and inserting this into equation (3.4a) to eliminate $\partial I^+/\partial \tau$. This gives a second order differential equation for $I^-(\tau)$

$$\frac{\partial^2 I^-(\tau)}{\partial^2 \tau} + a_1(\tau)\frac{\partial I^-(\tau)}{\partial \tau} + a_2(\tau)I^-(\tau) = \gamma(\tau). \tag{3.5}$$

A detailed derivation of the coefficients a_1, a_2, and γ is given in Appendix 2.

At the highest energy of the grid the sources vanish and the equation can be solved in τ-space. Proceeding successively downward in energy, the source term can be evaluated and the equation again solved in τ. For a second order differential equation it is necessary to specify two boundary conditions. These are chosen to force the intensities to vanish at ground level, $I^-(\tau = \infty, E) = 0$ and to equal a given incident intensity at some altitude, which will be referred to as the top of the atmosphere, $I^-(\tau = 0, E) = I^\infty(E)$. For numerical applications $\tau = \infty$ and $\tau = 0$ must be approximated by realistic values.

The upward intensity can then be calculated from equation (3.4a). Stamnes (1981b), however, pointed out that better accuracy is achieved if an equation similar to equation (3.5) is derived for I^+ and solved in the same manner as for I^-, with only the upper boundary condition calculated from equation (3.4a). This decreases the large round-off errors that occur when derivatives are approximated by finite differences. Even with the

method suggested by Stamnes great care has to be taken when evaluating the boundary condition from I^- and equation (3.4a). Applying a fourth order finite differencing method to calculate the derivatives and using a double-precision (64 bits) code minimizes these round-off errors and comparable results are obtained with both methods.

For the solution of the differential equation an algorithm developed by John C. Adams at NCAR in Boulder, Colorado was used. This FORTRAN subroutine discretizes equation (3.5) in a second order finite difference approximation and solves the resulting tridiagonal system directly. A fourth order approximation is then obtained using deferred corrections.

This algorithm requires equal step sizes in r. Since the scattering depth changes only slightly at high altitudes and increases rapidly at low altitudes, an equal step size in r would accumulate almost all grid points at the lower boundary. If, for example, the boundaries are specified at 80 km and 520 km, and the r-grid is divided into 201 steps where r_1 refers to 520 km, the last 200 values of r refer to altitudes between 80 km and 114 km, and 117 grid points are between 80 km and 85 km. Although it is advantageous to increase the grid density at the lower boundary, this choice is much too widely spaced at the upper boundary. A mapping suggested by Stamnes (1981) distributes the grid points more evenly. It is defined by

$$x(r) = A + B \ln r,$$

where x is the transformed grid point, and A and B are constants that determine the mapping of the interval boundaries $r_{\min}$, $r_{\max}$ of the r-grid onto an interval in x. If the x-grid is chosen to cover the interval $[0, 1]$, these constants are:

$$A = -B \ln r_{\min} \qquad B = \frac{1}{\ln r_{\min} - \ln r_{\max}}.$$

This transformation cannot be applied to transform the semi-infinite interval $[0, \infty]$ to the finite interval $[0, 1]$. It serves, however, as a useful mapping of a practical range of scattering depths $[r_{\min}, r_{\max}]$.

For the two-stream calculation homogeneous boundary conditions are applied at 80 km with the upper boundary varying between 500 km and 800 km. The atmosphere in this range is represented by a mixture of N_2, O_2, and O as well as thermal electrons. Although comparable in density to the thermal electrons, positive ions are neglected, because the collision frequency for electron–positive ion collisions is much smaller than for electron–neutral collisions. The thermosphere does not contain a significant amount of negative ions. For the case of an upper boundary at 800 km atomic hydrogen and helium are also included. The neutral densities are taken from the MSIS-83 atmosphere (Hedin, 1983), which takes variations of the densities due to solar and geomagnetic activity, latitude, and local time into account. For high latitudes, however, the ratios of the neutral densities do not agree with observations (Rees *et al.*, 1977; Sharp *et al.*, 1979; Strickland *et al.*, 1983; Roble *et al.*, 1984; Sharp, 1985; Meier and Conway, 1985). To correct this discrepancy the MSIS-83 densities are multiplied by a constant. In most cases the MSIS-83 density of atomic oxygen is considered too high, and correction factors as small as 1/3 are applied.

Densities and temperatures of the ambient thermal electron gas, which are needed for the evaluation of the loss function $L(E)$ (Eq. 2.7), are selected from a set of altitude profiles acquired by rocket borne instruments and from theoretical works (Rees *et al.*, 1977).

The backscatter ratio is derived by adopting the screened Coulomb cross section. This is discussed in detail by Stamnes (1978) and references therein. Stamnes derives the formula for energies above 12 eV

$$\beta = \sqrt{\epsilon(1+\epsilon)} - \epsilon$$

with a screening parameter ϵ for the energy range below 500 eV given by

$$\epsilon = \frac{1}{2} \frac{1}{\left(\frac{E}{12}\right)^{3/4} - 1}, \tag{3.7a}$$

where E is the energy in eV. The Bethe approximation (e.g. Dawydow, 1974) can be applied above 500 eV and gives the screening parameter (Berger et al., 1970)

$$\epsilon = \frac{6.22 \cdot 10^{-5}}{(2 + E_r)E_r}. \tag{3.7b}$$

The variable E_r is the kinetic energy of the electron in units of the electron rest mass, $E_r = E/511000$ eV. For energies less than 12 eV isotropic scattering ($\beta = 0.5$) is assumed. This definition makes the backscatter ratio a continuous function of energy.

With the cross sections, densities, backscatter ratio, loss function, and a boundary condition specified, the transport equation (3.5) can be solved to yield the intensity as a function of altitude and energy. To ensure the correct performance of the numerical methods and to estimate the error of the results, tests can be conducted to check the self-consistency of the code. For very restricted cases an analytic solution to equation (3.4a,b) can be found and the numerical results can be checked against it. As shown by Stamnes (1981a), the solution to the transport equation with $Q = 0$, $\omega = $ const., and $\beta = $ const. is $I^{\pm}(\tau) = G^{\pm} \exp(-k\tau/\bar{\mu})$, where $k = \sqrt{(1 - \omega)(1 - \omega + 2\beta\omega)}$. The constant G^- is given by the boundary condition I^{∞} and

$$\frac{G^+}{G^-} = \frac{\sqrt{1 - \omega + 2\omega\beta} - \sqrt{1 - \omega}}{\sqrt{1 - \omega + 2\omega\beta} + \sqrt{1 - \omega}}.$$

As already mentioned, the computation of I^+ is dependent on the numerical evaluation of the derivative in equation (3.4b). A simple difference method introduces errors of 15% as compared to the analytic solution, while a fourth order approximation with double precision arithmetic (64 bits) enabled the code to reproduce the analytic solution to four significant digits. This error occurs independently at each energy level and introduces errors in the subsequent calculation of the sources. The error may then grow while penetrating the entire solution, and is considered to be the weakest link of the two-stream

approximation. Awareness of this deficiency suggests limiting the application of the two-stream approximation to electron transport that results from internal sources, such as photoelectrons. For this case, the source term Q is relatively less dependent on the previously calculated intensity at higher energy, which lessens the impact of the uncertainty inherent in the upper boundary condition.

From a comparison between two-stream and multi-stream approximations of the solution of equation (3.2), with the exclusion of the source term ($Q = 0$), Kusida and Kamiyama (1985) estimate that the errors that are introduced by the two-stream approximation amount to 20–30% at high energies. Their result suggests that for incident electron spectra with a high characteristic energy a multi-stream approach should be used. A test of the self-consistency of the computer code can be based on a comparison between the energy deposition in the atmosphere, and the net energy flux at the top of the atmosphere. This test shows an energy deficiency of 1% increasing to 20% for large characteristic energies. This error in the energy budget represents an overall numerical error. For incident electron spectra with a characteristic energy smaller than 1 keV this error is less than 10%. The application of this method of solution for the two-stream approximation is therefore limited to soft electron spectra.

3.3 Multi-Stream Approximation

The angular dependent transport equation is not merely a generalization of the methods used for two streams, as described in the previous paragraphs. Rather than reducing the general transport equation to a small number (e.g. 2) of coupled differential equations, the discrete ordinate method of Chandrasekhar (1960) is utilized.

The definitions of the scattering depth r and the single scattering albedo ω make these quantities formally equivalent to their radiative counterparts. Comparing the radiative

transfer equation (e.g. Stamnes and Swanson, 1981)

$$\mu \frac{\partial I(\tau, E)}{\partial \tau} = I(\tau, E) - \frac{\omega}{2} \int p(\mu, \mu') I(\tau, \mu') \, d\mu' - Q(\tau, \mu) \qquad (3.8)$$

which describes the transport of radiant energy through a scattering, absorbing and emitting medium to the electron transport equation (Eq. 3.2) shows their similarity. The radiative transfer equation has been given considerable attention in the literature and a reliable method of solution is available with the discrete ordinate method (Stamnes and Swanson, 1981; Stamnes and Conklin, 1984; Stamnes, 1985a; Tsay, 1986; Stamnes *et al.*, 1987). Only a brief description will be given here.

Rather than averaging over discrete angular ranges (as it was done in the two-stream approach), the intensity I is sampled at $2n$ Gaussian quadrature points in μ and the phase function P is expanded into Legendre Polynomials. The integral in equation (3.8) is replaced by a sum using the double-Gauss (Sykes, 1951) quadrature formula. The discrete ordinate method, as developed by Stamnes and co-workers, is restricted to a plane-parallel atmosphere. This atmosphere is represented by M layers with specified scattering depths, scattering albedos, and phase functions. A solution of the homogeneous equation is constructed for each layer $m = 1, \ldots, M$ as a series

$$I_H^m(\tau, \mu_i) = \sum_{j=-n}^{n} L_j^m g_j^m(\mu_i) e^{-k_j^m \tau} \qquad \text{for} \qquad i = 1, \ldots, 2n,$$

where the $g_j^m(\mu_i)$'s are the eigenvectors of the system of $2n$ coupled differential equations representing the discretized version of equation (3.8), the eigenvalues are k_j^m, and the L_j^m's are integration constants determined by the boundary conditions. The source Q, which is calculated from the energy degradation, is approximated by a linear function within each layer and a particular solution of the form

$$I_P^m(\tau, \mu_i) = z_0^m(\mu_i) + z_1^m(\mu_i)\tau$$

is sought. The general solution is then constructed as the sum of the homogeneous and the particular solution. This method reduces the integro-differential equation (3.8) to M systems of $2n$ algebraic equations which have to be inverted simultaneously for all layers. The requirement of continuity of the intensity across layer interfaces and boundary conditions for the uppermost and lowest layers determine the constants of integration L_j^m. For the electron transport problem the boundary conditions are given by the intensity at the top of the atmosphere in all downward directions and zero intensity in all upward directions at the lowest altitude.

The Legendre expansion of the azimuthally averaged phase function $p(\cos \Theta)$, with Θ the scattering angle between μ and μ', gives

$$p(\cos \Theta) = p(\mu \rightarrow \mu') = \sum_{l=0}^{2n-1} (2l + 1) \chi_l P_l(\mu) P_l(\mu'), \qquad (3.9)$$

with $P_l(\mu)$ the Legendre polynomial of order l. The moments χ_l are determined by the orthogonality of the Legendre polynomials and are given by

$$\chi_l = \frac{1}{2} \int_{-1}^{1} P_l(\cos \Theta) p(\cos \Theta) \, d(\cos \Theta). \qquad (3.10)$$

A suitable phase function for electron scattering is given by the Rutherford formula with a screening parameter ϵ (see Eq. 3.7):

$$p(\cos \Theta) = \frac{4\epsilon(1 + \epsilon)}{(1 + 2\epsilon - \cos \Theta)^2}. \qquad (3.11)$$

The screening parameter becomes very small for large energies causing a strong forward peak in the phase function. This creates two problems. The representation of the phase function by a truncated Legendre series becomes inaccurate and a numerical evaluation of the integral in equation (3.10) becomes very time consuming. The use of a recursion

relation for the calculation of the moments overcomes the latter difficulty. Stamnes (1980) gives the first two moments by analytically solving the integral:

$$\chi_0 = 1 \qquad \chi_1 = 1 + 2\epsilon\left(1 - (1+\epsilon)\ln(1+\frac{1}{\epsilon})\right)$$

and R. Link (1986, private communication) provided the recursion formula

$$\chi_l = \frac{1}{l-1}\left((2l-1)(1+2\epsilon)\chi_{l-1} - l\chi_{l-2}\right).$$

Although this formula remains to be proven for an arbitrary order l, a numerical compari-son with the moments directly calculated from equation (3.10), using a Lobatto integration formula (Abramowitz and Stegun, 1972), showed its validity to, at least, order 16.

A strongly peaked phase function necessitates using a large number of terms in equa-tion (3.9). The series may not be truncated before the moments χ_l have decreased to values which are much less than unity, in order to be a meaningful representation of the phase function. Wiscombe (1977) describes a method, which he calls δ-M, where the peak of the phase function is removed and treated separately. Instead of the expansion (3.9) the phase function is approximated by

$$p(\mu \rightarrow \mu') = 2\chi_{2n}\delta(\mu - \mu') + (1 - \chi_{2n})\sum_{l=0}^{2n-1}(2l+1)\chi_l^* P_l(\mu)P_l(\mu').$$

Wiscombe shows that the homogeneous radiative transfer equation is formally left un-changed by this redefinition of the phase function expansion, if the scattering albedo ω and the optical depth τ are replaced by

$$\omega^* = \omega\frac{1 - \chi_{2n}}{1 - \omega\chi_{2n}} \qquad d\tau^* = (1 - \omega\chi_{2n})\,d\tau.$$

The moments χ_l^* of this expansion are related to the moments χ_l in Eq. (3.9) by

$$\chi_l^* = \frac{\chi_l - \chi_{2n}}{1 - \chi_{2n}}.$$

These transformations are substituted into the electron transport equation together with

$$Q^* = \frac{1}{1 - \omega \chi_{2n}} Q.$$

Tsay (1986) shows that the inhomogeneous transport equation is then formally identical to equation (3.8).

The Rutherford formula Eq. (3.11) is based on the Born approximation (e.g. Dawydow, 1974) and can therefore only be applied at high energy. The screening parameter ϵ, however, allows modification of the phase function and extention of the applicability of Eq. (3.11) to lower energy. Using the formula (Eq. 3.7) of Stamnes (1978) and Wedde (1976) for low energy, the experimentally observed backscatter ratio is reproduced. The fine structure in the phase function at energies below 100 eV, as found by Shyn et al. (1972), is lost in this representation. To include this structure, the moments of the phase function have to be numerically evaluated by integrating equation (3.10). This requires elaborate numerical schemes in order to achieve adequate accuracy. This work adopts a compromise of the Rutherford formula with a modified screening parameter (see Eq. 3.7a and b). Exploring the influence of a more structured phase function will be left for the future.

3.4 The Electron Intensity

The general transport equation yields the intensity as a function of altitude, energy, pitch angle, and time. The steady state intensity contains all the information that is necessary to describe the auroral electrons. The relationship between the intensity I and the distribution function f was explained in Chapter 2, I being the differential analogue to the first velocity moment of f (Eq. 2.2). By analogy, the energy moments of the intensity

are related to the next higher velocity moments of the distribution function. The zeroth energy moment of the intensity therefore gives the number flux

$$F_N(z) = 2\pi \int_0^\infty dE \int_{-1}^1 I(z, E, \mu)\mu \, d\mu.$$

If the μ integration is extended over the upper hemisphere only, the zeroth energy moment of the intensity defines the upward number flux, $F_N^+(z)$, and similarly for the downward number flux, $F_N^-(z)$. Likewise the upward and downward energy fluxes are given by the first energy moment of the intensity

$$F_E^+(z) = 2\pi \int_0^\infty E \, dE \int_0^1 I(z, E, \mu)\mu \, d\mu$$

$$F_E^-(z) = 2\pi \int_0^\infty E \, dE \int_{-1}^0 I(z, E, \mu)\mu \, d\mu.$$

In order to describe the intensity completely, its moments must be known to infinite order. The first two moments, however, are already adequate to specify the intensity of the precipitating electrons at the top of the atmosphere by the characteristic energy

$$E_{\text{char}} = \frac{1}{2}\frac{F_E^-(z_{\text{max}})}{F_N^-(z_{\text{max}})}$$

and the energy flux $F_E^-(z_{\text{max}})$ itself. This definition makes the characteristic energy half of the mean energy. Although this characterization does not contain any information on the shape of the electron spectrum, it is sufficient for some applications.

Two basic types of synthetic electron spectra as well as actually observed spectra are adopted as a boundary condition. A Maxwellian spectrum is defined by

$$I^\infty(E) = \frac{Q_0}{4\pi E_c^3 \bar{\mu}} E e^{-E/E_c}.$$

Using the integral formula (Gradshteyn and Ryzhik, 1965, *3.351.3.*)

$$\int_0^\infty E^n e^{-E/E_c} \, dE = n! \, E_c^{n+1}$$

the number flux ($n = 1$) becomes $F_N^-(z_{\max}) = Q_0/2E_c$ and the energy flux ($n = 2$) is $F_E^-(z_{\max}) = Q_0$ which results in the characteristic energy $E_{\text{char}} = E_c$. In order to approximate observed auroral electron spectra, a power law energy spectrum is added at low energies.

A monoenergetic spectrum is modelled by a Gaussian distribution with a peak energy E_c and a halfwidth E_a:

$$I^\infty(E) = \frac{Q_0}{2\pi^{3/2}\bar{\mu}E_aE_c} \exp\left[-\left(\frac{E_c - E}{E_a}\right)^2\right].$$

With the restriction $E_a \ll E_c$ the integral $\int_0^\infty I^\infty\, dE$ can be approximated by $\int_{-\infty}^\infty I^\infty\, dE$ and a standard integration formula for Gauss distributions can be used (e.g. Rottmann, 1960). The energy flux is then given by $F_E^-(z_{\max}) = Q_0$ and the characteristic energy becomes $E_{\text{char}} = \frac{1}{2}E_c$.

In order to discuss the general behavior of the intensity as an electron beam penetrates into the atmosphere, a Maxwellian spectrum, plus power law energy spectrum at low energies, with $Q_0 = 1$ erg cm^{-2}sec^{-1} and a characteristic energy of 6 keV is applied as a boundary condition in the following example. The calculation is done for 8 streams, and the boundary condition is chosen to give an isotropic intensity over the downward hemisphere. Rather than plotting the intensity, Fig. 3.1 shows the downward flux $F^-(z, E) = 2\pi \int_{-1}^0 \mu\, d\mu\, I(z, E, \mu)$ as a function of energy for several altitudes. It can be seen that the energy at which the flux has a maximum, increases with penetration into the atmosphere. This is a consequence of the energy dependence of the ionization cross sections which have a maximum at approximately 100 eV. As a result, the scattering length at high energy becomes large, allowing the energetic electrons to penetrate deeper than those at low energy. The production of secondary electrons and degradation in energy, however, supply low energy electrons at all altitudes. This shows up in the steep increase of the intensity with decreasing energy. A comparison of the low energy part of the spectrum
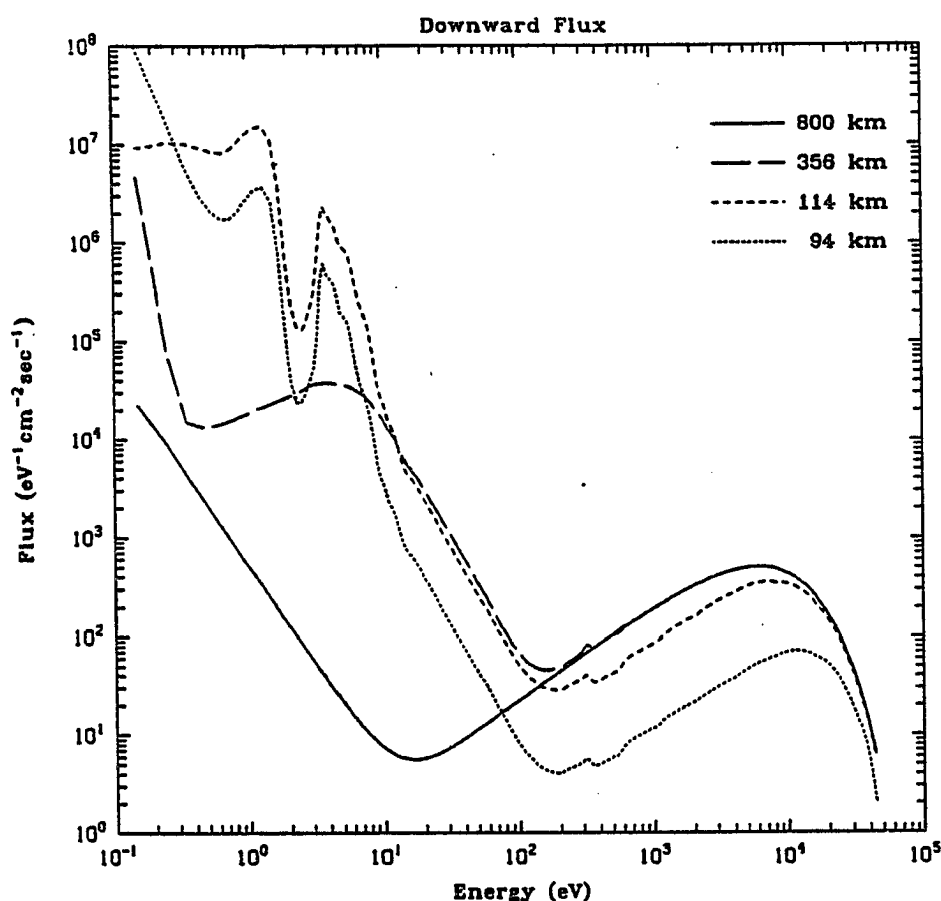
Fig. 3.1 The downward flux for 4 different altitudes from an isotropic Maxwellian input spectrum with $E_{char} = 6$ keV. The 800 km graph constitutes the boundary condition. At low energy (below ≈ 10 eV) a powerlaw with E^{-2} was added to the Maxwellian distribution. The calculation was carried out in a 8-stream mode.

to a run with a Maxwellian boundary condition without the added powerlaw, shows that this increase is independent of the applied boundary condition. The vibrational excitation of N_2, which has a large cross section confined to a narrow energy interval, causes a local intensity minimum at about 2.5 eV. Below ≈ 1 eV the dominant loss process is heating of the ambient electron gas, as described by the loss function (Eq. 3.6).

Although the O fine structure excitation has a large cross section in this energy range, it is not a very efficient energy degradation process due to the small energy loss. With decreasing energy, the intensity shows a steep increase at the local thermal energy. This is
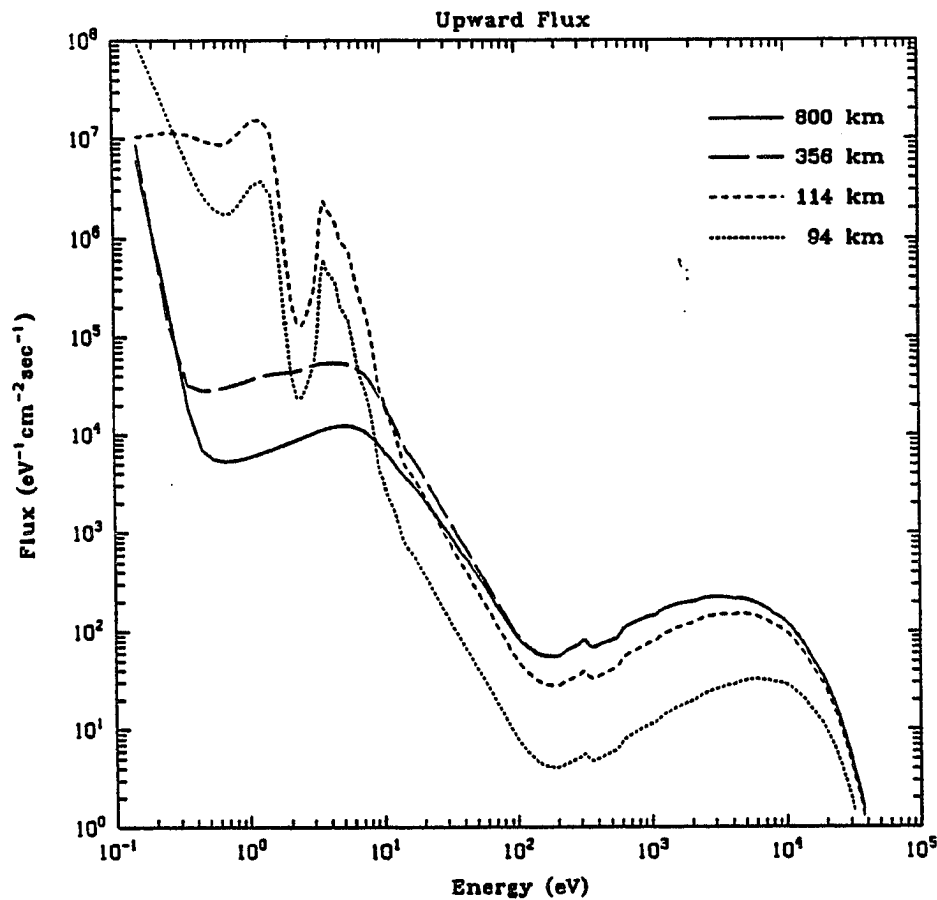
Fig. 3.2 The upward directed flux corresponding to the downward flux in Fig. 3.1.

best seen at high altitudes (356 km in Fig. 3.1). The transport calculation is inadequate for describing thermal electrons and must be combined with an energy equation in this low energy range (Schunk *et al.*, 1986). The computations in this work are therefore not extended below the thermal energy.

The upward directed flux is shown in Fig. 3.2 at the same altitudes as those that were selected in Fig. 3.1. The general appearance of the flux is similar to the downward flux, except that the maximum around 6 keV is not as pronounced. For a better comparison, the up- and downward fluxes are plotted together in Fig 3.3. The upward flux which escapes

the atmosphere at the upper boundary is used to define an albedo for the particle flux as well as for the energy flux

$$E_{alb} = \frac{F_E^-(z=\infty)}{F_E^+(z=\infty)}$$

$$P_{alb} = \frac{F_N^-(z=\infty)}{F_N^+(z=\infty)}.$$

In contrast to the energy albedo, the particle albedo is sensitive to the intensity at low energies. The downward intensity at the top of the atmosphere is given as a boundary condition, which can be varied at low energies without significant influence on the upward intensity. Thus the absolute value of the particle albedo contains some ambiguity. Using a consistent type of spectrum for the boundary condition allows a relative comparison between spectra with different characteristic energies. Fig. 3.4 shows the albedos as a function of the characteristic energy of the incident spectrum. The simultaneous constancy of the energy albedo and decrease of the particle albedo with E_{char} indicates that the mean energy per escaping electron increases with E_{char}. This is more clearly expressed by the increase of the ratio of the characteristic energies of the upward flux to the downward flux (Fig. 3.5).

To further illustrate penetration, and internal sources due to degradation in different energy regions, Fig. 3.6 shows altitude profiles of the upward and downward fluxes. At high energy (2 keV) the downward flux penetrates deeply into the atmosphere without a significant altitude variation above 200 km. The upward flux is almost entirely due to elastic scattering, and it follows the downward flux with a fixed ratio. At a smaller energy (100 eV) internal sources from degradation and secondary electron production become important and add to the direct component, causing the downward flux to increase where the density of the scatterers becomes large. At even smaller energy (5 eV) the upward and downward fluxes are dominated by the degradation source, and almost parallel the altitude profile of the density, until the sources from higher energies become unavailable (100 km).
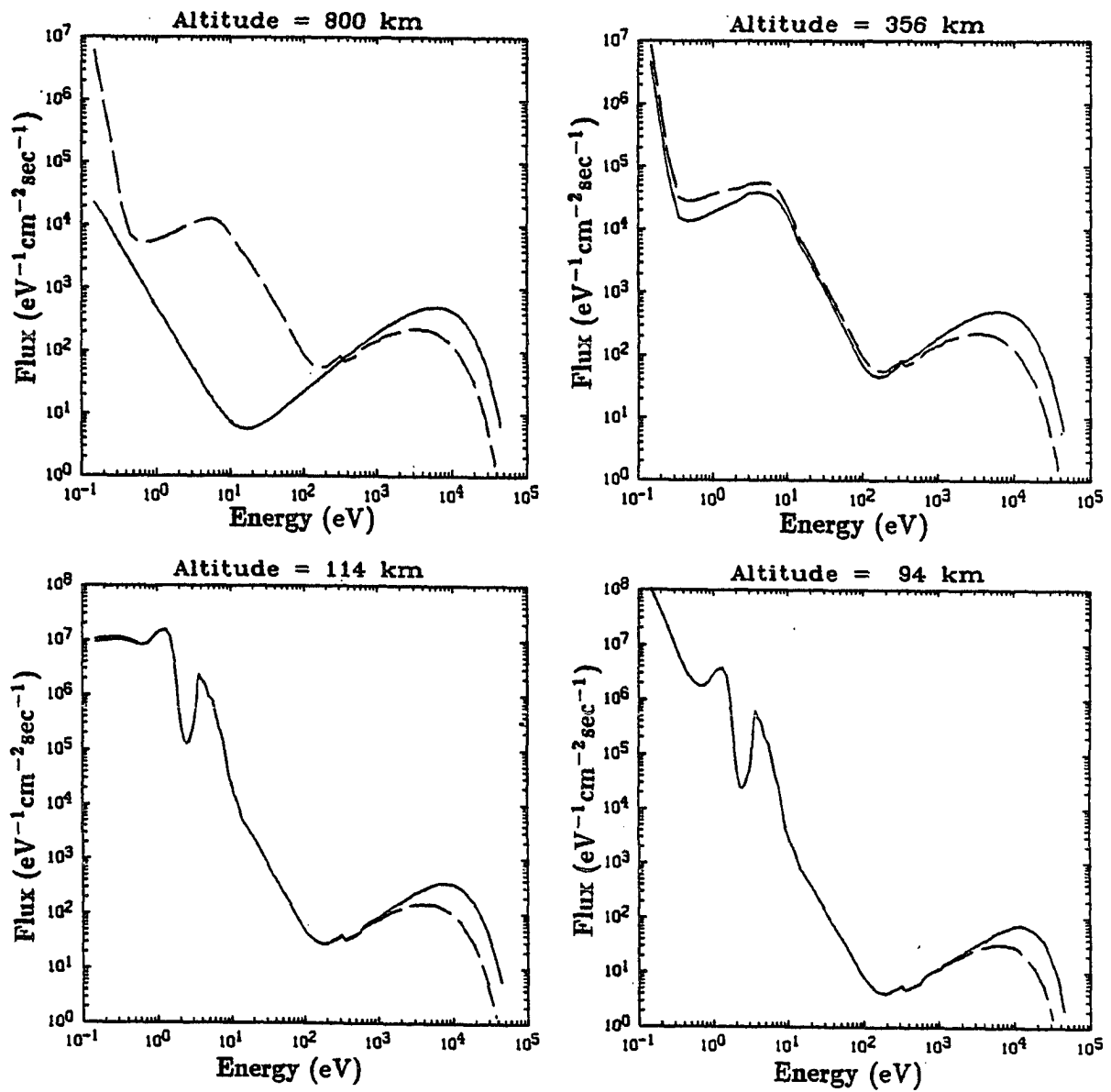
Fig. 3.3 The downward (solid line) and upward (broken line) fluxes at the same altitudes as in Fig. 3.1 and 3.2 plotted together for comparison.
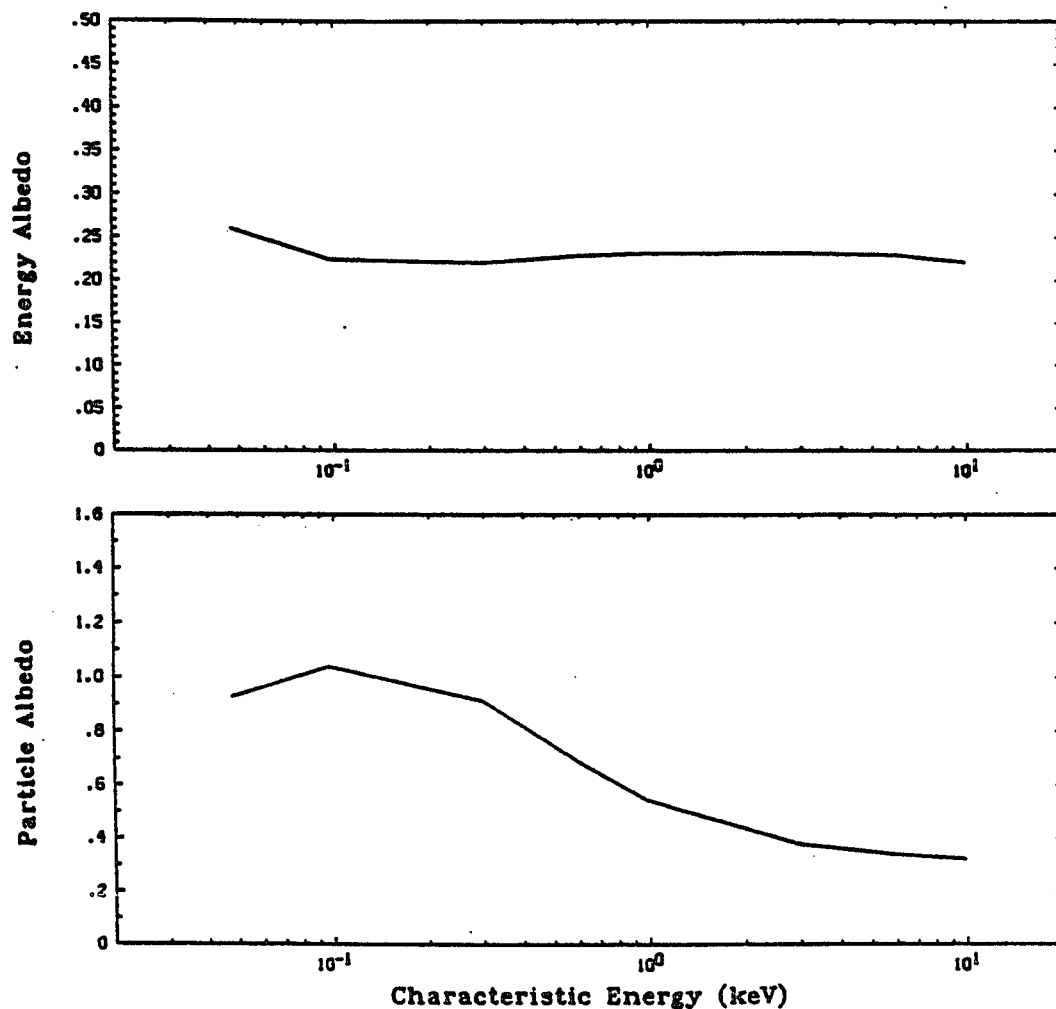
Fig. 3.4 Energy and particle albedo as a function of E_{char} for Maxwellian type input intensities.

At low energy the upward flux has its main source region at the altitude of the maximum downward flux, from which it seems to escape upwards. Although individual electrons do not necessarily follow the scheme described here, but rather undergo multiple scattering and degradation events in a random manner, the ensemble reaction can be understood and described in this simplified fashion.

If instead of a downward isotropic boundary condition, a monodirectional incident beam is applied, the penetration depth increases for the high energy component, but
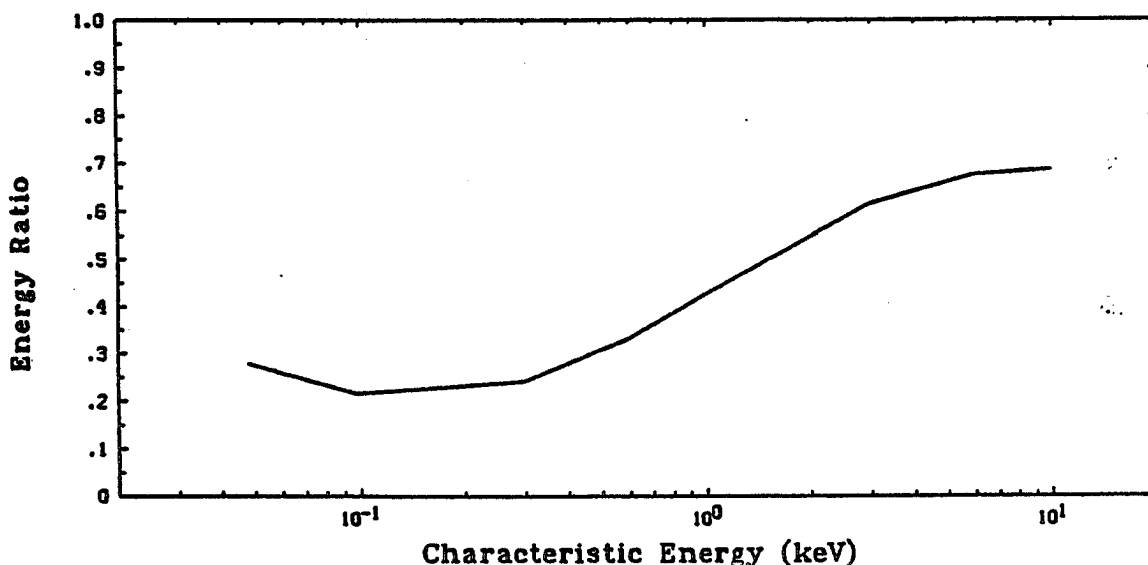
Fig. 3.5 Ratio of the characteristic energy of the upward to downward spectrum as a function of E_{char} of the incident intensity.

the general behavior is the same as for the isotropic case. The intensity at low energy quickly becomes isotropic from elastic scattering and production of secondaries, and keeps its directional characteristics only at high energy, where forward scattering prevails. The following chapter analyses the angular distribution of the intensity more closely.

Knowing the intensity, the energy deposition $\varepsilon(z)$ into a given state of a neutral or ion as a function of altitude can be derived. The energy loss in a single excitation collision with cross section $\sigma(E)$ is equivalent to the threshold T. The energy deposition rate is defined by

$$\varepsilon(z) = 2\pi n(z) \int_0^\infty dE \int_{-1}^1 I(z, E, \mu) T \sigma(E) \, d\mu. \tag{3.11}$$

In an ionizing collision some of the energy loss of the incident (primary) electron is carried away by the secondary. The total energy loss is therefore the sum of the thresholds for ionization and excitation of the ion and the energy of the secondary. This energy loss must be distinguished from what is generally referred to as the average energy loss per ion pair. Laboratory experiments as well as theoretical calculations show that the average
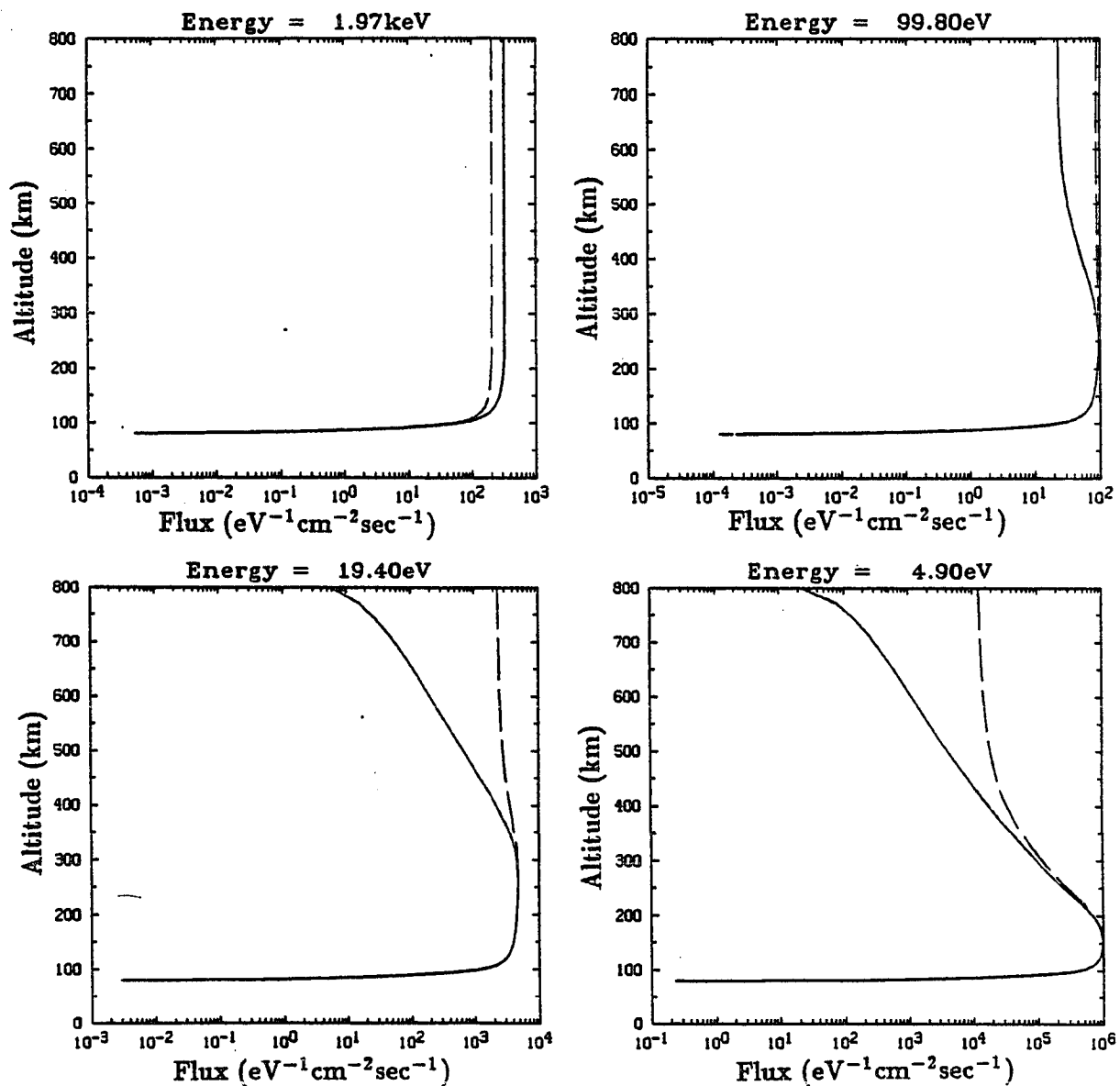
Fig. 3.6 Downward (solid lines) and upward (broken lines) fluxes as a function of altitude for 4 selected energies.
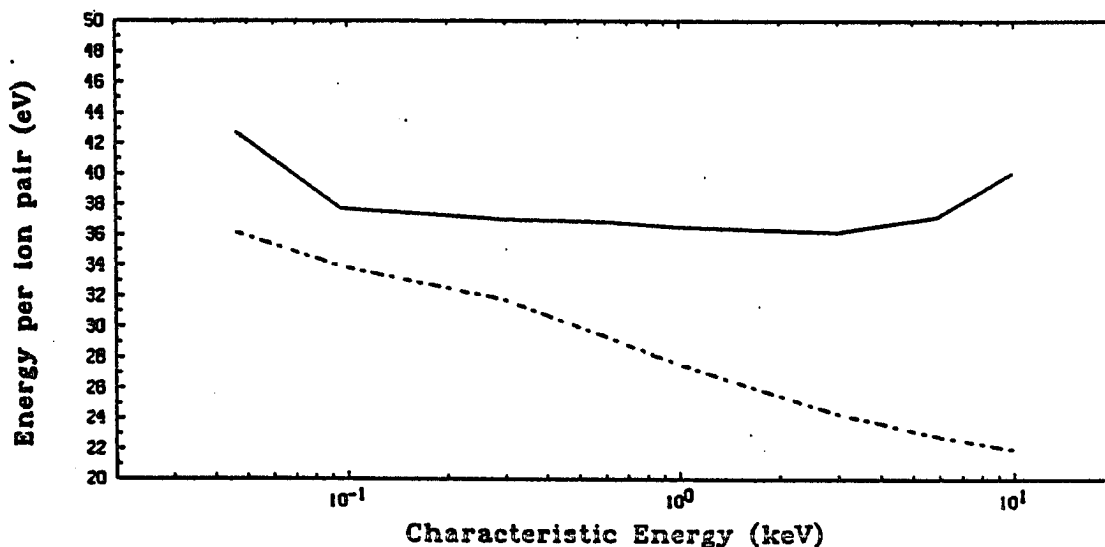
Fig. 3.7 Mean energy loss per ion pair (solid line) as a function of E_{char}. Also shown is the mean energy deposition per ion pair (dashed line).

energy loss per ion pair, W_e, is almost independent of the energy of the incident primary electron above 70 eV (Dalgarno and Griffing, 1958). Valentine and Curran (1958) review the experiments to that date which establish a value of $W_e = 35$ eV for N_2 as well as for air. The experimental data are based on the assumption that the ionizing electrons and all degraded and secondary electrons are completely absorbed in the gas. In the atmosphere, this is not the case. A fraction between 20% to 30% (see Fig. 3.4) of the incident energy flux escapes at the top of the atmosphere due to elastic scattering. The average deposited energy per ion pair is therefore dependent on the density distribution, the elastic scattering cross section and the phase function, and cannot be compared to the laboratory results. Instead, the energy flux that leaves the atmosphere has to be included in the total energy loss.

The energy loss per ion pair is plotted in Fig. 3.7 against E_{char} of the incident spectrum, based on the energy deposition as well as taking the escaping energy flux into account. As already pointed out, the mean energy of the escape flux increases with E_{char}, which in turn means that less energy is deposited. This is reflected in the decrease with

E_{char} of the energy deposited per ion pair formed. Including the escape flux in the energy loss yields a value of $W_e \simeq 38$ eV almost independent of E_{char}, but higher than the laboratory results. Based on the energy conservation test, the accuracy of the computer code is estimated to be $\sim 10\%$ so that the significance of the larger value is doubtful and not amenable to interpretation. It may be speculated that the set of cross sections has a systematic error which favors the ionization cross sections over the excitation.

The sum of $\epsilon(z)$ over all states of all species gives the energy deposition at altitude z, and integration over z gives the total energy deposition. As was pointed out earlier, a comparison of the net energy flux into the atmosphere to the energy deposition provides a useful check for the accuracy of the computer code. In this respect, the multi-stream code is much more accurate, even if run in a two-stream mode, than the two-stream approximation that is discussed in section 3.2. The error in the energy budget stays below 10% even for large energy grids. As indicated in section 3.1, the two-stream approximation requires evaluation of a derivative for calculating the upward intensity, while the discrete ordinate method solves for all angular bins simultaneously. This proves to be an advantage, especially for large energy grids, and significantly reduces the error in the energy budget. It must be stressed that this error estimate is useful only for a self-consistency test of the computer code, and does not provide an evaluation of the accuracy of the densities, cross sections, phase functions, or other inputs.

3.5 Comparison of the Intensity Calculations with Measurements in an Auroral Arc

On 9 March, 1978 a sounding rocket was launched from the Poker Flat rocket range (Fairbanks, Alaska) into a stable pre-midnight auroral arc on a trajectory that lay approximately in the magnetic meridian. A description of the payload and the acquired data is presented

by Pulliam *et al.* (1981). The aurora was characterized as an electron arc with a brightness of about 40 kR in OI 5577Å and an adjacent region of diffuse aurora to the south. Shortly after the experiment a breakup occurred, but during the rocket flight the aurora was described as stationary and static. Among other instruments there were two electron spectrometers with 11 energy channels which covered the range from 30 eV to 21 keV. They were mounted on the spinning payload such that they scanned the entire pitch angle range every 0.6 sec. Four-second averages of the electron intensities were binned into 36 equal angular bins with 5° width each. These data were provided by H. R. Anderson. Fig. 3.8 shows the downward energy flux as a function of range. The main optical emission features are coincident with the region of maximum downward energy flux and lies between 100 km and 150 km range. This region was traversed approximately at apogee at 340 km altitude.

The study by Pulliam *et al.* (1981) focused on hemispherical averages of the electron intensity, which were compared to a two stream transport calculation and discussed in terms of an acceleration mechanism (Evans, 1974). Using the measured downward intensity as a boundary condition, Pulliam *et al.* found their computed upward intensity in reasonable agreement with the measured data. Since their analysis was confined to a two-stream transport calculation, they could not analyse the angular distribution of the electron spectrum. The multi-stream transport code is used here to extend the analysis.

Describing the downward intensity data, Pulliam *et al.* noted a soft ($\leq$ 1 keV) and mostly isotropic electron spectrum south of the main precipitation region. As the rocket penetrated into the region of maximum energy flux, they observed an enhanced field aligned component of the intensity that gradually shifted to higher energies (from 1 to 6 keV). Occasionally, bursts of low energy field aligned electrons were superimposed on the spectra throughout the flight. These bursts are seen in successive sampling periods, indicating a duration of 4 to 16 flight seconds, or a horizontal extent of 2 to 8 km. Examples of the
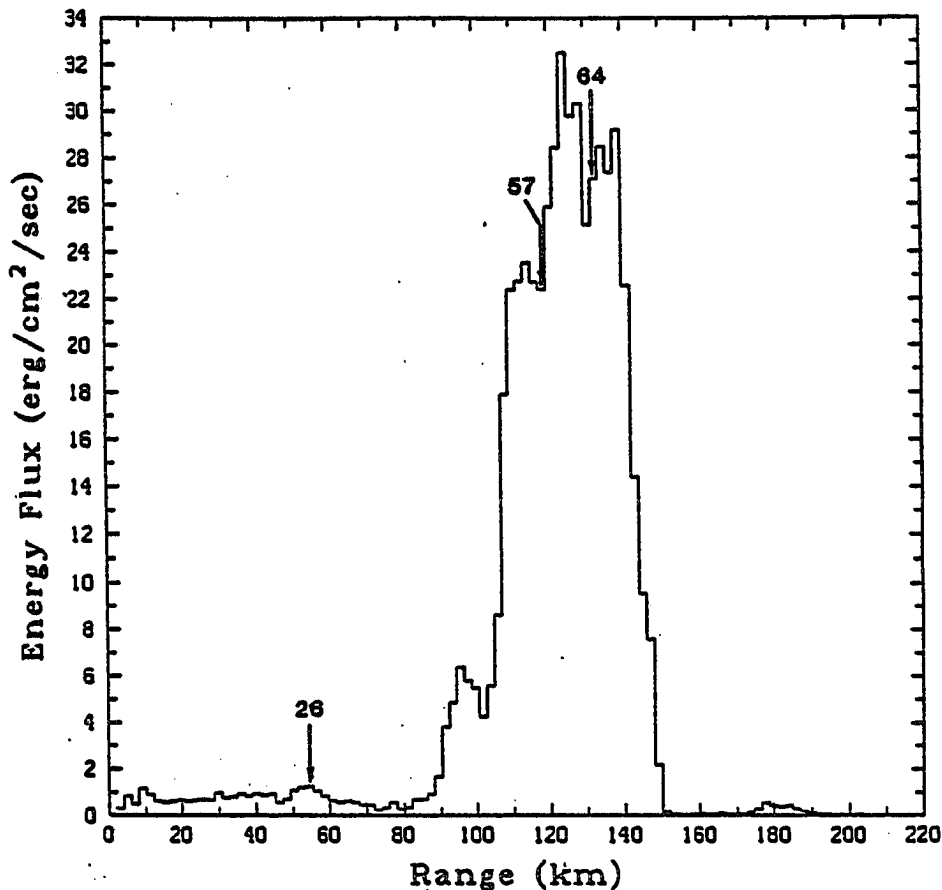
Fig. 3.8 Downward energy flux vs. range. Magnetic south is on the left. The flight followed roughly a magnetic meridian. The arrows indicate the positions where the data sets 26, 57, and 64 were taken.

intensity spectrum and the angular distribution are shown in Fig. 3.9a–c. These examples are taken at the locations indicated by arrows in the energy flux plot (Fig. 3.8). The first example, data set 26, shows a low energy field aligned burst without much intensity at higher energies (Fig. 3.9a). The altitude of the payload was 270 km and the total downward energy flux was 1.2 erg/cm^2/sec. Data set 57 was taken at apogee (340 km) and shows a low energy field aligned burst combined with high energy particles (Fig. 3.9b). The sensors at 2.6 and 6 keV show a very narrow field aligned downward intensity which persisted within the region of the maximum energy flux. The low energy bursts in that region were

interspersed with near isotropic distributions as the one in data set 64 (Fig. 3.9c). This set exhibits a high energy event with near isotropic low energy electrons taken 28 sec after data set 57. Both data sets 57 and 64 were acquired at locations near the maximum energy flux, 22.4 and 27.1 $erg/cm^2/sec$ respectively.

These examples are "typical" in the sense that they represent different types of anisotropy of the electron spectrum which can be found throughout this flight. Assuming that the aurora was stationary during the traverse of the rocket, it can be seen that the main region of electron precipitation was highly structured. Five isolated low energy bursts were located within the range 110 to 150 km. The energy flux (Fig. 3.8), which reflects mostly the high energy component, also shows significant variation across this region. The intensity data are averaged over 4 flight seconds, which corresponds to a horizontal resolution of 2 km. Optical auroral observations show a much finer structure, with the width of individual auroral arcs being of the same size or smaller than current camera resolution allows to determine (e.g. Lanchester and Rees, 1987). The width of an arc is estimated to be less than 200 m. The intensity data shown here therefore represent averages over several arcs.

In order to analyse the upward intensity, the measured downward intensities of the three data sets were used as a boundary condition for the multi-stream transport equation. To achieve a comparable angular resolution, the calculations were carried out with 32 streams. The MSIS densities were calculated for the date and time of the launch and the O density was scaled by a factor of 1/2.

Fig. 3.10 displays a comparison of the angle averaged upward flux between the computations and the measurements for the three sets. The horizontal bars show the measured flux while the solid line is the result of the transport calculation. The length of the bars indicates the energy range of the detectors. The agreement between measurement and computation is comparable to the results that are found by the two-stream calculations of
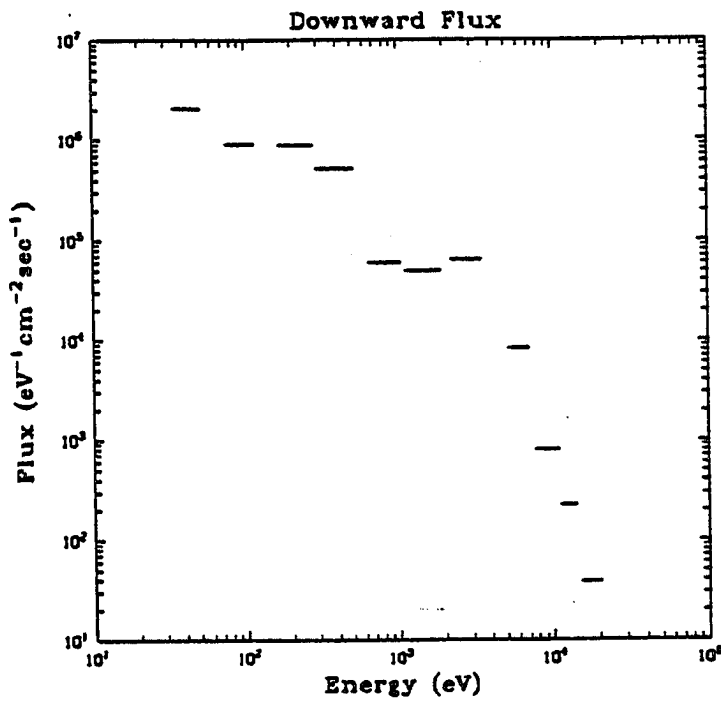
Downward Flux

Fig 3.9a Energy dependence of the downward flux (left) and angular distribution of the intensity (bottom) of data set 26. The length of the bars in the energy plot shows the range of the individual sensors. The angular distribution plots are normalized individually for each energy bin with the normalization factor shown on the ordinate with units eV cm^{-2} sec^{-1}. Each plot is identified by the center energy (in eV) of the corresponding energy bin. The abscissae are oriented normal to the magnetic field. Each data point represents a 4 sec average in a 5° pitch angle bin. The radii at which the points are located, give a linear measure of the intensity.
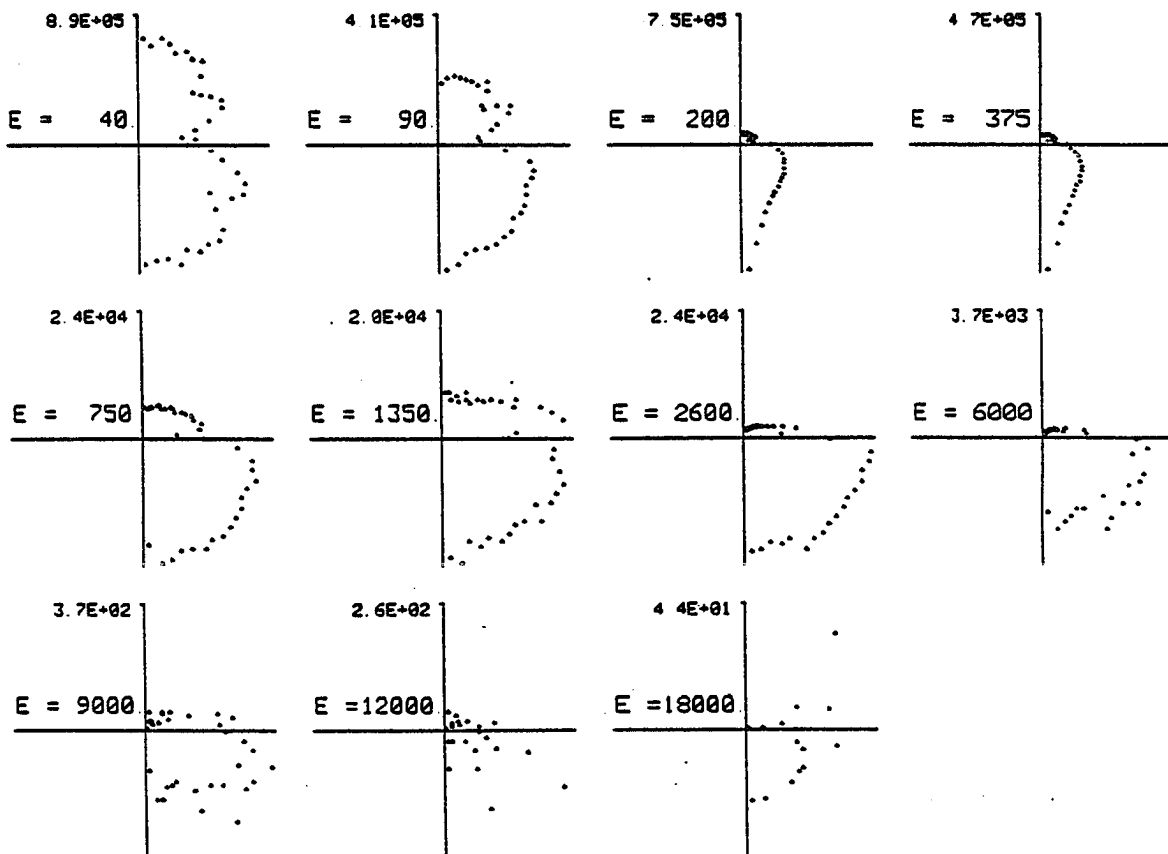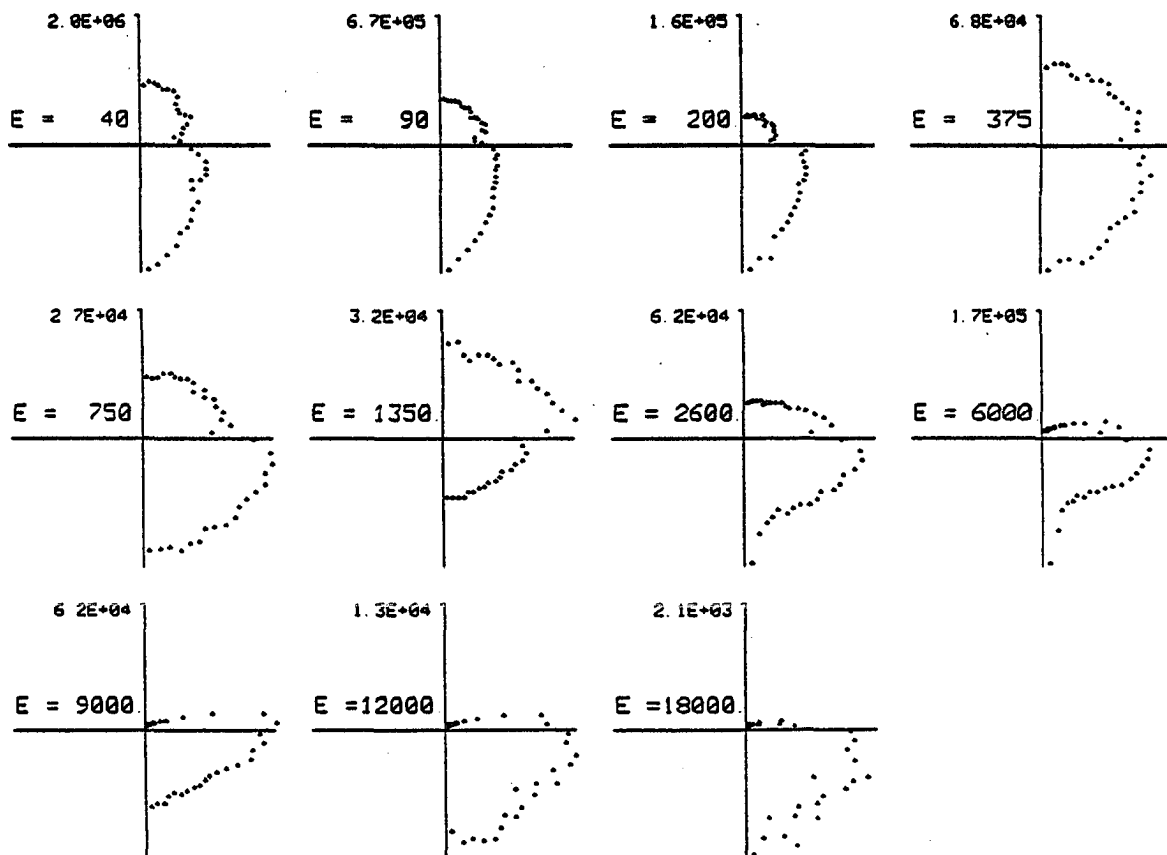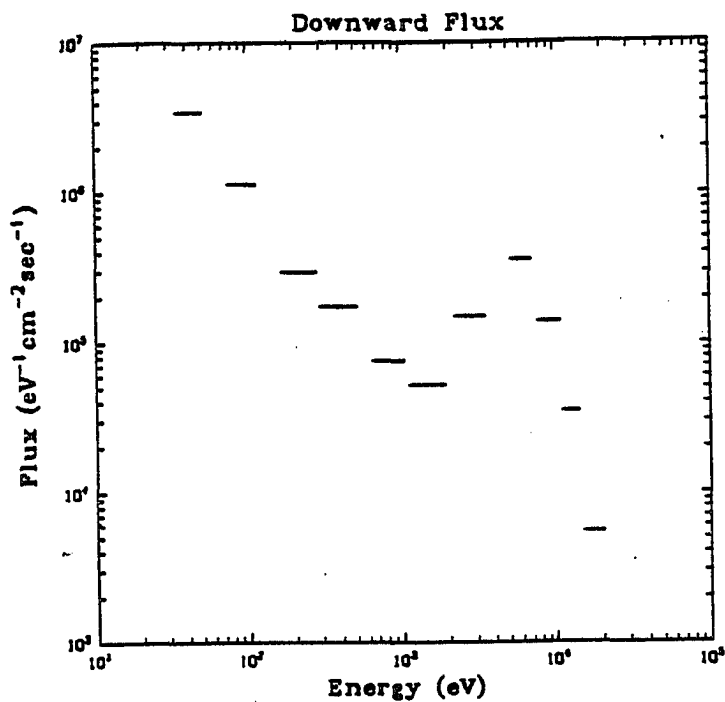
Fig. 3.9b   Same as Fig. 3.9a for data set 57.

Downward Flux

Flux (eV^{-1} cm^{-2} sec^{-1})

Energy (eV)

1. 2E+06   E = 40.

4. 4E+05   E = 90.

1. 1E+05   E = 200.

6. 6E+04   E = 375.

2. 9E+04   E = 750.

3. 4E+04   E = 1350.

6. 4E+04   E = 2600.

1. 3E+05   E = 6000.

8. 9E+04   E = 9000.

2. 1E+04   E =12000.

3. 2E+03   E =18000.
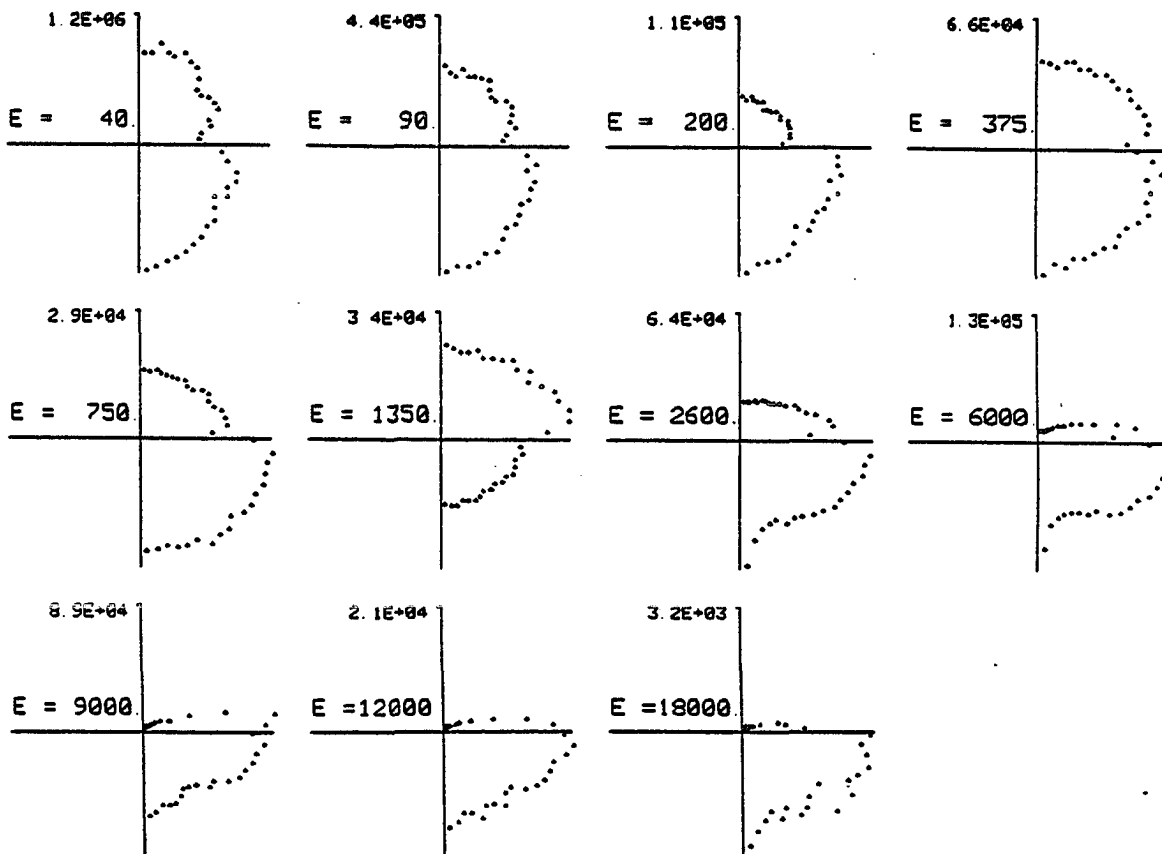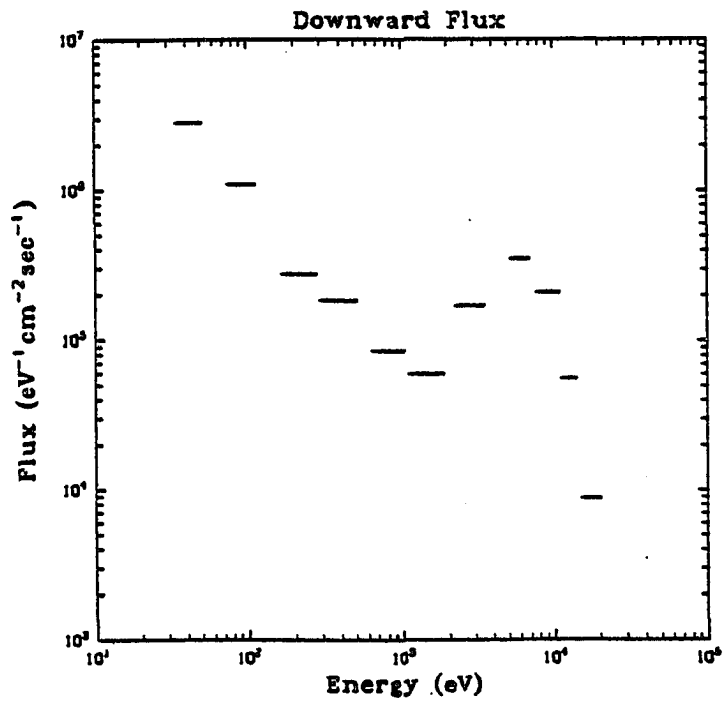
Fig. 3.9c   Same as Fig. 3.9a for data set 64.
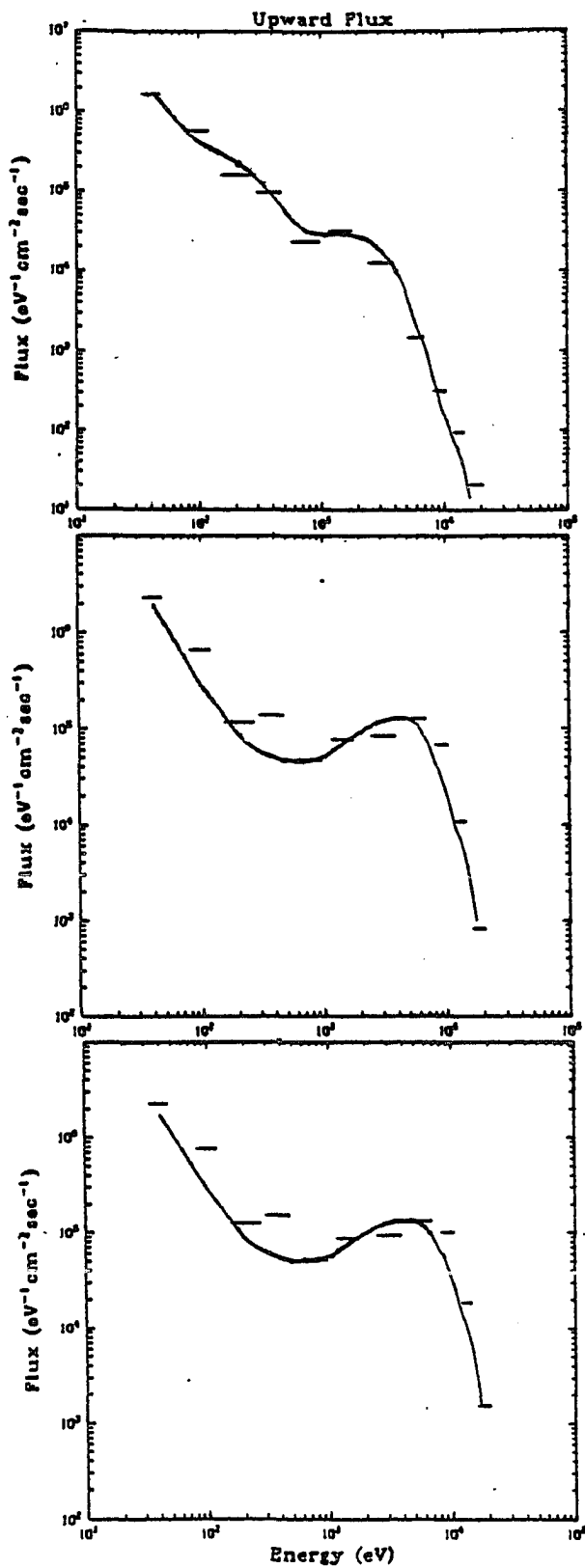
Fig 3.10 Upward flux (solid line) as calculated at the rocket altitude. The horizontal bars represent the measured flux. The top panel shows data set 26, the center panel shows data set 57, and data set 64 is displayed in the bottom panel.

Pulliam *et al.* (1981). In the context of the present work the discussion will concentrate on the differences in the angular distribution between the data and the transport equation results. The angular distribution at the altitude of the applied boundary condition is shown in Fig. 3.11a–c for 6 energy channels. The measured data are represented by crosses while the solid segments of a circle give the intensity of the 32 streams of the computation. The energy channels are individually normalized and the scale is indicated on the ordinate. The counting statistics yield errors between 1% and 3% in most cases. Only the highest energy channels have larger experimental errors.

Data set 26 shows the best agreement between measurements and the computations of the upward intensity (Fig. 3.11a). The downward field aligned electrons penetrate deep enough into the atmosphere to undergo multiple angular scattering until the distribution becomes almost isotropic. The backscattered intensity has lost the pronounced directional component. This is also shown by the measurements, except in the lowest energy sensors at 40 eV and 90 eV (only the 40 eV sensor is shown in Fig. 3.11a). At these energies the measurements indicate a stronger anisotropy in the upward intensity than suggested by the calculations. The same enhanced field aligned intensity is observed in the other two data sets. An analysis of 4 additional data sets supports the significance of this deviation of the theoretical results from the measurements.

Pulliam *et al.* (1981) reported that positive ions contributed less than 1% to the total particle and energy flux during the flight. The possibility that the additional electron intensity is due to ionization from precipitating protons can therefore be excluded.

To explore the reason for the inability of the transport code to reproduce the observed low energy anisotropy the effect of altering the phase functions has been studied. The elastic scattering is described by a screened Rutherford formula (see Chapter 3.2). At high energy the computations are in good agreement with the measured intensity, indicating that this choice of the phase function for elastic scattering is appropriate. The shape of
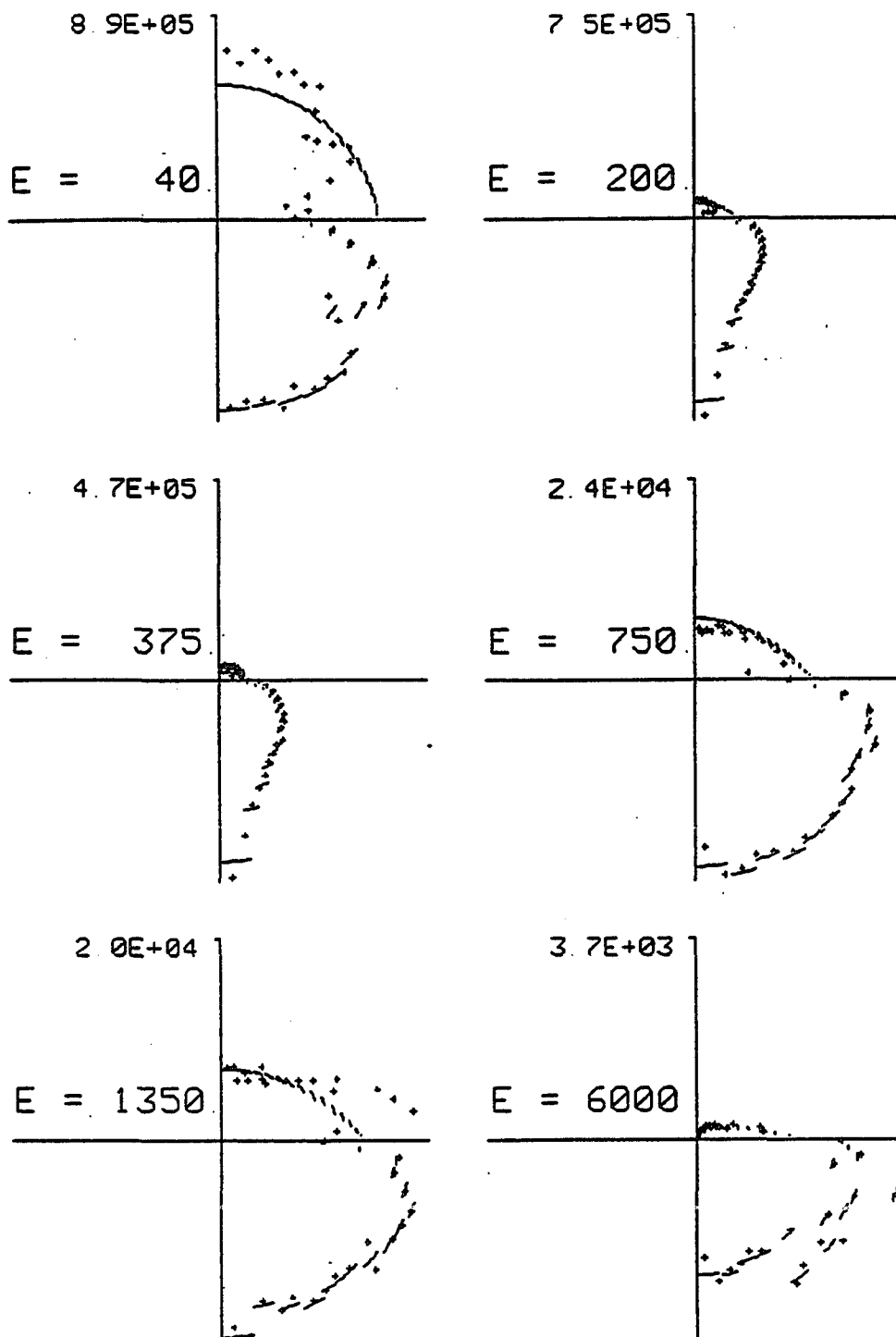
Fig. 3.11a   Comparison of the calculated intensity (solid lines) and the measured data (crosses) for 6 energy channels of data set 26. Each plot is normalized with the normalization factor shown on the ordinate.
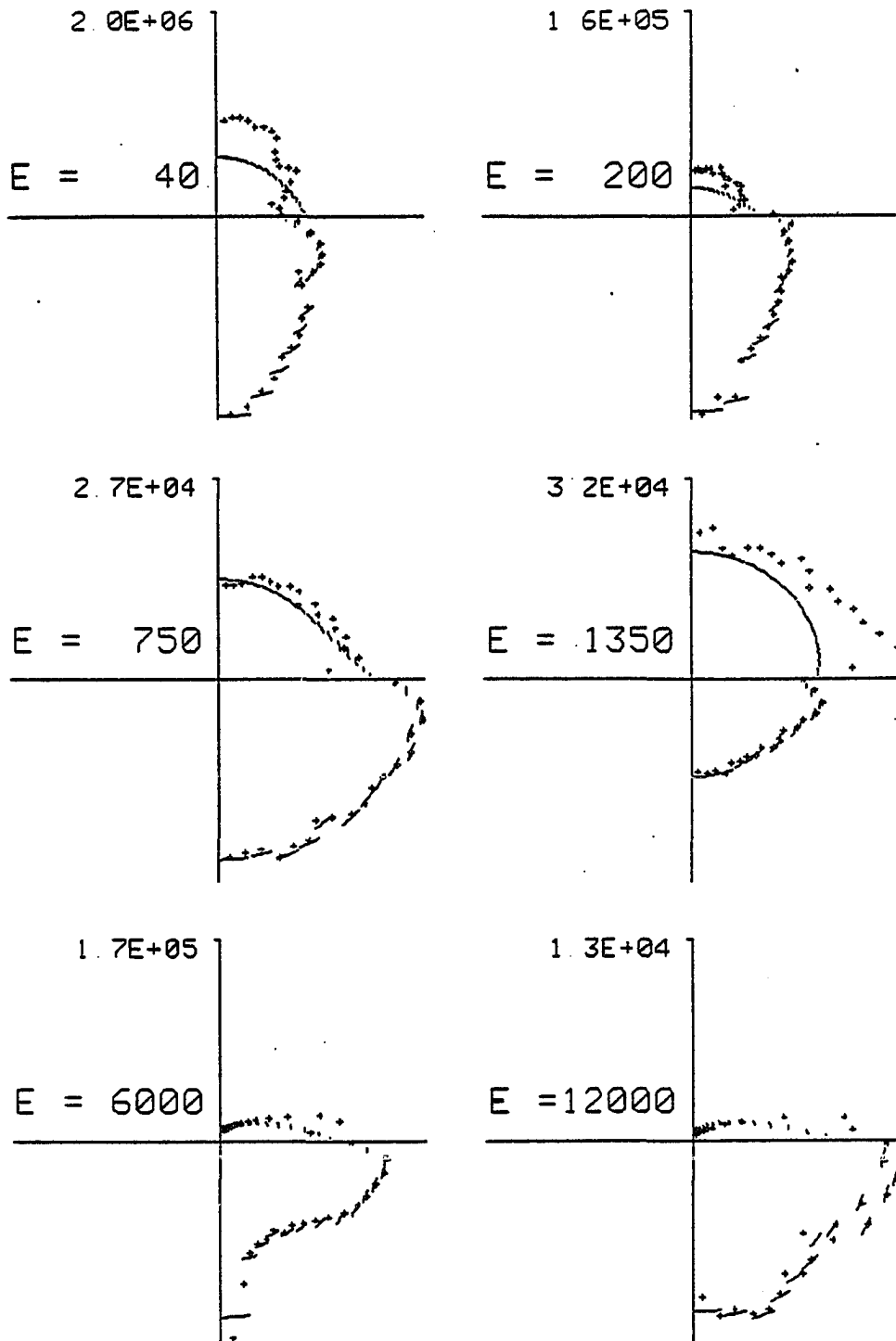
Fig. 3.11b Same as Fig. 3.11a for data set 57. Note that different energy channels are displayed.

1 2E+06

1 1E+05

E = 40

E = 200

2 9E+04

3. 4E+04

E = 750

E = 1350

1 3E+05

2. 1E+04

E = 6000

E = 12000
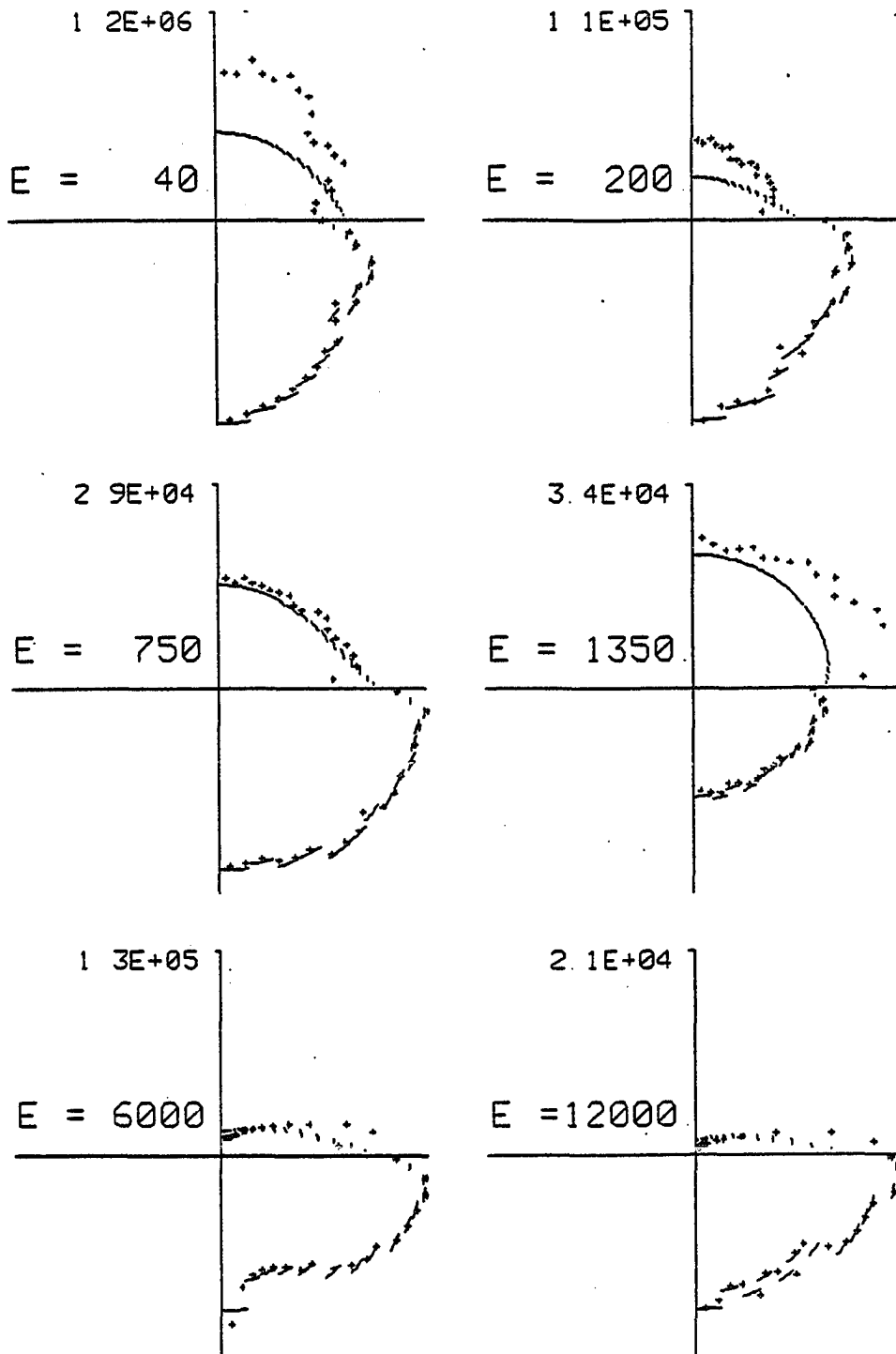
Fig. 3.11c   Same as Fig. 3.11a for data set 64.

the analytic formula deviates from measurements of the differential cross section by Shyn *et al.* (1972) only at low energy (less than 100 eV). The backscatter ratio, however, is in good agreement with laboratory data at all energies (Wedde and Strand, 1974).

The phase functions for inelastic collisions were assumed to be isotropic for production of secondary electrons and for the scattering of the degraded primaries a delta function in the forward direction was used. Laboratory measurements of double differential cross sections reveal a small backscattered component of the primaries (Cartwright *et al.*, 1977) and a preferred direction for the emerging secondary electrons (Opal *et al.*, 1972). For secondaries with an energy $E_{\text{sec}} \geq 75$ eV Opal *et al.* show a maximum of the phase function at $\approx 60°$ scattering angle. The transport code was modified to allow for alternate phase functions for both inelastic scattering of the primary and the production of secondaries. To demonstrate the insensitivity of the code to these changes the following phase functions were selected

$$p_{\text{sec}}(\mu) = \begin{cases} \delta(\mu - 0.5) & \text{for } E_{\text{sec}} \geq 75 \text{ eV} \\ 1 & \text{for } E_{\text{sec}} < 75 \text{ eV} \end{cases}$$

$$p_{\text{deg}}(\mu) = \begin{cases} \delta(\mu - 1) & \text{for } E \geq 100 \text{ eV} \\ \delta(\mu + 1) & \text{for } E < 100 \text{ eV}. \end{cases}$$

The angular distribution of the upward intensity at the rocket altitude remained almost unchanged, even with these radically unrealistic phase functions. Changes were observed only in the total upward flux which increased by $\approx 10\%$. This experiment suggests that the observed upward low energy anisotropy cannot be explained by inelastic angular scattering. Furthermore, it shows that the inelastic phase functions have little influence on the intensity, and the simplifications to forward and isotropic scattering for the degraded and secondary electrons are justified.

The second systematic discrepancy between the observed and calculated upward intensities occurs at high energies in the pitch angle range $75° - 85°$. This is apparent in data set 57 as well as 64 (Fig. 3.11a and b) in the sensors at 6000 eV and 12000 eV. The

analysis of other data sets confirms that this enhanced intensity has systematic character. The enhanced intensity occurs at high energies at or above the peak of the downward intensity. In this energy range the scattering phase function has a strong forward peak. It is unlikely that the observed discrepancy can be explained by scattering. The pitch angle distribution close to that of electrons at the mirror point suggests that these electrons are reflected by the converging magnetic field. This explanation also supports the enhanced intensity at the 1350 eV sensor. Electrons in this energy range experience more angular deflection by scattering than at higher energies and one might expect that the magnetic mirroring has less influence on the angular distribution. The enhanced intensity at high energy, however, will contribute to the intensity at lower energy by energy degradation. To obtain a quantitative statement as to whether the magnetic mirroring of electrons is sufficient to explain the observed intensity, the inhomogeneity of the magnetic field must be included in the transport calculation.

The present treatment of the transport equation does not include the interaction of electrons with electromagnetic fields. A study of whether or not an electric field can cause the observed anisotropy at low energies must be deferred to the future. Magnetic mirroring may be responsible for the large intensity in the pitch angle range $75° - 85°$ in the keV energy bins. To obtain a conclusive result the inhomogeneity of the magnetic field must be included in the code.

Chapter 4. Interpretation of Auroral Optical Observations

In the previous chapter *in situ* measurements of the electron intensity were compared to the calculations of the transport code. Electron intensity measurements in the ionosphere, however, require a large experimental effort. Satellite observations are insufficient and such measurements are limited to sounding rockets. This chapter is therefore concerned with indirect observations of auroral electrons through optical techniques.

4.1 Optical Emissions

Optical emissions in the aurora are generated when excited atoms and molecules decay to lower states. The main energy source for the excitation is the incident electron flux. The electron transport calculation provides a tool to calculate the photon intensity* of optical auroral emissions. However, the emission of a given feature is not equivalent to the electron impact excitation of the state whence it originates. Other mechanisms contribute to both the population and de-population of excited states. De-excitation occurs by quenching (collisional deactivation), dissociation, chemical reaction, and radiation. Besides direct electron impact, population of an excited state is possible by cascading, chemical reactions, photon absorption, and thermal electron excitation. In order to relate photon intensity to electron intensity it is expedient to select emission features that are caused directly by electron impact, eliminating the need to treat more complicated processes. Such emissions are often those which originate from states with a high threshold, since the energy that is

---

* The term intensity is used for electrons as well as photons. To distinguish between these two uses the term 'intensity', symbol I, applies to electrons while in the case of photons the term 'photon intensity', symbol I_λ, will be used.

transferred in chemical reactions is usually small (less than 10 eV). A high threshold also limits the population due to cascading from higher states.

Among these states are excited ion states and dissociation reactions like

$$O_2 + e^- \rightarrow O_2^* + e^- \rightarrow O + O(^3S^0) + e^-$$

followed by

$$O(^3S^0) \rightarrow O(^3P) + h\nu \qquad (1304\text{Å}).$$
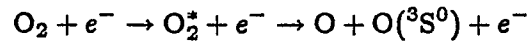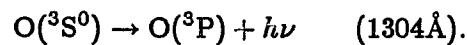
The entire process is characterized by an emission cross section which is defined by the cross section for emitting a photon of a given wavelength upon electron impact. For the OI(1304 Å) triplet, the emission cross section has been measured by Ajello (1971) in a laboratory experiment. In addition to the dissociation process, direct excitation of the $O(^3S^0)$ state by

$$O + e^- \rightarrow O(^3S^0) + e^-$$
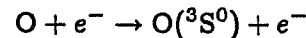
contributes to the 1304 Å radiation. Both processes are important in the aurora and, depending on the altitude of the emission, each may be the dominant source of I_{1304}. A similar situation occurs for the OII 4416 Å emission which also has two sources for the upper state $O^+(^2D^0)$, through dissociative ionization of O_2 and through direct ionization of atomic oxygen. Haasz and DeLeeuw (1976) have measured the emission cross sections for both processes and concluded that the direct ionization $O + e^- \rightarrow O^+(^2D^0) + 2e^-$ is the dominant mechanism for the OII 4416 Å emission.

The excitation rate $\eta(z)$ for a state with a known cross section $\sigma(E)$ of a species with density $n(z)$ is calculated from the intensity by

$$\eta(z) = 2\pi n(z) \int_0^\infty dE \int_{-1}^1 I(z, E, \mu)\sigma(E)\, d\mu. \qquad (4.1)$$

Substituting the emission cross section for the excitation cross section in Eq. (4.1), one can define an emission rate $\eta_\lambda(z)$. In many cases the emission cross section has the same energy dependence as the excitation cross section for the state whence the emission originates, and it can be given as a fraction of the excitation cross section of the higher state.

An example for an emission that results from an excited ion state is the N_2^+ first negative band system (N_2^+ 1N). The emission cross section for the (0,0) band at 3914 Å has been measured by Borst and Zipf (1970). They compared it to the ionization cross section and found an almost constant ratio of $\sigma^{ion}/\sigma^{3914} \approx 14.1$. The branching ratio for the upper state $N_2^+(B^2\Sigma_u^+)$ (see Table 2) as well as the emission cross section for the remaining bands of the system are calculated by applying the Frank-Condon factors (Vallance Jones, 1974). The same method is used for the O_2^+ first negative band system (O_2^+ 1N) which originates from $O_2^+(b^4\Sigma_g^+)$ (Zipf et al., 1985).

The emission cross sections of the LBH bands (Lyman-Birge-Hopfield) have been measured by Ajello and Shemansky (1985). The emission results from the $N_2(a^1\Pi_g \to X^1\Sigma_g^+)$ transition. From the close agreement between the $N_2(a^1\Pi_g)$ cross section measurements of Ajello and Shemansky, which is based on the LBH emission, and the electron energy loss experiment by Cartwright et al. (1977), it can be inferred that cascading from higher states contributes less than 5% to the emission. The direct relationship between electron impact and emission makes the LBH bands a good candidate for analysing optical data in terms of electron fluxes. Two additional advantages favour the LBH bands; they are bright auroral spectral features and they are in a wavelength range (1273–2550 Å) where the measurement is not contaminated from scattered sunlight or auroral light backscattered from the ground or from clouds.

If such observations are made by means of photometers with broad filters as on the Dynamics Explorer (DE-A) spacecraft (Frank et al., 1981), the other emissions that fall into the same wavelength range have to be known as well. For the filters that are deployed

on the UV imaging instrument of the DE-A these are the OI lines at 1304 Å and 1356 Å, and nine NI lines between 1200 Å and 1744 Å (see Table 3). The two source mechanisms for the OI(1304 Å) emission have already been mentioned. The OI(1356 Å) emission stems from the $O(^5S)$ to ground state transition and the emission cross section is nearly equivalent to the excitation cross section (Stone and Zipf, 1973). Emission cross sections for the NI lines from electron impact on N_2 at 100 and 200 eV have been measured by Ajello and Shemansky (1985). The energy dependence of the emission cross sections is assumed to be proportional to the dissociation cross section of N_2.

Ground based or satellite optical instruments measure the surface brightness, which is given for an optically thin atmosphere by the integral of the volume emission rate along the line of sight. For an arbitrary viewing angle this requires knowledge of the spatial distribution of the emission rate. Field aligned optical observations take advantage of the inherent field aligned structure of the aurora. The surface brightness I_λ is then obtained by the integral

$$I_\lambda = \int_0^\infty \eta_\lambda(z) \frac{dz}{\cos\alpha},$$

where α is the angle between the magnetic field and vertical. For emissions for which the atmosphere is optically thick the calculation of the surface brightness involves the radiative transfer from the emitting volume through the atmosphere. Absorption by Schuman-Runge bands and continuum of O_2 becomes important in the ultraviolet, while in the visible the atmosphere can be assumed to be optically thin. When absorption is included in the calculation of the nadir surface brightness, the photon intensity I_λ at satellite altitude z_{sat} is expressed by

$$I_\lambda = \int_0^{z_{sat}} \exp\left(-\sigma_\lambda \int_z^{z_{sat}} n(z')\,dz'\right) \eta_\lambda(z)\,dz,$$

where σ_λ is the extinction cross section and $n(z)$ is the density of the absorber. The O_2 absorption cross section in the wavelength region from 1050 Å to 1800 Å has been measured by Metzger and Cook (1964).

A different problem arises for the transfer of OI(1304 Å) radiation which undergoes resonant scattering, i.e. the atmosphere is optically thick but the absorber (atomic oxygen) re-emits the 1304 Å photon, changing the internal structure of the 1304 Å line and the directional behavior of the radiation. Meier and Lee (1982) solve the resonant scattering transport with a Monte Carlo simulation for a photoelectron and a solar source. In an atmosphere model represented by a horizontal slab all of the radiation is eventually transported to the upper and lower boundary. The ratio of the photon intensity at the lower boundary to the photon intensity at the upper boundary depends on the altitude distribution of the primary source. To avoid the lengthy Monte Carlo simulation, an estimate of the effect of resonant scattering is obtained from the work of Strickland and Anderson (1977). This estimate is valid only for nadir looking spacecraft, and establishes a relationship between the altitude of the photon production maximum, z_{max}, and the resonantly scattered photon intensity I_{1304} that escapes at the top of the atmosphere. The formula

$$I_{1304} = \left(5 \cdot 10^{-3} z_{max} + 1.125\right) \eta_{1304}$$

where η_{1304} is the photon column production rate, is derived from Fig. 2 of Strickland and Anderson (1977) and is valid for altitudes 100 km $\leq z_{max} \leq$ 400 km.

The $N_2(C^3\Pi_u)$ state decays by cascading to $N_2(B^3\Pi_g)$. The optical emissions associated with this transition are the N_2 second positive bands (N_2^+ 2P). About 90% of the excitation of the upper state is caused by electron impact. Approximately 10% cascading from higher states contributes to the second positive emissions (Tachibana and Phelps, 1979). A summary of the emission cross sections included in this work is presented in tabulated form in Table 3.

Table 3
Summary of Emission Cross Sections

Band System or Multiplet	Electronic Transition	Wavelength (Å)	Reference
Molecular Nitrogen			
LBH	$a^1\Pi_g \rightarrow X^1\Sigma_g^+$	1273-2550	Ajello and Shemansky, 1985
2P	$C^3\Pi_u \rightarrow B^3\Pi_g$	2685-4917	Borst and Zipf, 1970
1N	$B^2\Sigma_u^+ \rightarrow X^2\Sigma_g^+$	3308-5865	Tachibana and Phelps, 1979
Molecular Oxygen			
1N	$b^4\Sigma_g^- \rightarrow a^4\Pi_u$	4987-9716	Zipf *et al.*, 1985
Atomic Nitrogen			
NI	$^4P \rightarrow {^4S^0}$	1200	Ajello and Shemansky, 1985
NI	$^2D \rightarrow {^2P^0}$	1227	_"_
NI	$^2D \rightarrow {^2D^0}$	1243	_"_
NI	$^2D \rightarrow {^2P^0}$	1311	_"_
NI	$^2P \rightarrow {^2P^0}$	1319	_"_
NI	$^2P \rightarrow {^2P^0}$	1327	_"_
NI	$^2D \rightarrow {^2P^0}$	1412	_"_
NI	$^2P \rightarrow {^2D^0}$	1493	_"_
NI	$^2P \rightarrow {^2P^0}$	1744	_"_
NII(19)	$^3F^0 \rightarrow {^3D}$	5001	Filippelli *et al.*, 1982
NII(3)	$^3D \rightarrow {^3P^0}$	5680	_"_
Atomic Oxygen			
OI	$^3S^0 \rightarrow {^3P}$	1304	Ajello 1971
OI	$^5S^0 \rightarrow {^3P}$	1356	_"_
OI(5)	$^3P \rightarrow {^3S^0}$	4368	Julienne and Davis, 1976
OII(5)	$^2D^0 \rightarrow {^2P}$	4416	Haasz and DeLeeuw, 1976
OI(4)	$^3P \rightarrow {^3S^0}$	8446	Julienne and Davis, 1976

4.2 Interpretation of Emissions in Terms of Electron Spectra

The optical emissions in an aurora depend on the spectrum of the precipitating electrons, the scattering cross sections, the emission cross sections and the density of the atmospheric species. These parameters are inputs to the transport calculation that predicts the optical emissions. In order to invert this calculation, and infer some geophysical parameters from the observed optical emissions, the electron spectrum and the atmospheric density are parameterized, and a relationship between these parameters and the photon intensities is sought. Excitation cross sections and emission cross sections can be inferred from laboratory measurements and there will be no attempt to improve these results from auroral observations. The neutral densities are based on the MSIS-83 empirical model, which takes into account variations with geographic location, magnetic and solar activity, date, and time. It has already been mentioned in section 3.2 that the MSIS-83 densities may not always be applicable at high latitudes during periods of auroral activity. A one parameter correction is therefore applied by multiplying the MSIS-83 densities adopted in the transport calculation with a constant scaling factor. Strickland *et al.* (1986) have also suggested modification of the scale height for atomic oxygen. In this work, however, only a constant scaling of the density is considered.

The spectral characteristics of the electron precipitation are most important for inferring the optical emissions. To describe the electron spectrum completely an infinite number of parameters is required. It will be shown, that for the purpose of calculating height integrated emission rates in the framework and under the restrictions of the current electron transport model, it is sufficient to describe the electron spectrum by its first two energy moments, the particle flux and the energy flux.

To explore the sensitivity of the model to the choice of the spectrum of the precipitating electrons, the effects of two synthetic spectra introduced in section 3.3 (Maxwellian and
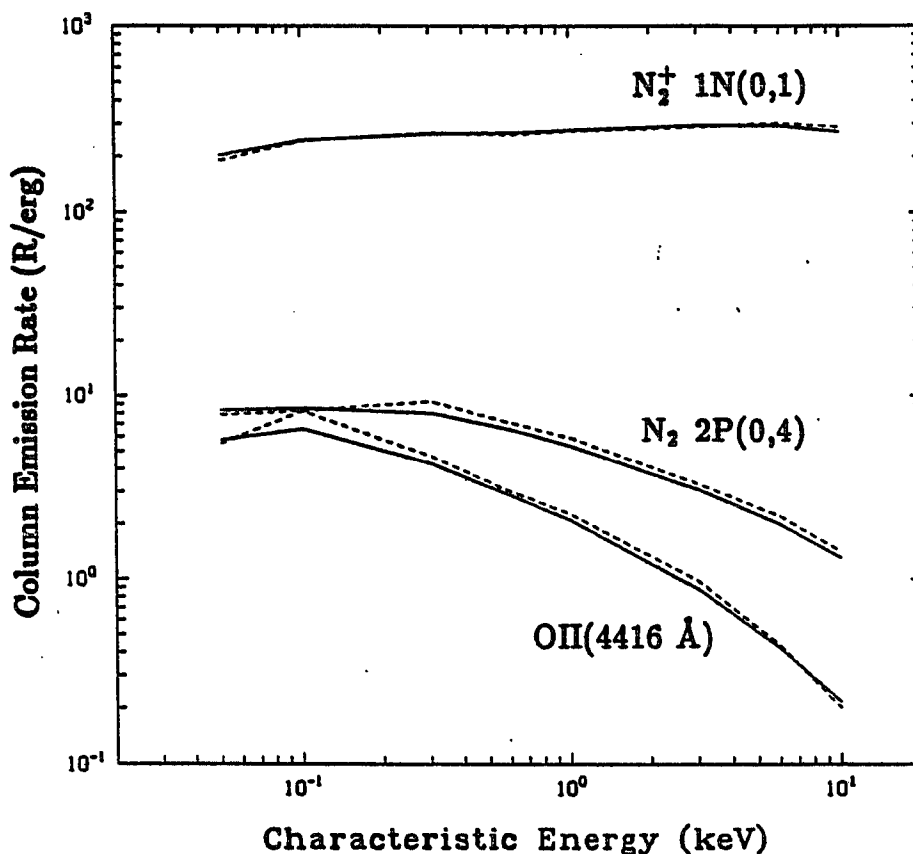
Fig. 4.1 Column emission rates of the N_2^+ 1N(0,1) band at 4278 Å, the N_2 2P(0,4) band at 4344 Å, and the OII line group at 4416 Å as a function of E_{char} for an electron energy flux of $F_E^- = 1$ erg $cm^{-2}sec^{-1}$. Solid lines result from precipitating Maxwellian spectra, dashed lines from monoenergetic spectra.

monoenergetic) are compared. Both spectra are characterized by the same total energy flux F_E^- and characteristic energy E_{char}, while the higher energy moments are very different. Both the transport equation and the equation from which the emission rates are calculated are linear in the intensity I, so that F_E^- scales linearly with the emissions. The response of an emission to E_{char} depends on two effects: (a) the penetration of the electrons into the atmosphere increases with E_{char}, thus the emission originates from regions of varying composition, and (b) the emission cross sections are a function of the electron energy.

The height integrated emission rates of the N_2^+ 1N(0,1) band at 4278 Å, the N_2 2P(0,4) band at 4344 Å, and the OII line group at 4416 Å are plotted in Fig. 4.1 as a function of E_{char}. The energy flux at the top of the atmosphere is $F_E^- = 1$ erg cm^{-2}sec^{-1}. Maxwellian (solid lines) and monoenergetic (dashed lines) spectra for boundary conditions yield the same photon intensity for a given E_{char}. The emission cross sections have their maximum at energies where the electron intensity is dominated by secondary or energy degraded electrons. The inelastic scattering reshapes the electron spectrum fast enough that the higher energy moments of the incident electron spectrum at the top of the atmosphere have no effect on the column emission rates. The altitude distribution of the volume emission rates, however, does depend on the shape of the incident electron spectrum. Electrons with a monoenergetic (Gaussian) spectrum penetrate deeper into the atmosphere than electrons with a Maxwellian spectrum of the same energy flux and E_{char}, and energy is deposited in a narrower height range. Fig. 4.2 shows the emission rate of N_2^+ 1N (4278 Å) as a function of altitude for several Maxwellian incident spectra which are distinguished by E_{char}.

The N_2^+ 1N emission is nearly independent of E_{char} as shown in Fig. 4.1. The value of 200–300 R/(erg cm^{-2} sec^{-1}) is in good agreement with satellite observations which monitored the energy flux as well as the characteristic energy and the 4278 Å photon intensity (Kasting and Hays, 1977, and Rees and Abreu, 1984). Because of its independence of E_{char} this emission can be directly related to the total energy flux F_E^- of the precipitating electrons. The N_2 2P emission on the other hand shows a variation with E_{char} due to the different energy dependence of the emission cross section. The energy flux and the characteristic energy of the incident electrons may therefore be determined from the ratio of these two emissions together with the absolute photon intensity of the 1stneg. band. Since both emissions originate from the same species, this ratio is independent of the atmospheric composition. This is demonstrated in Fig. 4.3, which shows the I_{4278}/I_{4344} ratio for two different atmospheres. The first is generated by MSIS-83 for a disturbed day
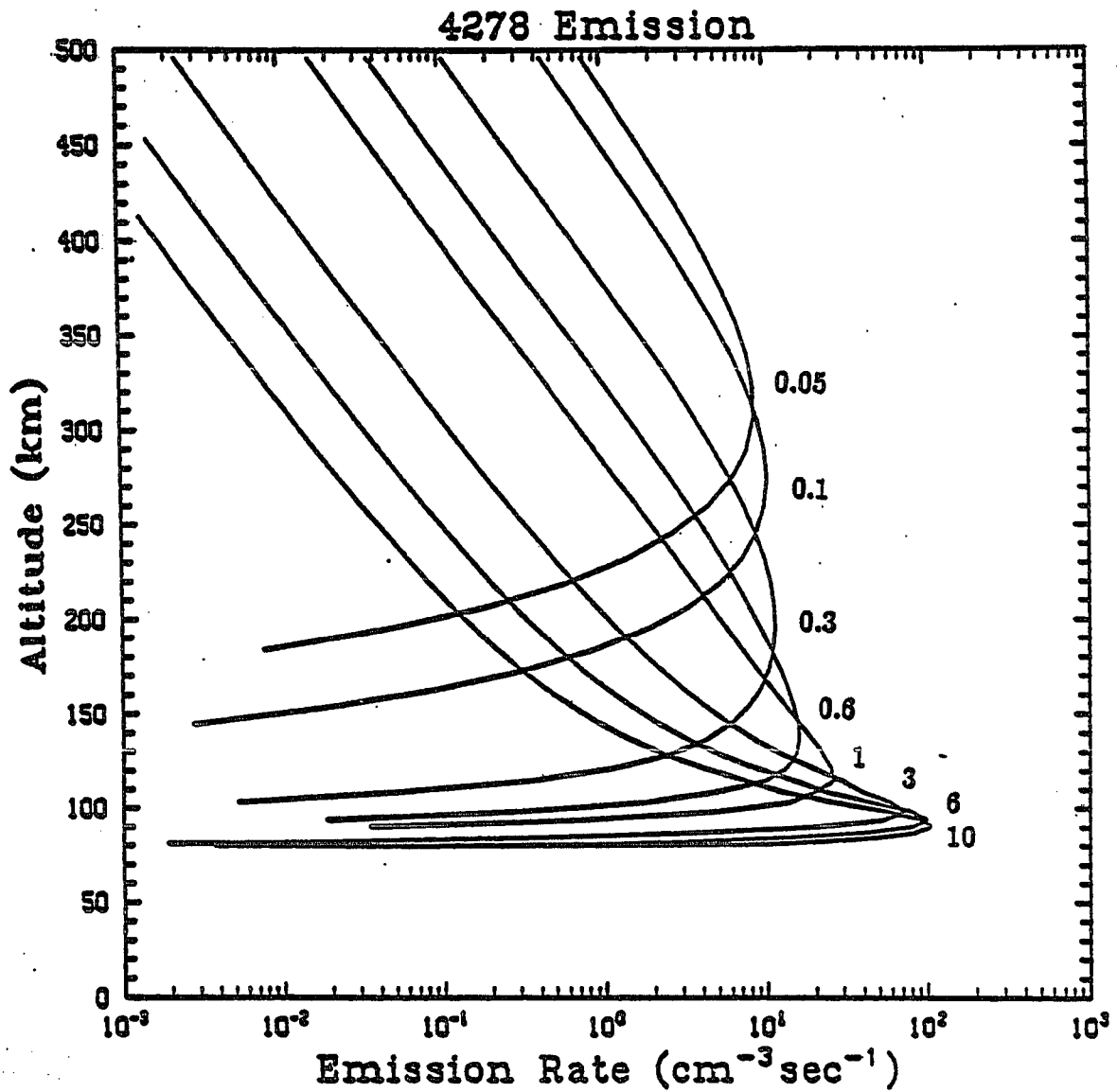
Fig. 4.2 Altitude distribution of the N_2^+ 1N volume emission rate at 4278 Å for precipitating Maxwellian electron spectra. The profiles refer to electron spectra with E_{char} ranging from 0.05 keV to 10 keV and energy flux of $F_E^- = 1$ erg cm^{-2}sec^{-1}.
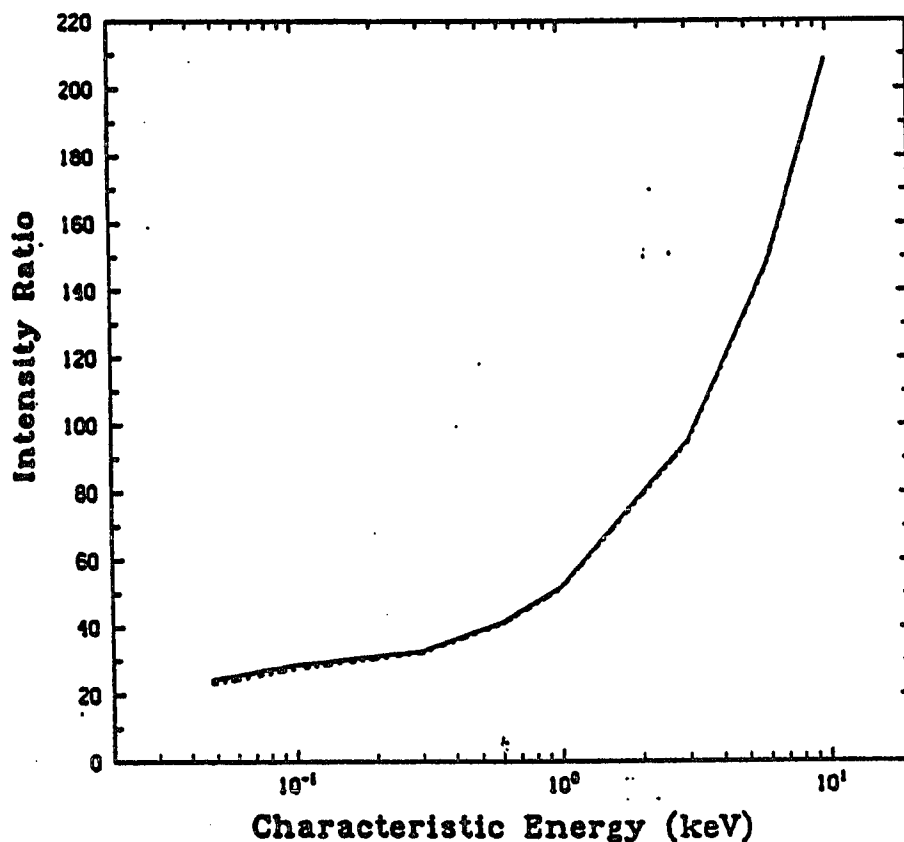
Fig. 4.3 Ratio of the column emission rates I_{4278}/I_{4344}. The solid line refers to a calculation based on a MSIS-83 density distribution of a disturbed day, the dashed line refers to a quiet day.

(1979, day 115) with an exospheric temperature of $T_{exo} = 1500°K$, the other is from a quiet day (1976, day 202) with $T_{exo} = 840°K$. Only minute differences are introduced by the change in the atmospheric composition.

The ability to infer characteristics of the electron spectrum without knowledge of the atmospheric composition opens up the possibility of using the transport calculation to infer ionospheric parameters from auroral optical observations.

4.3 Application of the Electron Transport Results to Auroral Images

The two Dynamics Explorer satellites (DE-A and DE-B) were launched in the summer of 1981 and operated successfully. The DE-A was launched into a high altitude orbit and carried an auroral imaging system (Spin-scan Auroral Imager: SAI). A description of the SAI instrument is given by Frank *et al.* (1981). Images of the entire auroral oval are obtained simultaneously in three wavelength regions with a temporal resolution of one frame every 12 minutes. Three scanning photometers are equipped with filters which may be changed during the flight. Two photometers are sensitive in the visible wavelength range and have, among others, filters to observe the OI 5577 Å and the OI 6300 Å emission. The third photometer is sensitive in the UV. The filters of the UV-photometer that are of interest here, are the 136W filter with a cutoff at $\lambda \approx 1360$ Å designed to monitor the LBH bands of N_2, and the 123W filter with a cutoff at $\lambda \approx 1230$ Å, which in addition to the LBH bands transmits the OI 1304 Å and OI 1356 Å emission lines. Several NI emissions also lie in this wavelength region.

All major emissions in the sensitivity range of the two UV-filters are calculated in the electron transport code. Including Schuman Runge absorption and resonant scattering of the OI 1304 Å triplet, the surface brightnesses of all major emissions at a satellite altitude of 800 km are plotted in Fig. 4.4 as a function of the characteristic energy. The calculations are based on Maxwellian electron spectra with an energy flux of 1 erg cm^{-2} sec^{-1}. The curve labeled NI includes nine NI emissions in the range 1200 Å to 1744 Å, the curve labeled LBH represents the sum of 104 LBH bands ranging from 1273 Å to 2550 Å, and the curve labeled OI 1304 Å includes both, direct excitation of O and excitation via O_2 dissociation. The OI 1356 Å emission is not shown, because it is much smaller than
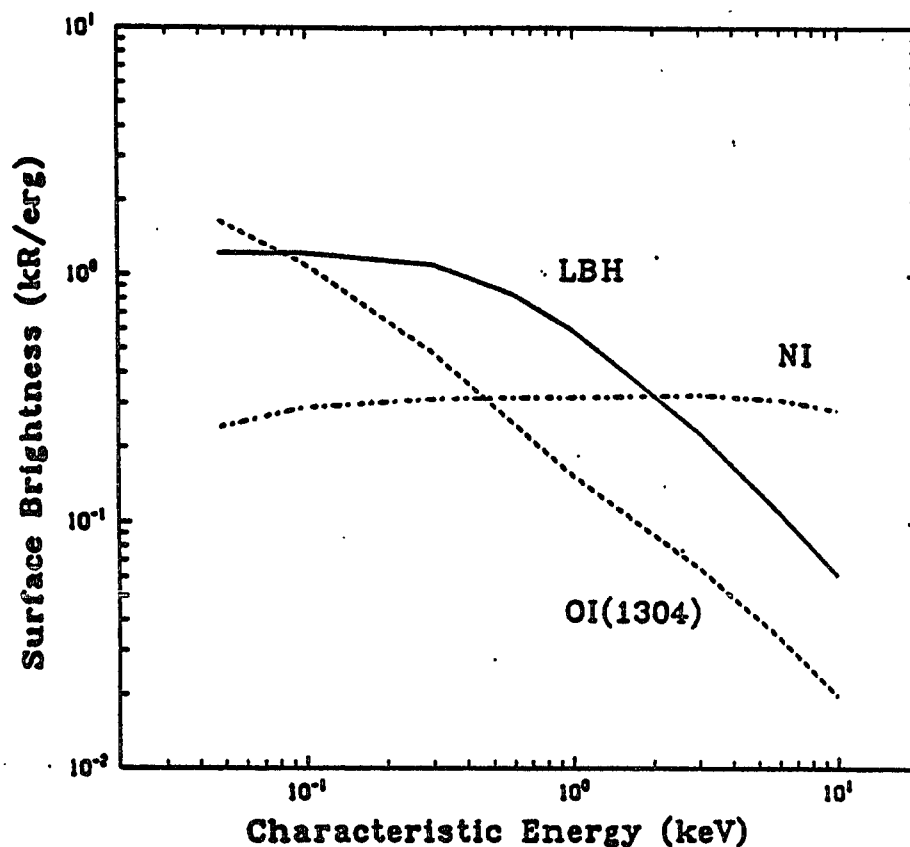
Fig. 4.4 Surface brightness for a nadir looking instrument at 800 km altitude of the major UV emissions in the sensitivity range of the DE-A UV-imager. The emissions are calculated from Maxwellian electron spectra with an energy flux of 1 erg cm^{-2} sec^{-1}. The surface brightness has been corrected to account for absorption by O_2 in the Schuman Runge bands and continuum.

the plotted emissions. It is, however, included in the calculation of count rates of the instruments.

Using the wavelength dependent calibration factors of the SAI instrument with the 123W and 136W filters (Rairden *et al.*, 1986), the surface brightness can be converted into count rates. Fig. 4.5 shows the count rates as a function of E_{char}. Both filters are broad passband filters. The filters are designed to be sensitive primarily to the LBH emissions (136W) and the OI lines (123W). With changing ratios between the OI and LBH photon intensities, the relative contribution of the different emissions to the count
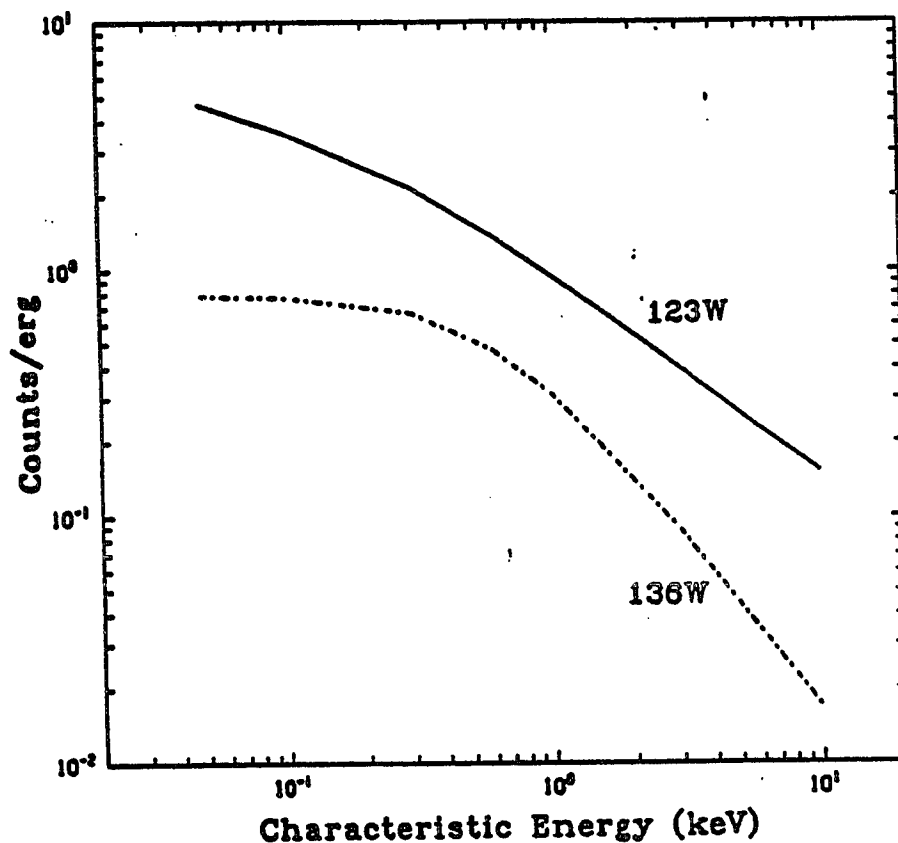
Fig. 4.5   Count rates of the UV-imager with the 123W and 136W filter that result from the surface brightness shown in Fig. 4.4 as a function of characteristic energy.

rate changes with E_{char} and with the atmospheric composition. Fig. 4.6 shows the relative contribution of the major emissions for the 123W and 136W filters as a function of E_{char}. The emissions are calculated for a MSIS-83 atmosphere (1979, day 115) but with the atomic oxygen density multiplied by 1/2. This scaling follows the practice of other authors, as mentioned in section 3.2. The wavelength range admitted by the 'LBH' filter (136W) shows little contamination from the OI emissions, but the passband of the 'OI' filter (123W) has substantial contamination from the LBH and NI emissions. Because of the variation of the contamination with E_{char}, it is not possible to infer the OI and LBH emission rates by simply applying a calibration factor to the count rates of the respective photometers.
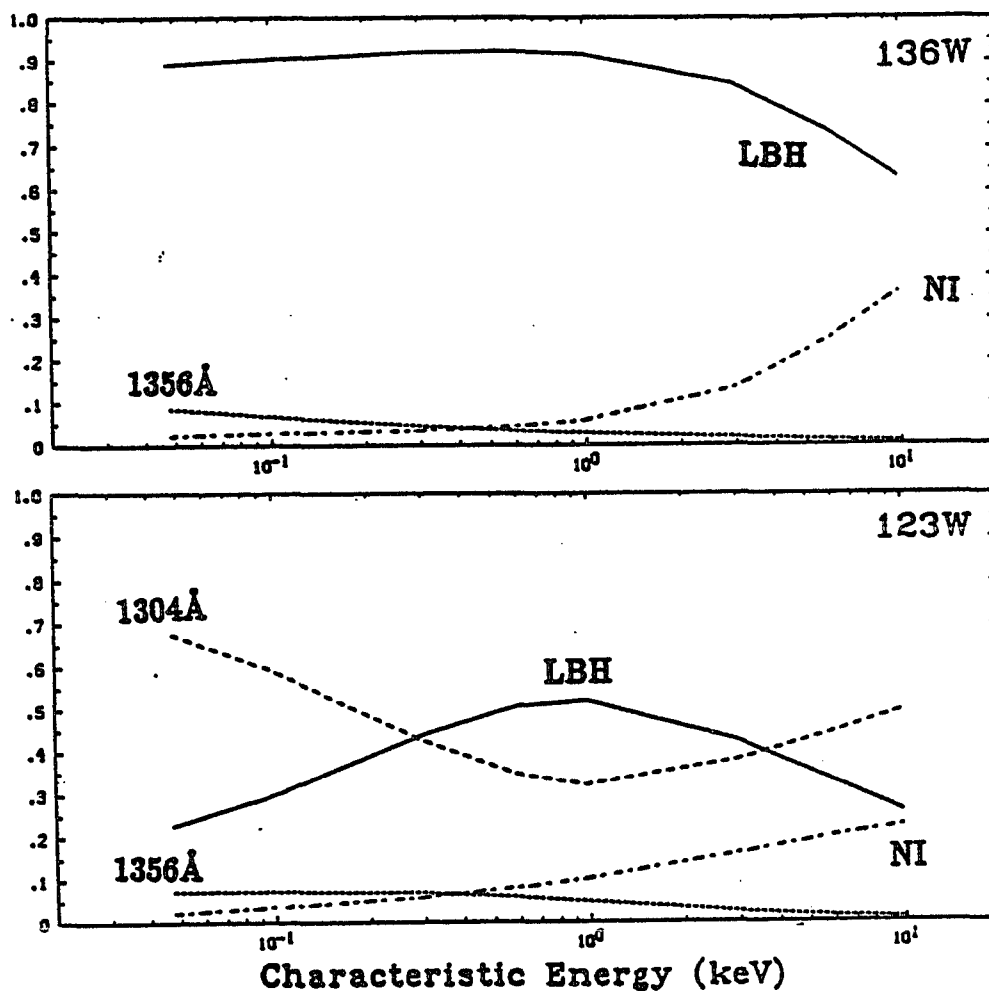
Fig. 4.6 Relative contribution of the LBH (solid line), NI (dash-dot), and OI (1304 Å: dashed, 1356 Å: dotted) emissions to the UV-imager. The top panel gives the relative contributions for the 136W filter, the bottom panel is for the 123W filter.

The second satellite, DE-B, was launched into a low altitude orbit. Among others, it carried an instrument to measure the electron intensity (LAPI). This instrument had 15 detectors covering the entire pitch angle range simultaneously (Winningham *et al.*, 1981). The temporal resolution of the intensity data is 1 sec. At satellite velocities of several kilometers per second this translates to a spatial resolution of the LAPI instrument that is coarser than the width of auroral optical features.

The SAI instrument acquires the images with scanning photometers. Each image is composed of 120 scan lines. A single scan takes 6 sec, which makes the time to acquire an entire image 12 minutes. The size of the area in the ionosphere that is imaged onto a single pixel depends on the altitude of the satellite. For the fall of 1981, when the apogee of DE-A was over the northern hemisphere at about 3-4 R_E altitude, the entire northern auroral oval could be imaged. In this case a single pixel refers to an area in the ionosphere of approximately 100 km diameter. The interpretation of the count rate as a surface brightness requires that the field of view of the instrument is filled. With a pixel size of 100 km, this will only be the case in rare circumstances. The resonant scattering of OI 1304 Å helps to fill the field of view even if the primary emission is confined to a small area, but the other UV emissions are likely to be underestimated. Both the LAPI and SAI instruments therefore yield data which represent averages over areas large compared to optical auroral structures.

The following paragraphs present an analysis of one SAI image; the LAPI instrument observed the electron intensity in temporal and spatial coincidence with one of the pixels of the image. This SAI image (day 326, 1981 at 7:53 UT) is displayed in Fig. 4.7 as a contour map of counts in the UV-photometer with the 123W filter. The dashed lines give the geographic coordinates. The auroral oval is clearly evident and extends to the dayside. Since the 123W filter includes the OI 1304 Å triplet, the sunlit atmosphere contributes to the photometer counts from scattered sunlight and the analysis is limited to the section of the auroral oval in the dark ionosphere. The LAPI instrument passed through the evening side of the auroral oval. Fig. 4.8 is an enlarged excerpt of the image showing the region where the LAPI coincidence occurred. The numbers give the count rates of the UV-photometer, and their position refers to the center of the pixel that they represent. The times at which these pixels were scanned are indicated at the right end of each scan. Adjacent pixels in a scan line are 3.4 msec apart, so that the pixels that compose the

section of a single scan line in the excerpted frame can be thought of as being taken instantaneously. Also indicated is the ground track of the DE-B satellite, which crossed the auroral oval at 450 km altitude equatorward.

The observed LAPI electron spectrum around 7:53 UT shows large variations, even at the resolution of 1 sec. The energy flux and the characteristic energy of the precipitating electrons from 7:53:03 to 7:53:14 is shown in Fig. 4.9. Rather than averaging over the time that corresponds to the space which is imaged onto a single pixel (approximately 14 sec), the spectrum at 7:53:11 UT (see Fig. 4.10) is adopted as a boundary condition for the electron transport calculation. A single spectrum, which by itself is an average over several kilometers, is more likely to represent the auroral electrons than an even larger average. The transport calculation is carried out with an angular resolution of 8 streams, although the measured boundary condition is almost isotropic over the downward direction. The MSIS-83 atomic oxygen density is scaled by a factor of 0.75. The calculated emissions yield a count rate of 5.7 for the 123W filter. To compare this number with the observed count rate, the pixel that corresponds to the geomagnetic position of the LAPI instrument has to be used. Assuming that the main emission occurs at an altitude of 100 km, the pixel that corresponds to the LAPI position yields 6 counts (see Fig. 4.8). This agreement lends confidence for further interpretation of the image.

In order to infer the energy flux and characteristic energy at other locations in the image, the information from the UV-photometer alone is insufficient. The count rate has a strong variation with E_{char} (Fig. 4.5). To obtain the energy flux independent of the UV image, analysis of data acquired by one of the photometers operating in the visible wavelength region is attempted. One of the other two photometers composed an image of the OI 5577 Å emission scanning parallel to the UV-photometer, which ensures that the pixels in the two images are reasonably coincident in time and space. The third photometer (6300 Å) scanned the image in the opposite direction, and its data cannot be compared

90°E

180°

0°

90°W
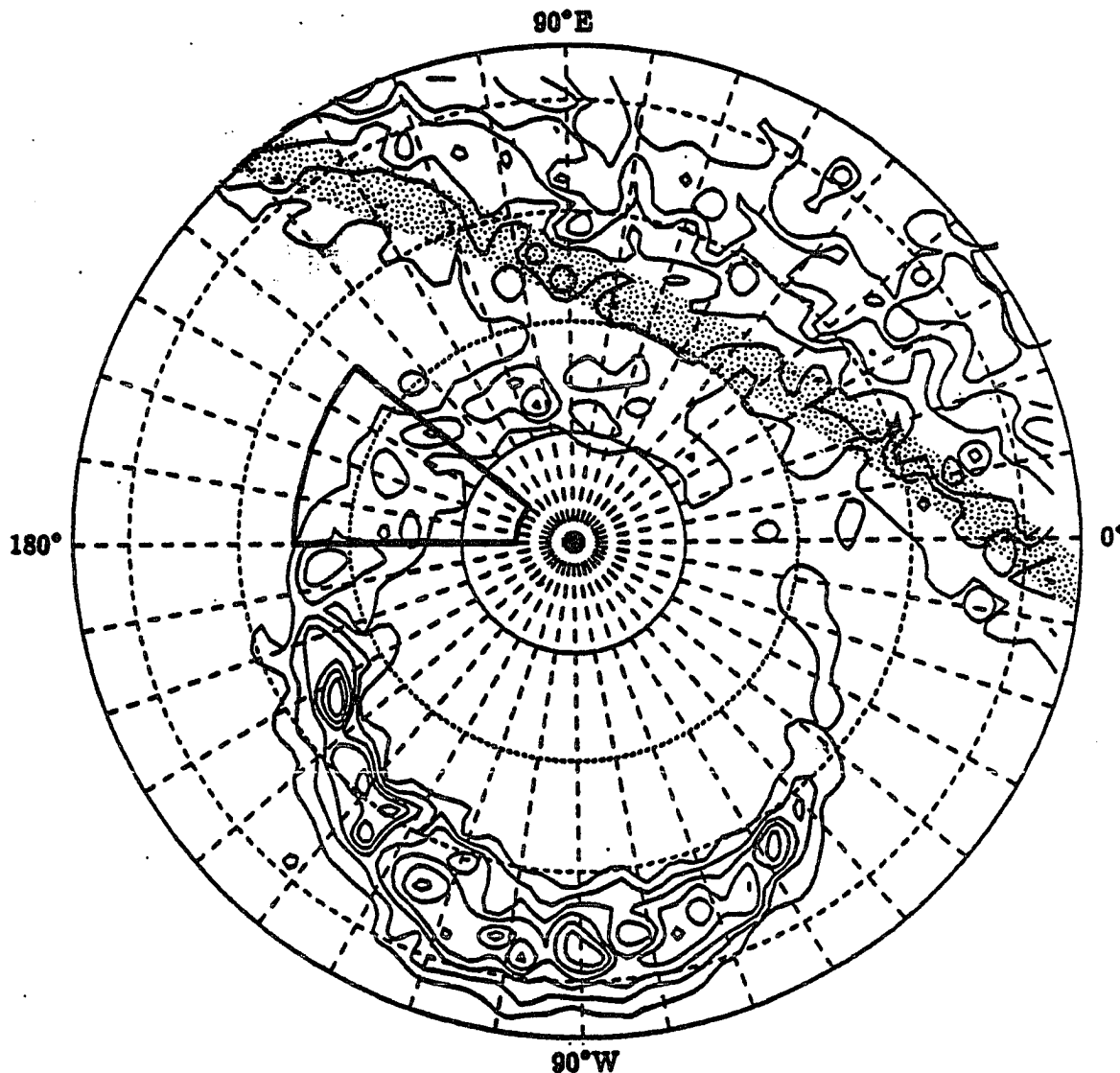
Fig. 4.7 SAI image of the northern hemisphere auroral oval on day 326, 1981, 7:47 UT to 7:59 UT. The contour lines of constant count rate of the UV-photometer with the 123W filter are projected onto geographic coordinates. The latitude-longitude grid (dashed lines) is plotted in increments of 10°, and the terminator (solar zenith angle of 90°) is indicated. The contour lines are given in increments of 4 counts. The thick line marks the section of the auroral oval that is enlarged in Fig. 4.8.
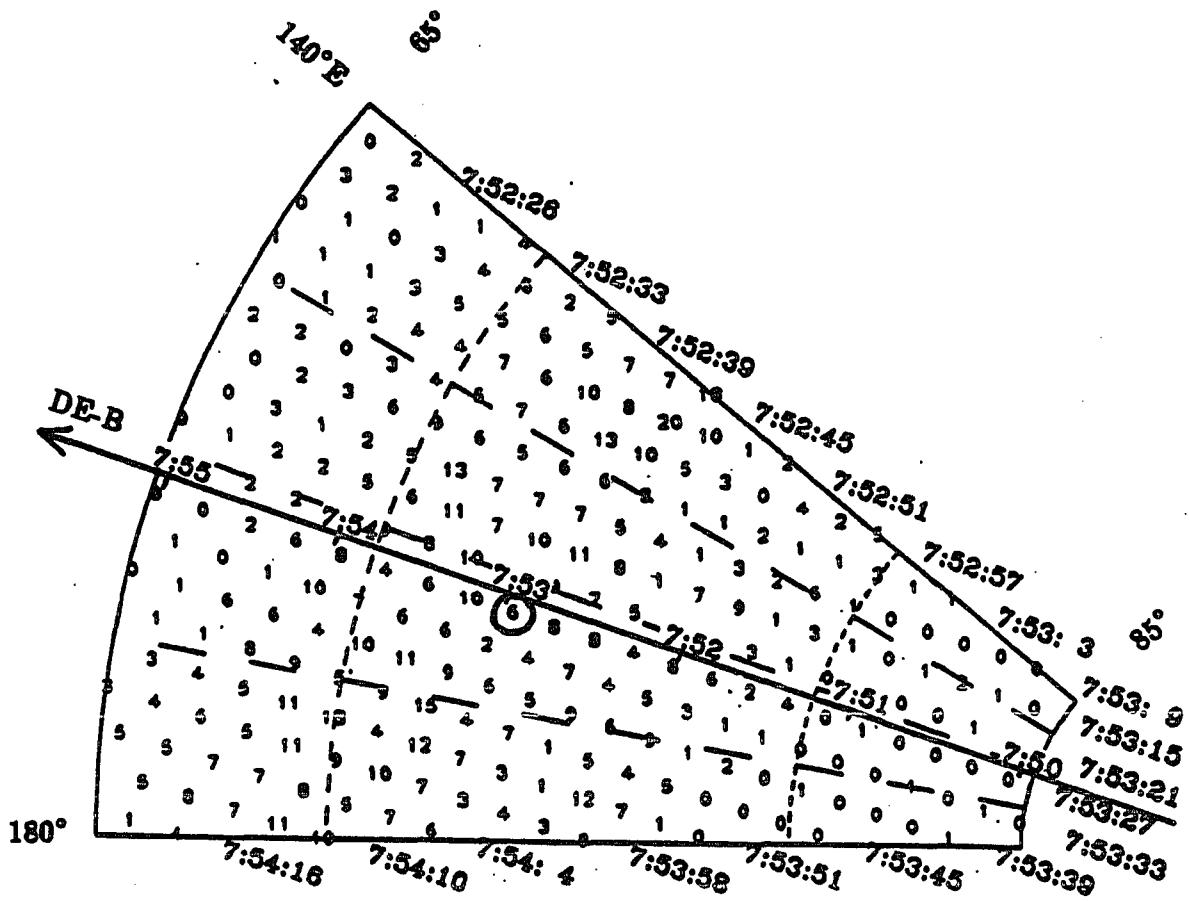
Fig. 4.8   Enlarged section of the image in Fig. 4.7 (latitude: 65°–85°, longitude: 140°E–180°). The numbers give the counts in the UV-imager. The times of the corresponding scan lines are given at the right edge. Also indicated is the ground track of the DE-B satellite with time marks. The pixel that refers to the same geomagnetic position as DE-B at 7:53:11 UT is marked by a circle.
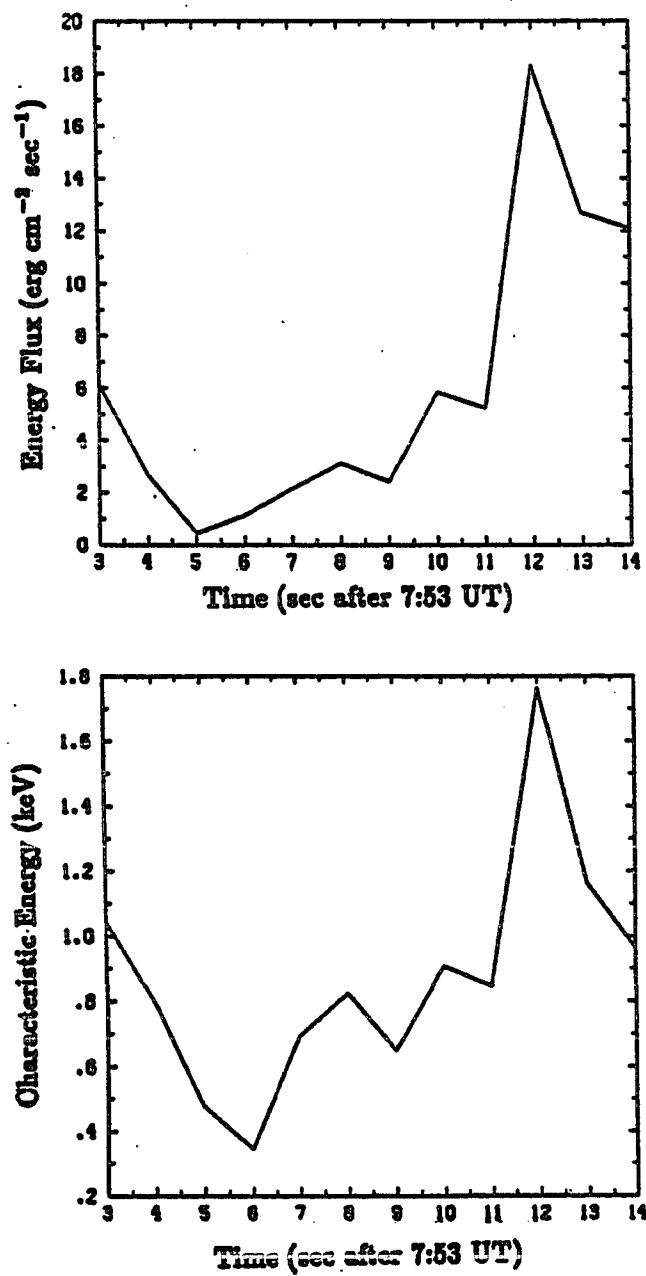
Fig. 4.9 Energy flux (upper panel) and characteristic energy (lower panel) for precipitating electrons observed by LAPI between 7:53:03 UT and 7:53:14 UT. The data that are displayed show the variation of the electron spectrum along a segment of the track of DE-B shorter than the diameter of a single pixel in the SAI image.
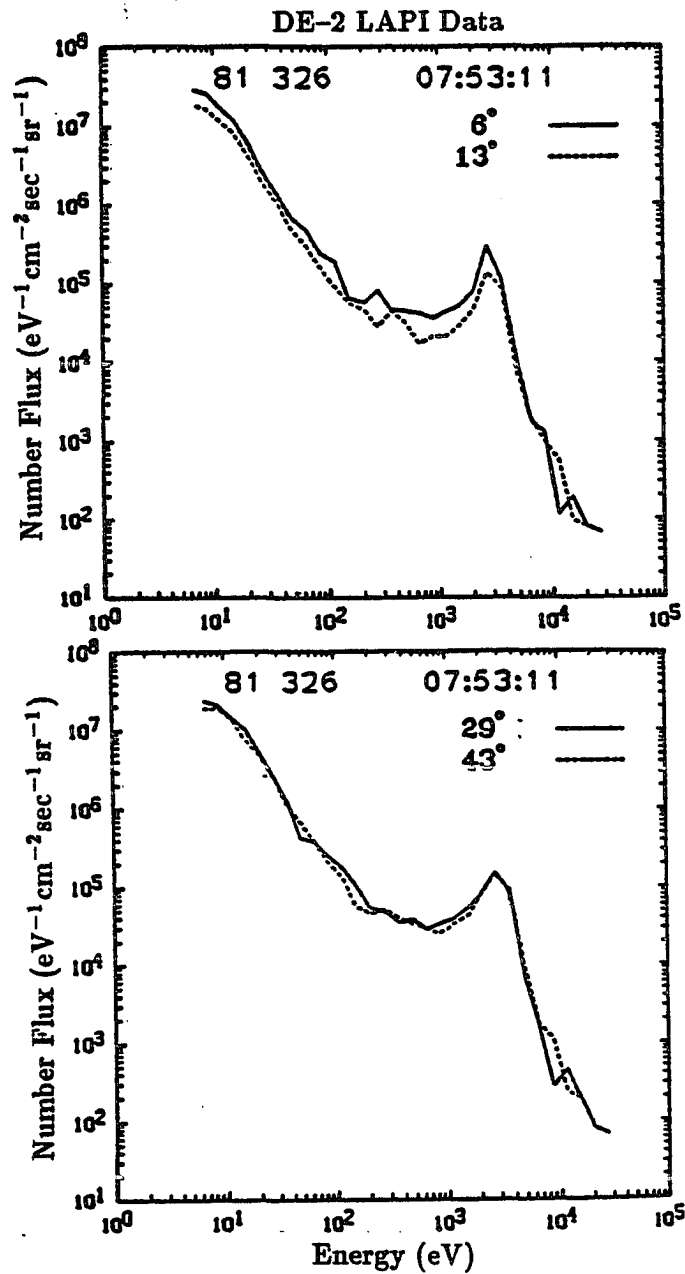
Fig. 4.10 Observed intensity of the precipitating electrons at 7:53:11 UT from 4 selected LAPI sensors.

to the UV image, because only the pixels in the center of the image fulfill the criterion of simultaneity.

To interpret the OI 5577 Å line in terms of energy flux, the assumption is made that the ratio between the N_2^+ 1N band at 4278 Å and the OI 5577 Å line is a constant. This assumption probably holds within a factor of two. It follows then, that the OI 5577 Å brightness can be directly related to the energy flux of the precipitating electrons. The LAPI electron spectrum at 7:53:11 UT gives an energy flux of 5.8 erg cm^{-2} sec^{-1} and the corresponding photometer count rate of the 5577 Å emission gives 12 counts. Unlike the UV emissions, part of the surface brightness in the visible wavelength region includes backscattering from the underlying atmosphere and reflection from the ground. To take the albedo into account, the count rate of the 5577 Å photometer has to be corrected. An estimated backscatter enhancement of 50% (Stamnes and Witt, 1987) reduces the effective count rate to 8 counts. Using the energy flux from the LAPI electron spectrum to calibrate the count rate of the 5577 Å image in terms of energy flux, yields the conversion factor of 0.725 (erg cm^{-2} sec^{-1})/counts. The I_{5577}/I_{4278} ratio that is implied in this conversion factor can be retrieved by using the calibration of the 5577 Å photometer. The albedo corrected 8 counts refer to a brightness of OI 5577 Å of 3.3 kR. The brightness of the N_2^+ 1N band at 4278 Å is calculated from the LAPI electron spectrum to be $I_{4278} = 1.28$ kR. The resulting ratio, $I_{5577}/I_{4278} = 2.6$, is small, but within the range inferred from other observations (Gattinger and Vallance Jones, 1972).

The energy flux of the precipitating auroral electrons can now be calculated for the entire auroral oval. Fig. 4.11 shows contour lines of constant energy flux, projected onto a geomagnetic coordinate grid. Integrating this energy flux over the area of the auroral oval yields a total energy input onto the ionosphere of 110 GW. Using the relation between the characteristic energy and the count rate of the UV-photometer (Fig. 4.5), the ratio of the counts in the UV-image to the counts in the 5577 Å image is used to infer E_{char} at

all locations in the auroral oval. The result is displayed in Fig. 4.12, which shows contour lines of constant E_{char}.

With these two parameters, total energy flux and characteristic energy, the electron precipitation is characterized for the entire auroral oval. In a study that compared the conductances which were derived from ratios of height integrated optical emissions to conductances which were derived from radar observations, Mende *et al.* (1984) concluded that spectroscopic data may be used to infer the Hall and Pedersen conductances. Mende *et al.* (1984) base their comparison on the ratio of I_{6300}/I_{4278} and the absolute brightness of I_{4278}. Since the I_{6300}/I_{4278} ratio is related to the characteristic energy (Rees and Roble, 1986), and the brightness of I_{4278} is proportional to the total energy flux, any pair of emissions that yields these two parameters may be used to infer the conductances. Combining Mende *et al.'s* relation with the results of Rees and Roble, a relation that expresses the conductance as a function of E_{char} and the energy flux is found (see also Robinson *et al.*, 1987). Fig. 4.13 displays the Hall conductance Σ_H and the Pedersen conductance Σ_P, normalized to the square root of the energy flux F_E^-, as a function of E_{char}. This relation can now be applied to the image of the auroral oval. Using the energy flux and the characteristic energy from Fig. 4.11 and Fig. 4.12, the conductances are calculated. Fig. 4.14 shows contour lines of constant Hall conductance on geomagnetic coordinates, and Fig. 4.15 shows the Pedersen conductances.

Models of the high latitude ionospheric convection pattern (Volland, 1978; Heelis *et al.*, 1982) depend on knowledge of the global distribution of the conductances on the scale of the auroral oval as one of their input parameters. The ability to determine the conductances from satellite images offers a valuable improvement to these models. Quantitative results derived from auroral satellite images may also lead to an improved parameterization of the auroral energy input to global models of the thermosphere and ionosphere.
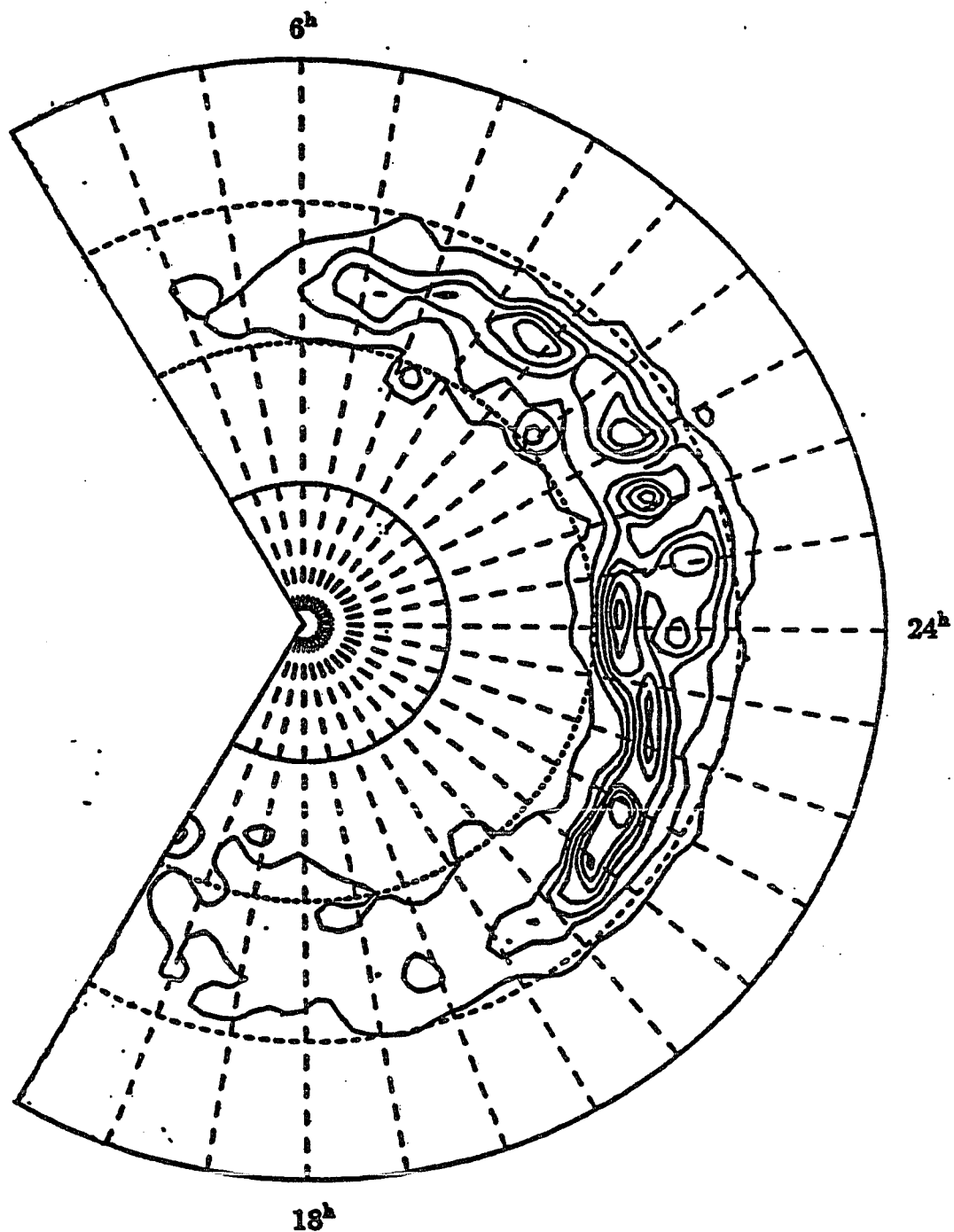
Fig. 4.11 Contour lines of constant energy flux into the atmosphere in increments of 5 erg cm^{-2} sec^{-1}, projected onto geomagnetic coordinates. The section of the sunlit atmosphere is blanked out. The lowest energy contour refers to 3.5 erg cm^{-2} sec^{-1}.
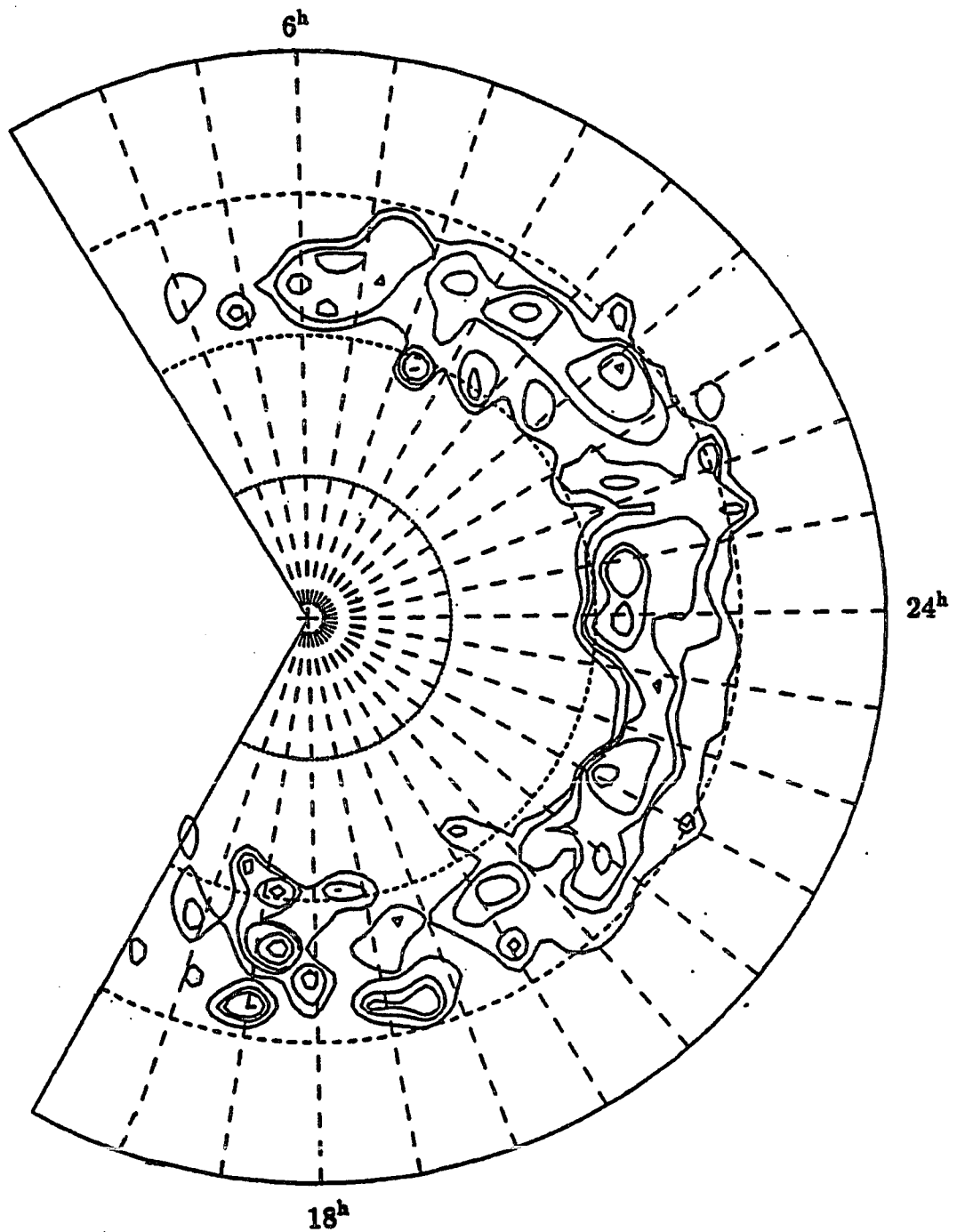
Fig. 4.12 Contours of constant characteristic energy at the levels 0.5, 1, 1.5, 2, 3, and 6 keV. The characteristic energy is derived from the count ratio of two simultaneous SAI images.
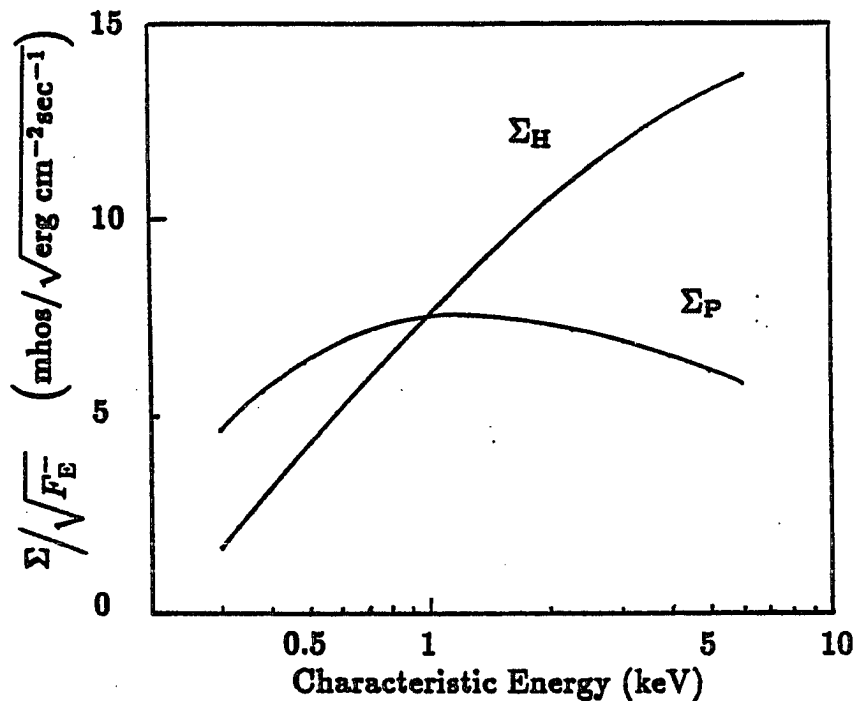
Fig. 4.13 Normalized conductances as a function of the characteristic energy.

4.4 Application of the Electron Transport Results to Ground Based Optical Observations

The first step in the interpretation of auroral optical emissions is the characterization of the incident electron spectrum. It has been shown in section 4.2 that for most purposes two parameters, E_{char} and downward energy flux F_E^-, suffice for this characterization. The model calculations show that the column emission rates of the spectral features that are included in this work (see Table 3) are almost independent of the shape of the incident electron spectrum. Furthermore, ratios between column emission rates that result directly from electron impact on a single species are independent of the model atmosphere. The incident electron spectrum (i.e. E_{char} and F_E^-) can therefore be inferred from these emissions without detailed knowledge of the atmospheric composition. Column emission rate ratios resulting from different neutral species may be used to infer density ratios between
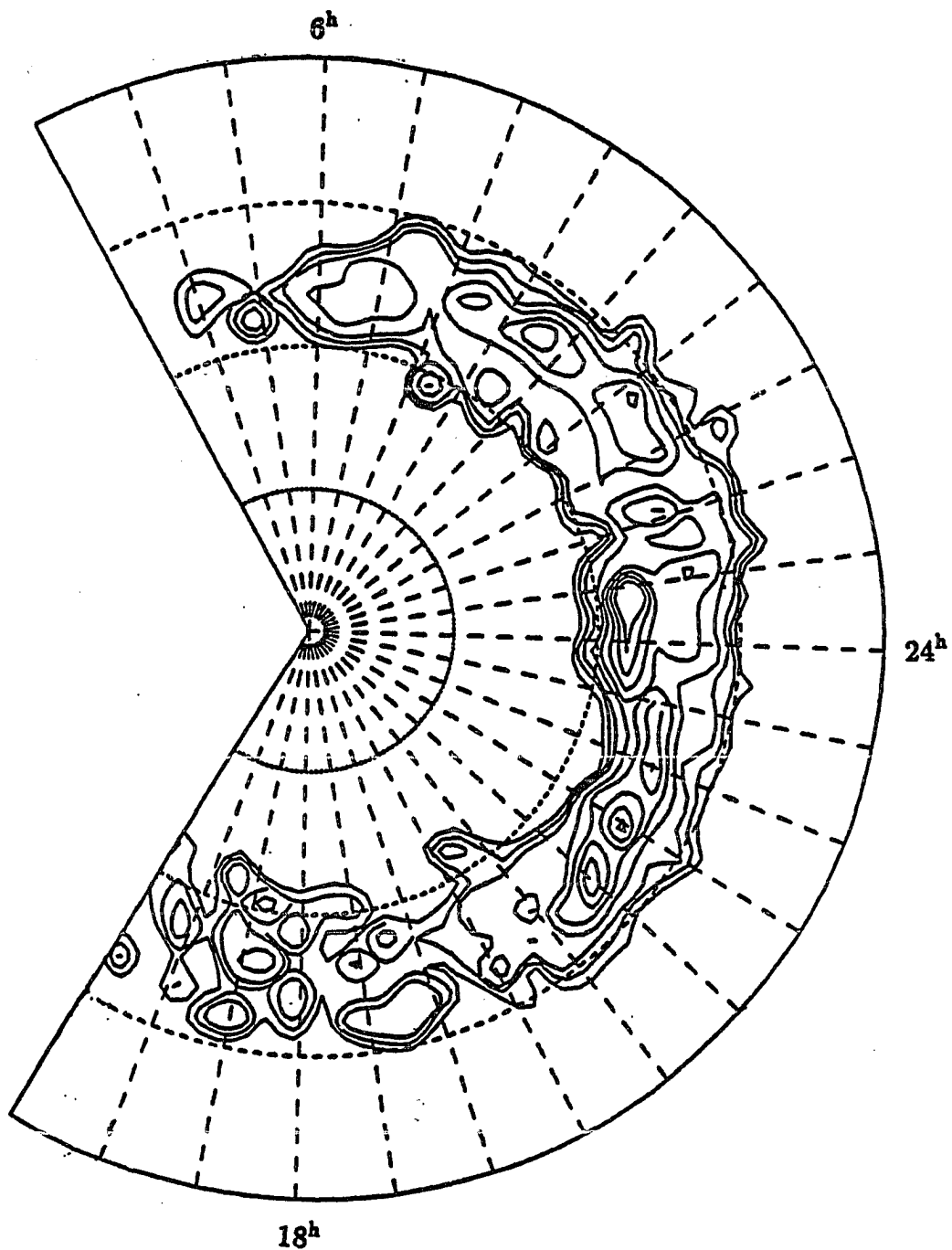
Fig. 4.14   Contours of the Hall conductance at the levels 5, 10, 15 mhos, and then increasing in increments of 10 mhos. The section of the sunlit atmosphere is blanked out.
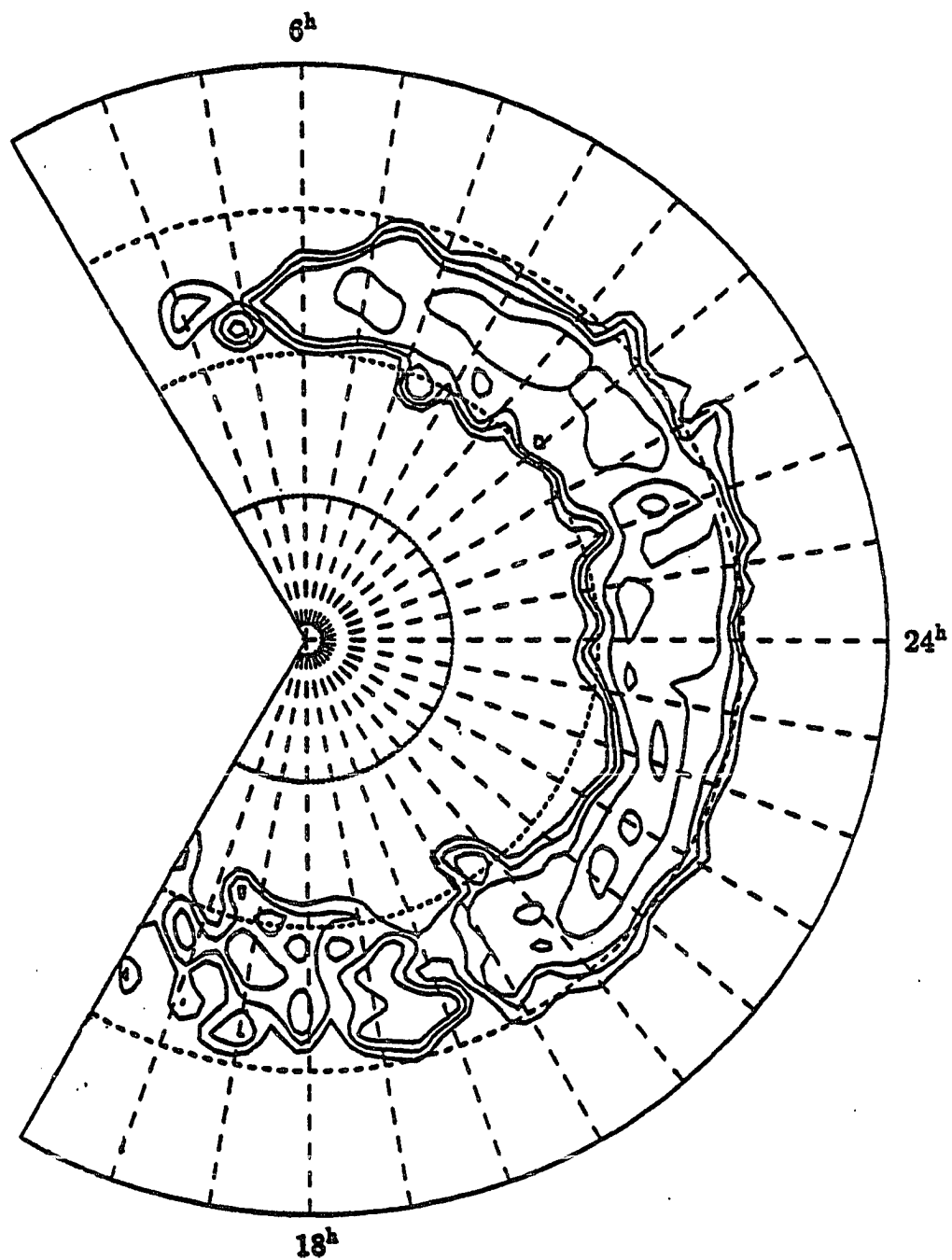
Fig. 4.15   Same as Fig. 4.14 for the Pedersen conductance.

neutral species, provided E_{char} is known. The criteria for selecting emission features for analysis with the electron transport model are: 1) the emissions must result directly from electron impact excitation and the emission cross section must be known from laboratory measurements or theory; 2) the ratio of emission features of the same species must exhibit a variation with E_{char}; 3) extinction and scattering of the radiation through the atmosphere and instrumental constraints must be considered. The last criterion excludes all UV emissions from ground based observations.

Two auroral features that are easily observed because of their outstanding brightness are the N_2^+ 1N(0,1) band at 4278 Å and the OI(6300 Å) line and these are often used to infer the energy flux and the characteristic energy. It has been shown in section 4.2 that the column emission rate of the N_2^+ 1N band is a good indicator of the energy flux. Experimental results indicate that the ratio of I_{6300}/I_{4278} ('red/blue ratio') is a function of E_{char}, but modelling of the OI(6300 Å) brightness is complex and criterion 1) fails. The OI(6300 Å) emission results from the transition of $O(^1D)$ to the ground state. This state is excited through direct electron impact as well as chemical reactions and dissociative recombination of O_2^+. Rees and Roble (1986) list seven processes that contribute to the excitation. The radiative lifetime of the $O(^1D)$ state is approximately 110 sec and the loss rate is dominated by the much faster collisional deactivation. The brightness of the OI(6300 Å) varies inversely with E_{char} for a given energy flux. Many authors use the 'red/blue' ratio to characterize the incident electron spectrum (e.g. Eather and Mende, 1972; Christensen et al., 1987), and Rees and Roble (1986) present an approximate equation for the OI(6300 Å) brightness as a function of E_{char}. The current transport code does not include chemical processes and is inadequate to calculate the OI(6300 Å) volume emission rate which is not included in the interpretation of optical observations.

During the fall and winter 1986/87 a 1m Fastie-Ebert spectrometer was operated at Poker Flat to test the method outlined above for obtaining F_E^-, E_{char}, and neutral composition from selected auroral spectroscopic emissions. This instrument acquires spectra by tilting a diffraction grating and thus scanning a given wavelength range. The length of this range is inversely related to the spectral resolution and, at a constant scan rate, the sensitivity. Auroral observations demand a high time resolution because of the variability of the aurora. The instrumental constraints for the selection of emission features therefore require spectral proximity to achieve sufficient resolution for spectral separation and to increase the sensitivity. The field of view of the spectrometer is $\approx 7°$. The spectrometer was pointed in the magnetic zenith in order to align the line of sight with the auroral field aligned structure. The observed surface brightness of an auroral emission for which the atmosphere is optically thin can then be related directly to the column emission rate. In order to minimize atmospheric extinction the spectral features for the analysis were chosen in the visible wavelength range.

An oxygen ion emission with a laboratory measured emission cross section is the OII(5) multiplet with its two brightest lines at $\lambda = 4414.9$ Å and $\lambda = 4417.0$ Å. The emission cross section of the OII(4416 Å) line group consisting of these two lines was measured by Haasz and DeLeeuw (1976). They concluded that the contribution from O_2 dissociation is small compared to direct ionization excitation of atomic oxygen. Two N_2 emissions in the spectral vicinity of OII(4416 Å) are the N_2^+ 1N(0,1) band at 4278 Å and the N_2 2P(0,4) band at 4344 Å, which have already been discussed in section 4.2. Their ratio as a function of E_{char} is shown in Fig. 4.3.

A second set of auroral emissions, consisting of an N_2 and O_2 first negative band and an atomic nitrogen emission, required an independent setup of the spectrometer and could not be observed simultaneously with the first wavelength range.

The two wavelength ranges chosen for this study are: the range from 4260 Å to 4440 Å at a resolution of 4 Å, and the range from 4820 Å to 5620 Å at a resolution of 8 Å. The auroral spectrum in these wavelength ranges is illustrated by two sample spectra in Fig. 4.16. The brightest features are identified in the figure. The range 4260 Å to 4440 Å includes the N_2^+ 1N(0,1) band at 4278 Å, which is so bright that the count rate is off scale in Fig. 4.16 (top panel). The lines of the OII(2) multiplet at the wavelengths 4317 Å, 4320 Å, 4337 Å, 4346 Å, and 4349 Å partially overlap with the N_2 2P(0,4) band at 4344 Å. Also in this wavelength range are the OI(5) line at 4368 Å, the OII(5) multiplet at 4416 Å, and the NII(55) multiplet at 4433 Å. The emission cross sections for the N_2^+ 1N band (4278 Å), the N_2 2P band (4344 Å), and the OII(4416 Å) multiplet have been measured and the volume emission rate of these features can be calculated from the electron intensity. Their column emission rates are displayed in Fig. 4.1 as a function of E_{char}. Both the $N_2$2P (0,4) and the OII(4416 Å) brightnesses are small, so that only bright auroral events can be interpreted. The mercury line, which is also identified in the spectrum, results from scattered city lights and serves as an indicator of clouds.

During the second half of the night of November 4, 1986, bright auroral activity was observed with the 1m Fastie-Ebert spectrometer scanning the range 4260 Å to 4440 Å. The brightness of the N_2^+1N (0,1) band reached 4 kR, while the brightness of the $N_2$2P (0,4) band and the OII(4416 Å) exceeded 70 R and 40 R respectively. Since the $N_2$2P band overlaps with the OII(2) lines (see Fig. 4.16) and the resolution of the spectrometer was insufficient to separate the $N_2$2P band from the OII lines, uncertainties are introduced in the measurement of the brightness of the $N_2$2P. The emission cross section for the OII(4416 Å) line group has an uncertainty of 40% (Haasz and DeLeeuw, 1976) which exceeds by far the uncertainty due to counting statistics of the photomultiplier. These errors are, however, systematic errors which affect the absolute value of the brightness, while relative changes
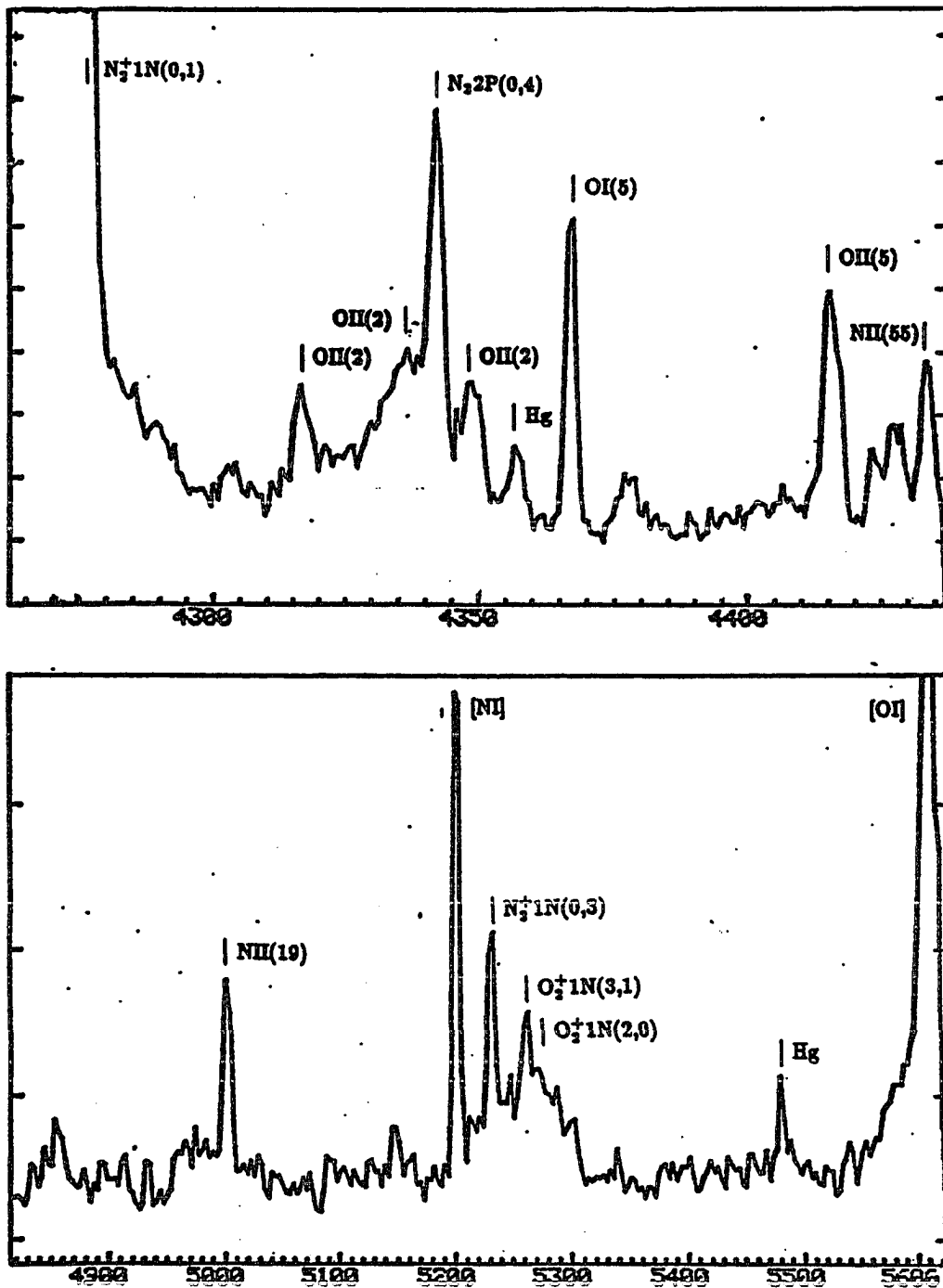
Fig. 4.16 Auroral spectrum in the wavelength range 4260 Å to 4440 Å (top) and 4820 Å to 5620 Å (bottom). The brightest features are identified. The N_2^+1N(0,1) band at 4278 Å and the OI(5577 Å) green line are off scale in this representation. The emissions that are suitable for an interpretation in the framework of the electron transport calculation are the N_2^+1N and O_2^+1N bands, the $N_2$2P band, the OII(4416 Å) line group and the NII(5001 Å) line group.
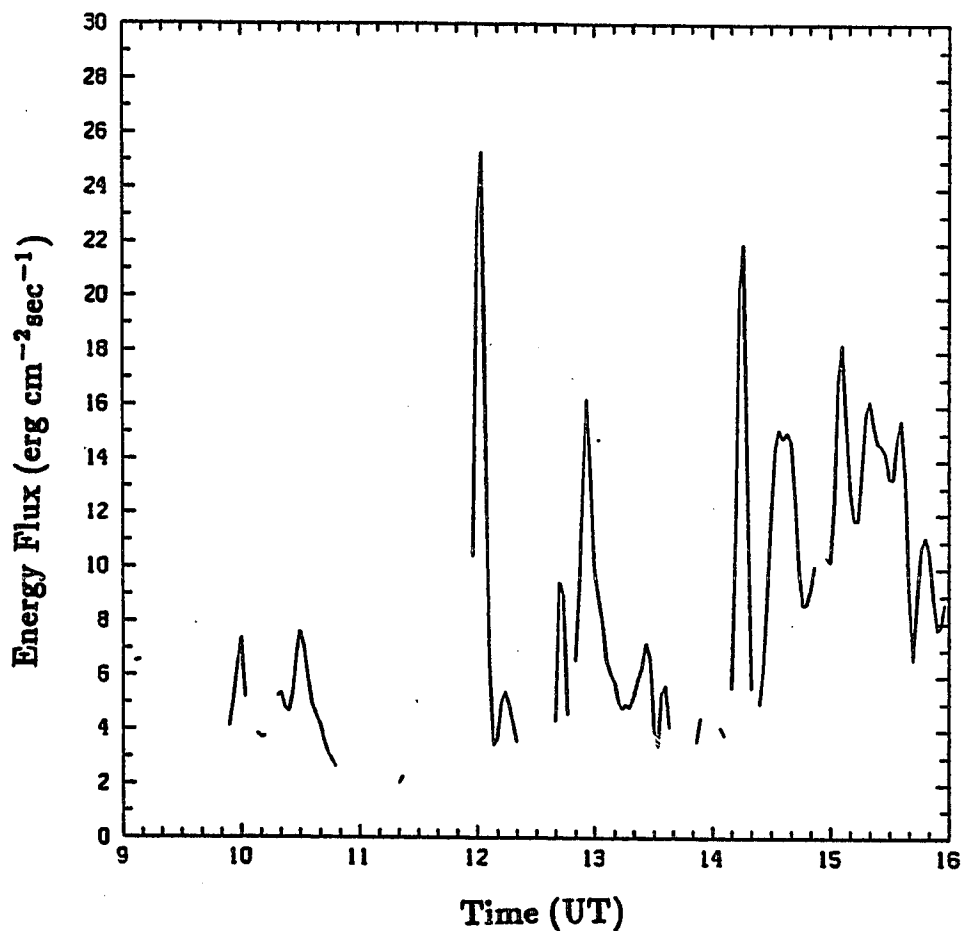
Fig. 4.17 Energy flux as a function of time for November 4, 1986, 9:00 UT to 16:00 UT. The energy flux is derived from the $N_2^+ 1N$ (0,1) brightness. Local solar midnight is at 9:52 UT.

during the observation period may be of greater significance, assuming that the background level is consistently taken into account.

Fig. 4.17 shows the energy flux of the precipitating electrons as a function of time for November 4, 1986, 9:00–16:00 UT. The energy flux is derived from the $N_2^+ 1N$ (0,1) brightness by means of the conversion factor of 250 $R/(\text{erg cm}^{-2}\text{sec}^{-1})$. A time resolution of 2 minutes was achieved. Data of the MSP (meridian scanning photometer) in Poker Flat are available for the same period. The MSP consists of 5 photometers with a narrow field of view (1°) equipped with interference filters. It scans along the magnetic meridian and assembles the time evolution of auroral activity in the meridional plane. The MSP data

are used to describe the general development of the aurora and to discriminate electron from proton precipitation by monitoring the H_β brightness. The MSP data show that the two features that are observed at 10:00 UT and 10:30 UT (Fig. 4.17) are associated with southward moving broad auroral structures which passed through the field of view of the spectrometer, while the activity at 12:00 UT and 13:00 UT occurred simultaneously over a large latitudinal extent north and south of the field of view. After 14:00 UT the main emission region was located north of the field of view, and the H_β channel of the MSP indicated an increasing amount of proton precipitation in the magnetic zenith.

The ratio of N_2^+1N (0,1) to $N_2$2P (0,4) (I_{4278}/I_{4344}) varied between 40 and 90 during the night. As discussed earlier, this ratio as a function of E_{char} is independent of the model atmosphere and is well suited to infer E_{char}. According to Fig. 4.3 the observed ratios refer to characteristic energies of the electron precipitation between 0.5 keV and 3 keV.

The OII(4416 Å) emission arises from $O + e$ collisions, and the OII(4416 Å) brightness is a function of the O-density and of E_{char}. Fig. 4.18 shows the ratio I_{4278}/I_{4416} as a function of E_{char} for several O-density scalings of the MSIS-83 atmosphere. Knowing the characteristic energy and the energy flux, the ratio I_{4278}/I_{4416} is interpreted in terms of the O-density scaling factor.

For the auroral features at 10:30 UT and 12:00 UT the ratios I_{4278}/I_{4416} yield the same E_{char} as the ratios I_{4278}/I_{4344}, if the O-density is scaled by 0.75, while the ratios at 13:00 UT and 14:15 UT are in better agreement with an unscaled O-density. The data between 14:30 UT and 15:30 UT are not included in this comparison, because the H_β brightness indicates proton precipitation. Towards morning, when the main emission region was north of the field of view, a smaller scaling factor is again required. The ratios I_{4278}/I_{4416} and I_{4278}/I_{4344} and their interpretation in terms of E_{char} and O-density scaling are summarized in Table 4.
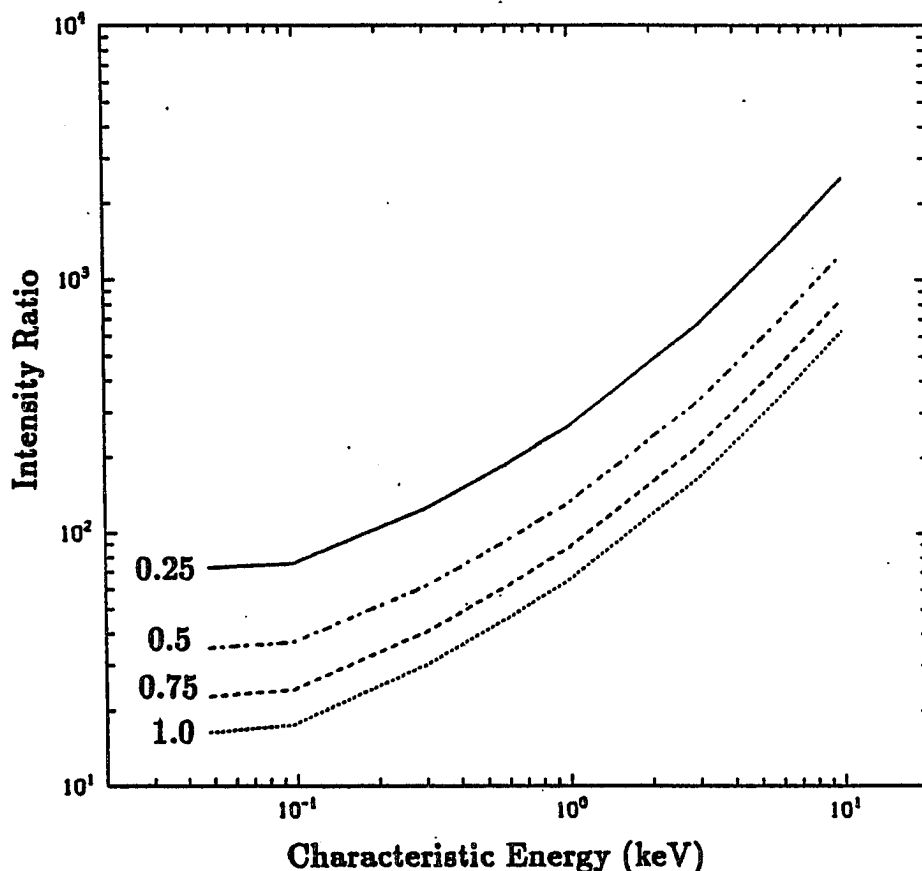
Fig. 4.18 Ratio of the column emission rates of N_2^+1N (0,1) to $OII(4416\ \text{Å})$ as a function of E_{char}. The four graphs refer to different scaling of the MSIS-83 O-density.

Because of the uncertainties discussed above the absolute values of E_{char} and the O-density scaling factor may have large errors (40%), but the relative variation through the night is significant. To improve the determination of E_{char} from the N_2^+1N to N_22P ratio, a brighter and more isolated band of the N_22P system should be selected. The N_22P (0,0) band at 3371 Å is comparable in brightness to the N_2^+1N (0,1) band and less polluted by other overlapping emissions. It is, however, so far in the blue wavelength range, that atmospheric extinction drastically reduces the signal level, unless observations are made from high flying aircraft or from satellite. The N_22P (0,2) band at 3804 Å or the N_22P (1,4) at 3997 Å are preferable bands. They were not used in this analysis, because of the large

Table 4

Brightness Ratios and Their Interpretation During November 4, 1986

Time (UT)	I_{4278}/I_{4344}	E_{char} (keV)	I_{4278}/I_{4416}	O-density scaling
10:24	52	1.0	85	0.75
10:44	61	1.5	120	0.75
12:02	63	1.5	120	0.75
13:00	78	2.2	110	1.1
13:02	88	2.7	130	1.0
14:12	70	1.8	87	1.1
14:14	77	2.2	110	1.1
14:18	73	2.0	85	1.2
15:26	84	2.5	165	0.9
15:30	68	1.7	155	0.75
15:34	75	2.0	160	0.75

wavelength separation from the OII(4416 Å) line group. To improve the interpretation of the OII(4416 Å) line group, a more accurate laboratory measurement of the emission cross section is needed.

The second wavelength range (4820 Å to 5620 Å) includes the NII(19) multiplet at 5001 Å, the forbidden NI doublet at 5200 Å, the N_2^+ 1N(0,3) band at 5228 Å, the O_2^+ 1N(3,1) and (2,0) bands at 5252 Å and 5275 Å, and the forbidden OI line at 5577 Å. The count rate of the green line (5577 Å) is off scale in Fig. 4.16 (bottom panel). The OI(5577 Å) emission results from the $O(^1S) \rightarrow O(^1D)$ transition. The excitation of the $O(^1S)$ state is governed by complex chemical reactions and the calculation of the OI(5577 Å) volume emission rate is not included in the current transport code. The volume emission rates of the first negative bands of N_2^+ and O_2^+ as well as of the NII(5001 Å) multiplet result from direct electron impact on neutrals and can be calculated from the electron intensity.
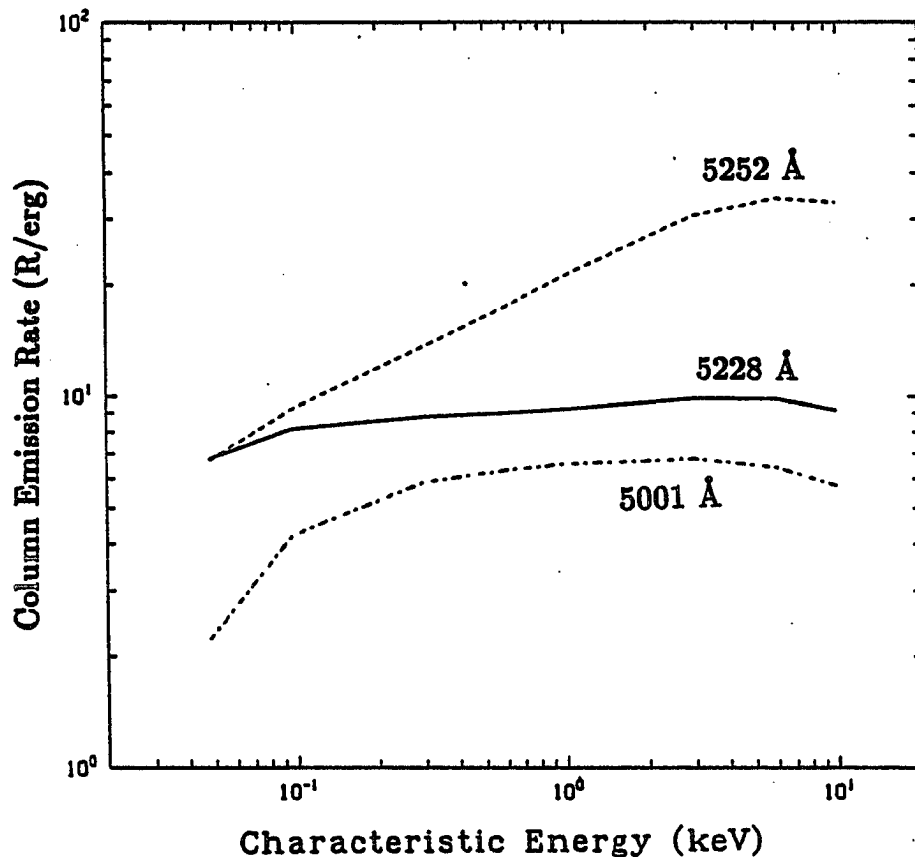
Fig. 4.19 Column emission rates of the $O_2^+ 1N(3,1)$ and $(2,0)$ bands at 5252 Å, the $N_2^+ 1N(0,3)$ band at 5228 Å, and the NII multiplet at 5001 Å as a function of E_{char}. Maxwellian boundary conditions with an electron energy flux of $F_E^- = 1$ erg cm^{-2}sec^{-1} were applied at 800 km altitude.

The corresponding column emission rates are shown in Fig. 4.19 as a function of E_{char}. Since the two O_2^+ 1N bands overlap considerably, the graph shows the sum of their column emission rates.

Auroral observations of this spectral range were made during March, 1987. Two emissions that originate from $N_2 + e$ are the $N_2^+ 1N$ (0,3) band at 5228 Å and the NII(19) multiplet with the two brightest lines at 5001.1 Å and 5001.5 Å. The ratio of the NII(5001 Å) to the $N_2^+ 1N$ (0,3) column emission rates (I_{5001}/I_{5228}) as a function of E_{char} is shown in Fig. 4.20 together with the ratio of the column emission rates of $N_2^+ 1N$ (0,3) to the two $O_2^+ 1N$ bands (I_{5228}/I_{5252}). The ratio (I_{5001}/I_{5228}) is almost constant for $E_{char} \geq 200$ eV
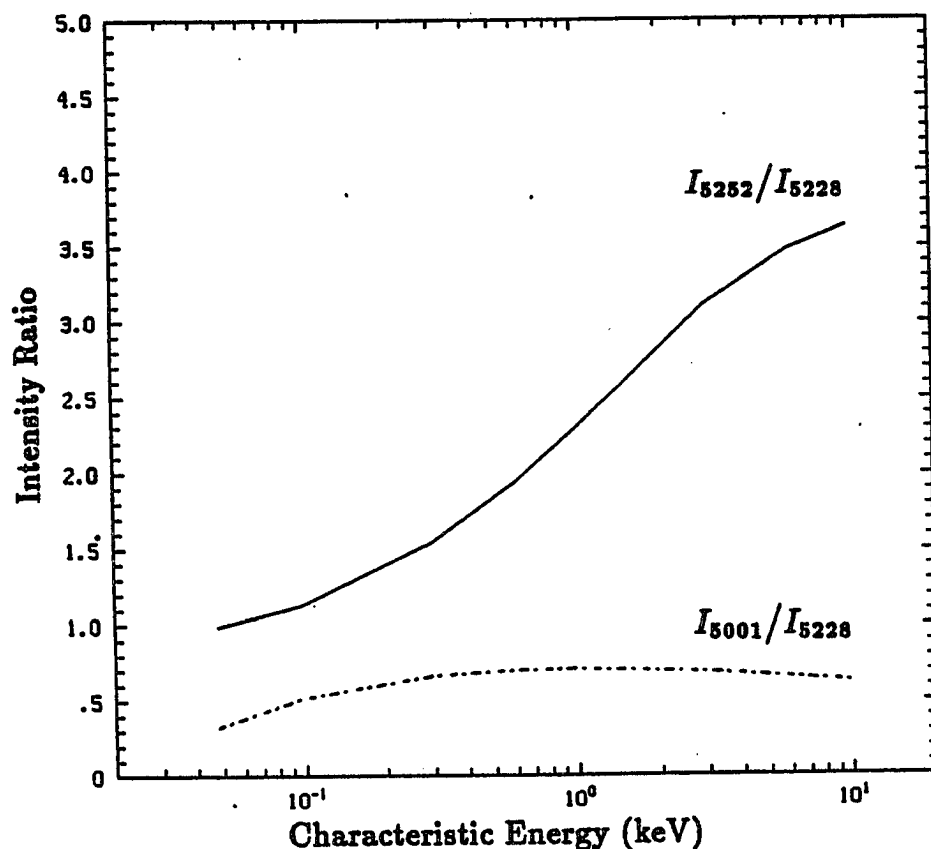
Fig. 4.20 Ratio of the column emission rates of the sum of $O_2^+ 1N$ (2,0) and (3,1) to $N_2^+ 1N$ (0,3) (solid line) and the ratio of NII(5001 Å) to $N_2^+ 1N$ (0,3) (dashed line) as a function of E_{char}.

and therefore only suited to distinguish very soft precipitation. The emission cross sections of the NII(5001 Å) and the $N_2^+ 1N$ band have a similar energy dependence except for the high threshold of the NII(5001 Å) cross section at 53 eV.

Under the assumption that the N_2 and O_2 densities are correctly represented by the MSIS-83 atmosphere, the characteristic energy of the precipitating electrons can be inferred from the ratio of the column emission rates of the $N_2^+ 1N$ to the $O_2^+ 1N$ bands. Fig. 4.19 shows the column emission rates for these bands as a function of E_{char}. Since the $O_2^+ 1N$ (2,0) and (1,3) bands overlap, and since they originate from the same excited state, they are lumped together and the sum is displayed.

The brightness of the N_2^+1N (0,3) band and of the sum of the two O_2^+1N bands is measured by fitting synthetic spectra of these emissions to the observed spectrum. The calculations of the synthetic spectra were carried out with the program DIALUP (Degen, 1986). Some modifications to the DIALUP code were necessary to enable the user to change the ratio between the N_2^+1N and O_2^+1N bands. This rather cumbersome method to measure the ratio and brightness of the two bands is necessary because the bands overlap each other and are contaminated by the forbidden NI(5200 Å) doublet.

The spectrometer was not fully operational during the observation period in March 1987 and worked only for brief periods. An additional limitation is imposed by the short nights. On March 26, astronomical twilight (shadowheight 320 km) ends at 7:30 UT and begins again at 12:05 UT. The brightnesses of the N_2^+1N and O_2^+1N bands are plotted in Fig. 4.21 (top panel) as a function of time for a short interval of the night of March 23 and two short intervals of the night of March 26. The time resolution of the measurements is 5 minutes. The ratio of the bands is shown in Fig. 4.21 (bottom panel) for the same intervals. This ratio can be converted to E_{char} using the theoretical ratio (Fig. 4.20), and a scale for E_{char} is given on the right side of Fig. 4.21 (bottom panel).

The ratio of the column emission rates of NII(5001 Å) to the N_2^+1N band is expected to be nearly constant for $E_{char} \gtrsim 0.2$ keV (see Fig. 4.20) at a value of $I_{5001}/I_{5228} \approx 0.65$. The average value of this ratio from 12:20 UT to 13:05 UT on March 23, when the characteristic energy stayed above 0.5 keV (Fig. 4.21) gives $I_{5001}/I_{5228} = 0.48$ with a standard deviation of 0.08. The two intervals on March 26, excluding the measurements at 8:35 UT and 11:15 UT, when E_{char} dropped to 0.1 keV, yield a ratio of $I_{5001}/I_{5228} = 0.51 \pm 0.08$. At the two incidences of $E_{char} = 0.1$ keV, the ratio yields $I_{5001}/I_{5228} = 0.33$. These observed ratios are systematically smaller than the theoretical value of 0.65 but they exhibit the expected variation with E_{char}. The systematic discrepancy cannot be explained with changes in the relative density of the species of the atmosphere model since both emissions
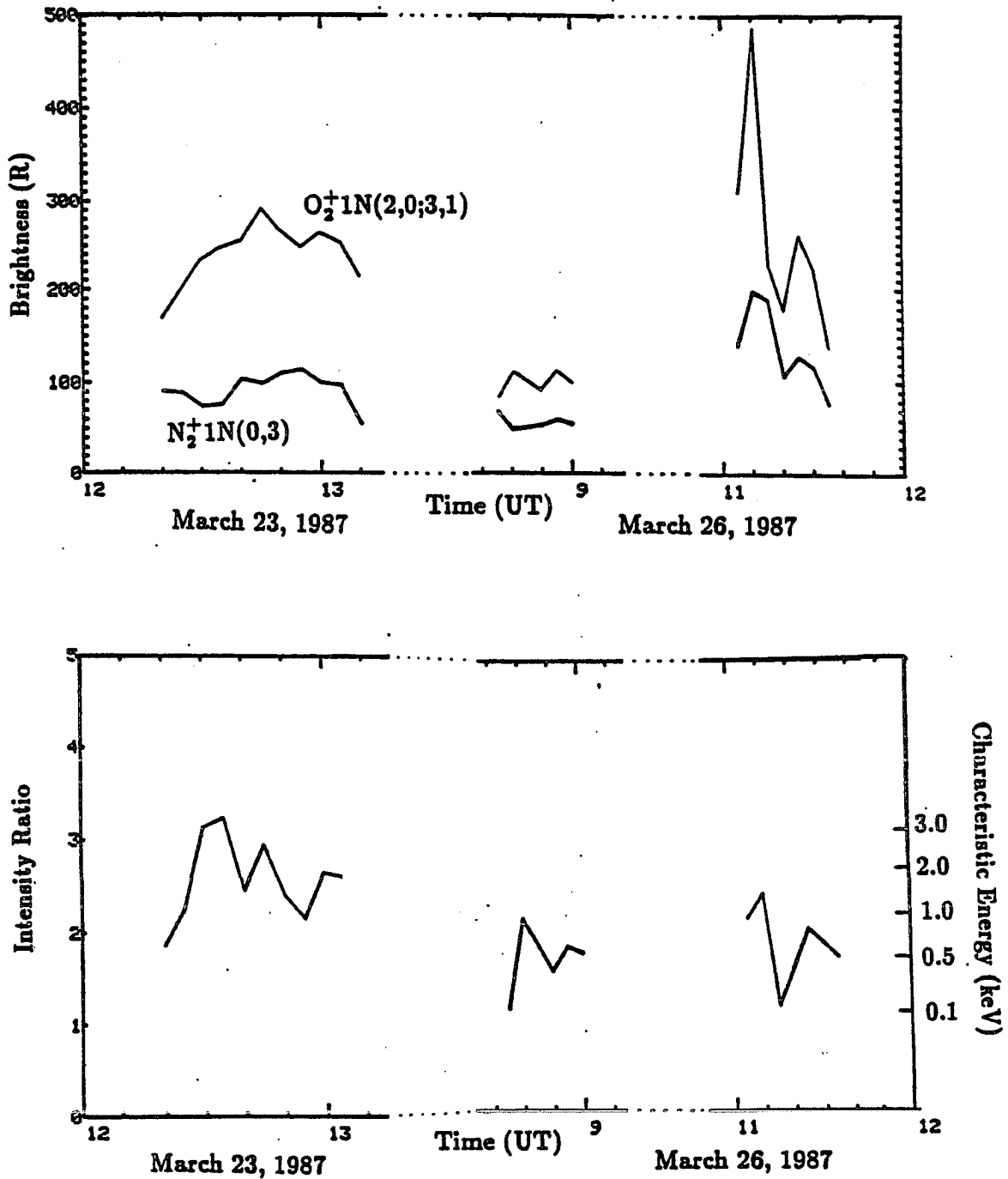
Fig. 4.21 Brightness of the N_2^+1N (0,3) and O_2^+1N (2,0) and (3,1) band during 12:20 UT to 13:10 UT on March 23 and 8:35 UT to 9:00 UT and 11:00 UT to 11:35 UT on March 26 (top panel). Local solar midnight is at 9:52 UT. The ratio of the two bands is displayed on the bottom panel. A scale for the conversion of this ratio to E_{char} is given on the right side.

result from the same species, i.e. from $N_2 + e$ collisions. Filippelli *et al.*, (1982) measured the emission cross section for the entire multiplet NII(19), while only the two brightest lines are taken into account for the data analysis. This leads to an underestimate of the NII(19) multiplet emission which may explain the low observed value for the ratio I_{5001}/I_{5228}. The uncertainty in the measurement of the emission cross section of Filippelli *et al.* is 15% and a similar error in the ratio may have been introduced by the measurement of the absolute brightness of the $N_2^+ 1N$ band. The measurement and the theoretical value of the ratio I_{5001}/I_{5228} are therefore in agreement within the error limits.

Chapter 5. Summary and Conclusions

The objective of this thesis is the development of a model for interpreting optical auroral observations in terms of ionospheric properties. The primary local energy source for the aurora is the electron precipitation. An electron transport calculation is carried out, which yields the electron intensity as a function of altitude, energy, and pitch angle for a given incident electron spectrum. The transport equation is derived from the Boltzmann equation. Cross sections for angular scattering and energy degradation of electrons are necessary input to the transport calculation, and cross sections for the emission of a photon upon electron impact are needed for the calculation of the brightness of auroral features. A set of cross sections is compiled and discussed in Sections 2.2 and 4.1. The cross sections are summarized in Tables 1, 2, and 3 with their references.

The numerical solution of the transport equation is discussed in Chapter 3. A differential equation for a two-stream approximation is derived and solved. Recognizing the formal similarity between electron transport and radiative transfer, the discrete ordinate method developed by Stamnes and co-workers (1987) is adopted as a numerical scheme for the multi-stream approximation. This method proves to have smaller numerical errors compared to the differential equation solver of the two-stream approximation. Electron intensity measurements from a sounding rocket (Pulliam *et al.*, 1981) were used in a comparison with the results of the multi-stream calculation. The overall agreement between observed backscattered electrons and computed intensities inspires confidence in the implementation of the transport code. Differences between the experimental data and the model predictions point to possible improvements that may be achieved by including effects of the converging geomagnetic field (Stamnes, 1985b).

The electron intensities are used to calculate volume production rates of excited states and ionization rates of the constituents of the upper atmosphere. Optical emissions result from radiative de-excitation. The calculation of the emission rates includes cascading and branching but is limited to electron impact excitation only. The resulting emissions are directly linked to the electron intensity. Excitation due to chemical reactions depends not only on the initial electron impact on one species but on a complicated non-linear interaction between many different reaction partners. For some prominent auroral emissions, OI(6300 Å) and OI(5577 Å), the relative importance of these processes is still under investigation. The interpretation of auroral emission features is therefore limited to emissions that result from direct electron impact on molecular and atomic constituents of the atmosphere. Excited states for which chemical reactions are an unlikely excitation mechanism are those with a high excitation threshold. Excited ion states and dissociative excitation are preferred candidates. Uncertainties in individual excitation cross sections have only a small impact on the results of the transport calculation, which depend on the total cross section. The excitation rate of the individual states and the brightness of emission features, however, are directly affected by uncertainties in the cross sections and model atmosphere. Reliable laboratory measurements are therefore crucial for the interpretation of optical emissions.

In order to relate a volume emission rate to surface brightness, the radiative transfer of the emission to the observer and the geometry of the emission volume must be considered. Because of the structure of the aurora it is advantageous to align the viewing direction of an instrument with the geomagnetic field. The observed surface brightness is then related to the column emission rate. For an optically thin case ($\tau \ll 1$), which applies to part of the visible wavelength range, extinction in the atmosphere can be neglected. In the optically thick case ($\tau \approx 1$), especially at visible blue and UV wavelengths, scattering and absorption has to be taken into account. For some emission lines, e.g. OI(1304 Å) and

NI(1200 Å), the atmosphere is extremely thick ($\tau \gg 1$) due to resonant absorption, and resonant scattering of the radiation transfer must be included in the calculation of the surface brightness.

The systematic dependence of the surface brightness of auroral emissions on the characteristics of the incident electron spectrum and the atmospheric composition opens the possibility for inferring the energy flux, characteristic energy and the atmospheric composition from optical observations. The surface brightness of the N_2^+ 1N bands is proportional to the energy flux. The N_2 2P, N_2 LBH, O_2^+ 1N, some NI, and the OI and OII surface brightnesses are also dependent on the characteristic energy. Ratios of these emissions to the N_2^+ 1N band can therefore be used to infer the characteristic energy of the precipitation. Having determined both the energy flux and the characteristic energy, the atomic oxygen emissions provide a measure for the relative O abundance at the altitude of the emission. This interpretation of auroral emissions is valid only in the framework of the model. Although it could be shown that the detailed shape of the spectrum of the incident electrons plays a minor role, the analysis can only be applied to aurora which results from "well behaved" electron spectra. Energy distributions with a large number of low energy electrons in addition to an energetic component (Robinson et al., 1987), or double-hump spectra, need direct measurements of the electron spectrum, in addition to optical observations, to be suitable for interpretation. All model calculations of the optical emissions are carried out using isotropic incident electron distributions. Application to non-isotropic distributions of the relations between brightnesses and energy flux or characteristic energy also leads to misinterpretation.

If the optical observations are carried out with low spectroscopic resolution, so that the individual lines and bands from different species cannot be separated, an assumption about the composition at the emitting altitude must be made. Combining a UV-image like the DE images with an image in the N_2^+ 1N(3914 Å) wavelength still yields sufficient information

to infer the characteristics of the electron precipitation. The electron transport calculation can then be used to determine the corresponding ionization rate, energy deposition rate, and ambient electron heating rate. It is thus possible to infer ionospheric parameters on a global scale.

The aurora changes rapidly in space and time. Sudden brightening or dimming and fast motion of small scale auroral features accompany almost any auroral display, and constitute a major element of the aesthetic value of the aurora. For the interpretation of optical observations with the proposed method, the nature of the aurora requires high time resolution and simultaneity of the measurements for the purpose of using the ratio of spectral features. Spectra that require integration over 5 minutes or the DE-photometer images that are scanned in 12 minutes therefore represent crude averages. Imaging an ionospheric region with a diameter of approximately 100 km onto a single pixel contains, in addition to the averaging over space, the uncertainty that for many auroral structures the field of view of the instrument is not filled. In that case the count rate cannot be related to the brightness of the auroral structure. The currently available satellite images and their interpretation present only one aspect of the aurora: an average global distribution. Ground based observations with high time and spatial resolution are a necessary tool to study the small scale aurora. But even with the most sophisticated instruments and analysis to interpret the aurora and to understand its causes and nature, one cannot come close to describing what the human observer sees, standing outside in the night, staring fascinated at the flames in the sky.

Appendix 1: The Energy Redistribution Function

One major task for the solution of the transport equation is the calculation of the internal sources due to cascading electrons. The use of a fixed energy grid for the numerical procedure requires an optimization scheme to accommodate the discrete energy losses of the collision processes. Adequate results can always be obtained by using small enough energy cells. This, however, requires prohibitively large data storage and computer memory and lengthens the time that the code runs. A method that uses an energy grid with large and increasing cell sizes was suggested by Swartz (1985) and is adopted in this work, with some modifications. Fig. A1.1 and A1.2 is reproduced from Swartz' paper to illustrate the problem. The case with an energy cell width ΔE larger than the energy loss T of a given process is shown in Fig. A1.1a. In this example three collisions would be needed to produce an energy loss that would degrade electrons from cell E_i to the next lower cell E_{i-1}. To account for this, the cross section for such a process is adjusted in order to reduce the probability of a degradation by ΔE to one third of its original value. This is expressed for an arbitrary combination of ΔE and T by

$$\sigma^{\text{eff}}(E) = \sigma(E)\frac{T}{E - [E - T]}.$$

T refers to the actual energy loss of the process with cross section $\sigma(E)$ and the operator $[E-T]$ denotes the energy grid cell closest to $E-T$ and at least less than E. Thus $[E_i - T]$ gives E_{i-1} in Fig. A1.1a and E_k in Fig. A1.1b. The modified cross section $\sigma^{\text{eff}}(E)$ has to be used to calculate the losses from the energy cell E_i as well as for the sources at energy cell E_k.

For the case where the sink cell E_k is smaller than the source cell E_i, the cascading of all electrons from the source cell to a single sink cell produces an artificial peak at E_k with

113

$E_{i-1} < E_i - T$

ENERGY MISMATCH

T

(a)

E_{i-1}

E_i

ΔE_{i-1}

ΔE_{i-1}

$E_k \neq E_i - T$

$< E_{i-1}$

ENERGY MIS- MATCH

T

(b)

E_k

E_{i-1}

E_{i-1}
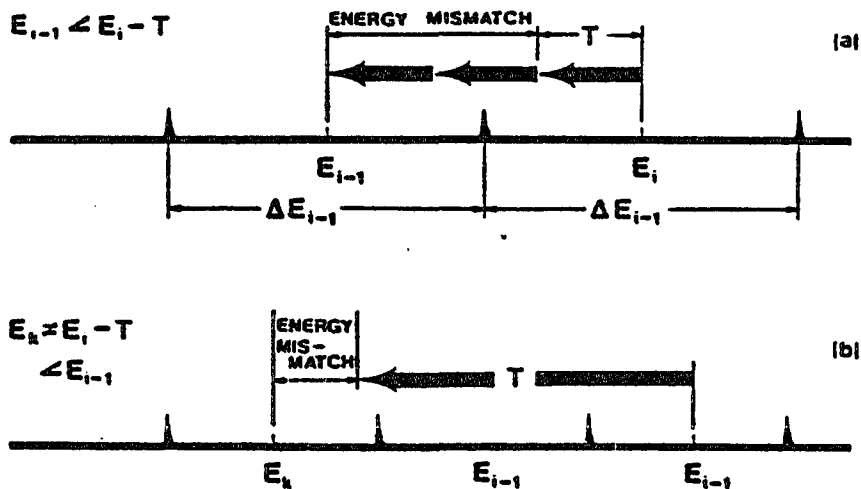
Fig. A1.1 Incompatibilities between a finite energy grid and discrete losses: (a) energy cell wider than the energy loss in one collision, (b) energy lost is not equal to the difference in mean cell energies (from Swartz, 1985).

E_i = Source Cell

E_k = Sink Cell

$\Delta E_k < \Delta E_i$

T

(a)

E_{k-1} E_k E_{k+1}

E_i

ΔE_k

ΔE_i

$\Delta E_i = \Delta E_{k-1} + \Delta E_k + \Delta E_{k+1}$

T

T

(b)

T

E_{k-1} E_k E_{k+1}

E_i

ΔE_i

ΔE_i
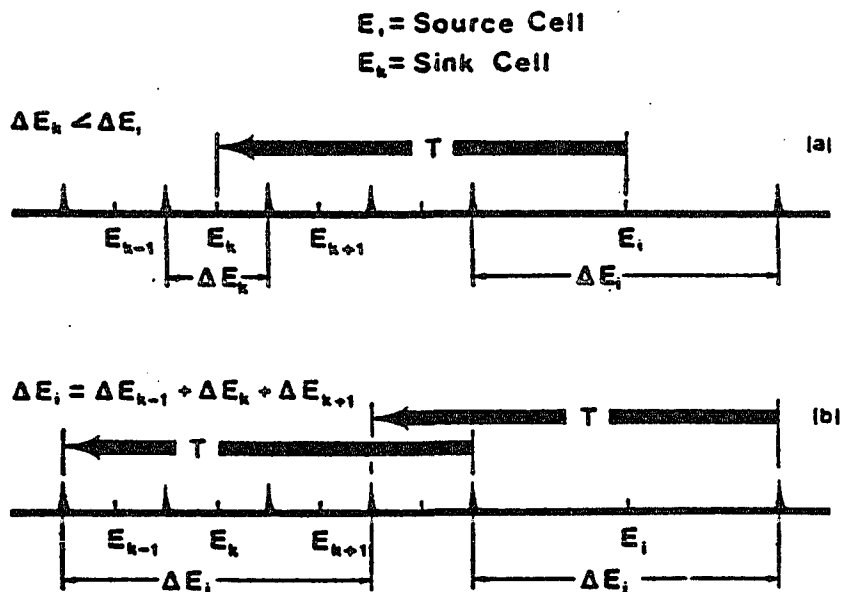
Fig. A1.2 Degradation of a large cell (a) completely into a small cell versus (b) source cell spread out over several small cells (from Swartz, 1985).

respect to the neighboring cells (Fig. A1.2a). This is avoided by distributing the degraded electrons over a number of sink cells such that the combined cell width of the sink cells equals the width of the source cell (Fig. A1.2b). This means replacing the δ-function that occurs in the production cross section

$$\sigma^{\mathrm{deg}}(E \to E') = \sigma^{\mathrm{ex}}(E')\delta(E' - (E+T))$$

by a double step function centered at $E-T$ with a width of the source cell ΔE. To minimize further mismatches that occur if the source cell width does not equal a multiple of the sink cell width, the energy grid is chosen to have cell widths proportional to increasing powers of two.

For an ionization collision the energy loss is composed of the ionization threshold, an excitation threshold if the ion is left in an excited state, and the energy transferred to the secondary electron. Thus the degradation cross section cannot be represented by a δ-function but is determined by a broader distribution. Based on the Bethe formula Rees *et al.* (1969) derived this distribution. With T the threshold, E the energy of the incident primary, and E_s the energy of the emerging secondary electron, the production cross section for secondary electrons becomes

$$\sigma^{\mathrm{sec}}(E \to E_s) = \frac{\sigma^{\mathrm{ion}}(E)}{N} \frac{1}{T+E_s} \exp\left[-\frac{T+E_s}{31.5} - 339\exp\left(-\frac{T+E_s}{2.49}\right)\right]$$
$$\ln\left(\frac{\sqrt{E}+\sqrt{E-(T+E)}}{\sqrt{E}-\sqrt{E-(T+E)}}\right).$$

$$\text{(A1.1)}$$

N is a normalization factor which is chosen such that

$$\int \sigma^{\mathrm{sec}}(E \to E_s)\,dE_s = \sigma^{\mathrm{ion}}(E).$$

$$\text{(A1.2)}$$

Laboratory measurements of secondary electron spectra were conducted by Opal *et al.* (1971) for a number of gases, including N_2 and O_2. Their results are in good agreement with Eq. (A1.1).

Since the primary electron loses energy $\Delta E = T + E_s$ in the same process, the production of the emerging primary electron at the energy $E_p = E - E_s - T$ can be described by the same cross section

$$\sigma^{\mathrm{deg}}(E \to E_p) = \sigma^{\mathrm{sec}}(E \to E_s). \tag{A1.3}$$

The energy E_s can be chosen to coincide with the energy grid and thus no adjustment for $\sigma^{\mathrm{sec}}(E \to E_s)$ is necessary. For the degraded primary, however, E_p will, in general, not be a grid point, if already fixed by E_s. Swartz (1985) and Stamnes (1978), therefore, suggested adjusting the primary degradation cross section according to a scheme similar to that adopted for the excitation cross sections.

Although the adjustment of the cross section guarantees energy conservation in the numerical calculation, it does not conserve the number of electrons. It is therefore advantageous to avoid the modification of the ionization cross sections. For the transport calculation individual electron collisions are of no consequence, allowing the following relaxation of the requirement of Eq. (A1.3)

$$\int_0^E \sigma^{\mathrm{deg}}(E \to E_p)\, dE_p = \int_0^E \sigma^{\mathrm{sec}}(E \to E_s)\, dE_s. \tag{A1.4}$$

Thus, σ^{deg} and σ^{sec} may be computed independently of one another on the discrete energy grid. Substituting $E - E_s - T$ for E_s in Eq. (A1.1) and Eq. (A1.2) with E_s chosen so that $E - E_s - T$ coincides with an energy grid cell yields the degradation cross section for the primary electron without any further modifications.

To ensure energy conservation in the energy degradation process, equations (A1.2) and (A1.4) must hold on the chosen energy grid with the integration method that is used by the degradation routine. For the calculation of the source term Q in the differential equation (Eq. 3.2), the integral over energy is replaced by a simple summation (Eq. 3.3b):

$$\int_E^\infty R(E' \to E)\, I(E')\, dE' = \sum_{i=n+1}^N R_{in} I(E_i) \Delta_i.$$

The intensity $I(E)$ is sampled at the center energy E_i of the energy grid cell and assumed to be constant over the width Δ_i of the energy cell. The index i refers to the source energy cell, while the index n refers to the sink energy cell. Applying the same sampling to the degradation function of Eq. (A1.1) for the source energy (E without index in Eq. (A1.1)), requires a careful calculation of the numerical value of $R_{in} = R(E_i \rightarrow E_n)$ to fulfill Eq. (A1.2) and (A1.4). Expressing the condition of Eq. (A1.2) on the discrete grid

$$\sum_{n=1}^{i} \sigma^{\mathrm{deg}}(E_i \rightarrow E_n)\Delta_n = \sigma^{\mathrm{ion}}(E_i),$$

it can be seen that the energy redistribution function must be calculated according to

$$R_{in} = \frac{1}{\Delta_n} \int_{E_n - \frac{\Delta_n}{2}}^{E_n + \frac{\Delta_n}{2}} R(E_i \rightarrow E)\, dE. \tag{A1.5}$$

The redistribution function R_{in} is the sum of σ^{sec}, σ^{deg}, and σ^{ex} and the method outlined above must be applied to all three components.

Especially for σ^{deg} and large incident energies the energy redistribution function (Eq. A1.1) shows rapid variation over a single energy grid cell. In order to evaluate the integral in Eq. (A1.5) several quadrature rules have been compared. The discretized forms of Eq. (A1.2) and (A1.4) are used as a criterion for the integration method. It was found that the double-exponential quadrature rule (Toda and Ono, 1982) is best suited for the integration of the function given by Eq. (A1.1). The sink energies for the production of secondary electrons (σ^{sec}) are at low energies where the energy grid has a high resolution and a trapezoid rule might suffice for the integration. For reasons of consistency, the same integration method as for σ^{deg} is applied. Only for the calculation of σ^{ex}, where the energy degradation is given by a δ-function, the numerical integration can be omitted. The spreading of electron intensity from a large energy source cell over several small energy sink cells as described in Fig. A1.2 by the Swartz method ensures energy conservation in the energy degradation process.

Appendix 2: Details of the Derivation of the Two Stream Equation

Starting with equations (3.4a) and (3.4b) it is first noted that τ is a function of energy. It proves to be advantageous to scale these equations such that the spatial variable becomes energy independent. This can be achieved by substituting $\tau_{ref} = \tau(E_{ref})$ for τ, where E_{ref} is some reference energy. The derivative of I with respect to τ is replaced by

$$\frac{\partial I}{\partial \tau} = \frac{\partial I}{\partial \tau_{ref}} \frac{d\tau_{ref}}{d\tau}$$

and equations (3.4a) and (3.4b) become

$$\pm \frac{\partial I^{\pm}}{\partial \tau_{ref}} = AI^{\pm} - BI^{\mp} - \tilde{Q}^{\pm}. \tag{A2.1}$$

The following definitions are applied:

$$A = \frac{\sin \alpha}{\bar{\mu}} \frac{d\tau_{ref}}{d\tau} \left(1 - \omega(1 - \beta)\right)$$

$$B = \frac{\sin \alpha}{\bar{\mu}} \frac{d\tau_{ref}}{d\tau} \omega\beta$$

$$\tilde{Q}^{\pm} = \frac{\sin \alpha}{\bar{\mu}} \frac{d\tau_{ref}}{d\tau} Q^{\pm}$$

and according to the definition of τ in Eq. (3.1) the normalization is:

$$\frac{d\tau_{ref}}{d\tau} = \frac{\sum_j \left(n_j(z)\sigma_j^{tot}(E_{ref}) + n_e(z)\Lambda(E_{ref})\right)}{\sum_j \left(n_j(z)\sigma_j^{tot}(E) + n_e(z)\Lambda(E)\right)}.$$

Resolving Eq. (A2.1) for I^+ in terms of I^- gives

$$I^+ = \frac{1}{B}\left(AI^- + \frac{\partial I^-}{\partial \tau_{ref}} - \tilde{Q}^-\right).$$

This is inserted into Eq. (A2.1) to eliminate I^+:

$$\frac{\partial}{\partial \tau_{ref}}\left[\frac{1}{B}\left(AI^- + \frac{\partial I^-}{\partial \tau_{ref}} - \tilde{Q}^-\right)\right] = \frac{A}{B}\left(AI^- + \frac{\partial I^-}{\partial \tau_{ref}} - \tilde{Q}^-\right) - BI^- - \tilde{Q}^+.$$

118

Ordering the terms with respect to the derivatives of I^- and writing $()'$ for $\frac{\partial}{\partial \tau_{ref}}$ gives:

$$\frac{1}{B}(I^-)'' + \left(\frac{A}{B} + \left(\frac{1}{B}\right)' - \frac{A}{B}\right)(I^-)' + \left(\left(\frac{A}{B}\right)' - \frac{A^2}{B} + B\right)I^- = \left(\frac{\tilde{Q}^-}{B}\right)' - \frac{A}{B}\tilde{Q}^- - \tilde{Q}^+.$$

With the definitions

$$a_1(\tau) = B\left(\frac{1}{B}\right)' = -\frac{1}{B}\frac{\partial B}{\partial \tau_{ref}}$$

$$a_2(\tau) = B^2 - A^2 + \frac{\partial A}{\partial \tau_{ref}} + a_1 A$$

$$\gamma(\tau) = -B\tilde{Q}^+ - A\tilde{Q}^- + \frac{\partial \tilde{Q}^-}{\partial \tau_{ref}} + a_1\tilde{Q}^-$$

we arrive at equation (3.5).

References

Aarts, J. F. M. and F. J. de Heer, Emission Cross Sections for OI and OII Multiplet Radiation Produced by Electron Impact on O_2, *Physica*, **56**, 294, 1971.

Ajello, J. M., Dissociative Excitation of O_2 in the Vacuum Ultraviolet by Electron Impact, *J. Chem. Phys.*, **55**, 3156, 1971.

Ajello, J. M. and D. E. Shemansky, A Re-Examination of Important N_2 Cross Sections by Electron Impact with Application to the Dayglow: The Lyman-Birge-Hopfield Band System and NI (119.99 nm), *J. Geophys. Res.*, **90**, 9845, 1985.

Andrick, D. and A. Bitsch, Experimental Investigation and Phase Shift Analysis of Low-Energy Electron-Helium Scattering, *J. Phys. B*, **8**, 393, 1975.

Banks, P. M., Collision Frequencies and Energy Transfer: Electrons, *Planet. Space Sci.*, **14**, 1085, 1966.

Banks, P. M. and A. F. Nagy, Concerning the Influence of Elastic Scattering Upon Photoelectron Transport and Escape, *J. Geophys. Res.*, **75**, 1902, 1970.

Banks, P. M., C. R. Chappell, and A. F. Nagy, A New Model for the Interaction of Auroral Electrons With the Atmosphere: Spectral Degradation, Backscatter, Optical Emission, and Ionization, *J. Geophys. Res.*, **79**, 1459, 1974.

Berger, M. J., S. M. Seltzer, and K. Maeda, Energy Deposition by Auroral Electrons in the Atmosphere, *J. Atmos. Terr. Phys.*, **32**, 1015, 1970.

Birkeland, K., Expédition Norvégienne de 1899-1900 pour l'étude des aurores boréalis, *Vid. Selsk. Skr. Math. Nat. Kl.*, **1**, 1901.

Borst, W. L. and E. C. Zipf, Cross Section for Electron Impact Excitation of the (0,0) First Negative Band of N_2^+ from Threshold to 3 keV, *Phys. Rev. A*, **1**, 834, 1970.

Burnett, T. and S. P. Rountree, Differential and Total Cross Sections for Electron-Impact Ionization of Atomic Oxygen, *Phys. Rev. A*, **20**, 1468, 1979.

Cartwright, D. C., S. Trajmar, A. Chutjian, and W. Williams, Electron Impact Excitation of the Electronic States of N_2. II. Integral Cross Sections at Incident Energies from 10 to 50 eV, *Phys. Rev. A*, **16**, 1041, 1977.

Chandrasekhar, S., Radiative Transfer, 393 pp., Dover Publications, New York, 1960.

Christensen, A. B., L. R. Lyons, J. H. Hecht, G. G. Sivjee, R. R. Meier, and D. G. Strickland, Magnetic Field-Aligned Electric Field Acceleration and the Characteristics of the Optical Aurora, *J. Geophys. Res.*, **92**, 6163, 1987.

Dalgarno, A. and G. W. Griffing, Energy per Ion Pair for Electron and Proton Beams in Atomic Hydrogen, *Proc. Roy. Soc. A*, **248**, 415, 1958.

Dawydow, A. S., Quantenmechanik, 4. edition, 673 pp., VEB Deutscher Verlag der Wissenschaften, Berlin, 1974.

Degen, V., DIALUP Facility for Generating Auroral and Airglow Synthetic Spectra, *Report Geophys. Inst. Univ. Alaska*, UAG R-305, 1986.

Duderstadt, J. J. and W. R. Martin, Transport Theory, 613 pp., Wiley, New York, 1979.

de Heer, F. J. and R. H. J. Jansen, Total Cross Sections for Electron Scattering by He, *J. Phys. B*, **10**, 3741, 1977.

Eather, R. H. and S. B. Mende, Systematics in Auroral Energy Spectra, *J. Geophys. Res*, **77**, 660, 1972.

Evans, D. S., Precipitating Electron Fluxes Formed by a Magnetic Field-Aligned Potential Difference, *J. Geophys. Res.*, **79**, 2853, 1974.

Filippelli, A. R., F. A. Sharpton, C. C. Lin, and R. E. Murphy, Production of Atomic Nitrogen Emission by Electron-Impact Dissociative Excitation of Nitrogen Molecules, *J. Chem. Phys.*, **76**, 3597, 1982.

Fite, W. L. and R. T. Brackmann, Collisions of Electrons With Hydrogen Atoms I. Ionization, *Phys. Rev.*, **112**, 1141, 1958.

Fite, W. L., R. F. Stebbings, and R. T. Brackmann, Collision of Electrons With Hydrogen Atoms IV. Excitation of Lyman-Alpha Radiation Near Threshold, *Phys. Rev.*, **116**, 356, 1959.

Frank, L. A., J. D. Craven, K. L. Ackerson, M. R. English, R. H. Eather, and R. L. Carovillano, Global Auroral Imaging Instrumentation for the Dynamics Explorer Mission, *Space Sci. Instrum.*, **5**, 369, 1981.

Gattinger, R. L. and A. Vallance Jones, The Intensity Ratios of Auroral Emission Features, *Ann. Géophys.*, **28**, 91, 1972.

Goody, R. M., Atmospheric Radiation, I Theoretical Basis, 436 pp., Oxford University Press, London, 1964.

Gradshteyn, I. S. and I. M. Ryzhik, Table of Integrals, Series, and Products, 4. edition, 1086 pp., Academic Press, New York, 1965.

Green, A. E. S. and R. S. Stolarski, Analytic Models of Electron Impact Excitation Cross Sections, *J. Atmos. Terr. Phys.*, **34**, 1703, 1972.

Haasz, A. A. and J. H. DeLeeuw, Effective Electron Impact Excitation Cross Sections for N_2, O_2, and O_1, *J. Geophys. Res.*, **81**, 4031. 1976.

Hake, R. D. and A. V. Phelps, Momentum-Transfer and Inelastic-Collision Cross Sections for Electrons in O_2, CO, and CO_2, *Phys. Rev.*, **158**, 70, 1967.

Hasted, J. B., Physics of Atomic Collisions, second edition, 773 pp., American Elsevier Publishing Company, New York, 1972.

Hedin, A. E., A Revised Thermospheric Model Based on Mass Spectrometer and Incoherent Scatter Data: MSIS-83, *J. Geophys. Res.*, **88**, 10170, 1983.

Hedin, A. E., MSIS-86 Thermospheric Model, submitted to J. Geophys. Res., 1986.

Heelis, R. A., J. K. Lowell, and R. W. Spiro, A Model of the High-Latitude Ionospheric Convection Pattern, *J. Geophys. Res.*, **87**, 6339, 1982.

Hoegy, W. R., New Fine Structure Cooling Rate, *Geophys. Res. Lett.*, **3**, 541, 1976.

Hofstadter, D. R., Gödel, Escher, Bach: An Eternal Golden Braid, 777pp., Random House Inc., New York, 1980.

Holland, R. F. and W. B. Maier II, Study of the $A \rightarrow X$ Transitions in N_2^+ and CO^+, *J. Chem. Phys.*, **56**, 1972.

Holt, H. K. and R. Krotkov, Excitation of n=2 States in Helium by Electron Bombardment, *Phys. Rev.*, **144**, 82, 1966.

Itikawa, Y. and O. Aono, Energy Change of a Charged Particle Moving in a Plasma, *Physics Fluids*, **9**, 1259, 1966.

Jacchia, L. G., Thermospheric Temperature, Density, and Composition: New Models, *Spec. Rep.*, **375**, Smithonian Astrophys. Observ., Cambridge, Mass., 1977.

Jobe, J. D. and R. M. St.John, Absolute Measurements of the 2^1P and 2^3P Electron Excitation Cross Sections of Helium Atoms, *Phys. Rev.*, **164**, 117, 1967.

Julienne, P. S. and J. Davis, Cascade and Radiation Trapping Effects on Atmospheric Atomic Oxygen Emission Excited by Electron Impact, *J. Geophys. Res.*, **81**, 1397, 1976.

Kasting, J. F. and P. B. Hays, A Comparison between N_2^+ 4278 Å Emission and Electron Flux in the Auroral Zone, *J. Geophys. Res.*, **82**, 3319, 1977.

Kusida, K. and H. Kamiyama, Discrete Ordinate Solutions of the Transport Equation for Auroral Electrons, in: Proceedings of the Seventh Symposium on Coordinated Observations of the Ionosphere and the Magnetosphere in the Polar Regions, edited by T. Nagata and N. Sato, pp. 345–353, National Institute of Polar Research, Tokyo, 1985.

Lanchester, B. S. and M. H. Rees, Field-Aligned Current Reversals and Fine Structure in a Dayside Auroral Arc, *Planet. Space Sci.*, **35**, 759, 1987.

Lawton, S. A. and A. V. Phelps, Excitation of the $b^1\Sigma_g^+$ State of O_2 by Low Energy Electrons, *J. Chem. Phys.*, **69**, 1055, 1978.

LeDourneuf, M. and R. K. Nesbet, Electron Impact Excitation of Fine-Structure Levels of Atomic Oxygen, *J. Phys. B*, **9**, L241, 1976.

Lejeune, G. and F. Wormser, Diffusion of Photoelectrons Along a Field Line Inside the Plasmasphere, *J. Geophys. Res.*, **81**, 2900, 1976.

Linder, F. and H. Schmidt, Experimental Study of Low Energy e-O_2 Collision Processes, *Z. Naturforsch.*, **26**, 1617, 1971.

Mahan, A. H., A. Gallagher, and S. J. Smith, Electron Impact Excitation of the ^3S, ^3P, and ^3D States of H, *Phys. Rev. A*, **13**, 156, 1976.

Märk, T. D., Cross Section for Single and Double Ionization of N_2 and O_2 Molecules by Electron Impact from Threshold up to 170 eV, *J. Chem. Phys.*, **63**, 3731, 1975.

Meier, R. R. and J.-S. Lee, An Analysis of the OI 1304 Å Dayglow Using a Monte Carlo Resonant Scattering Model with Partial Frequency Redistribution, *Planet. Space Sci.*, **30**, 439, 1982.

Meier, R. R., R. R. Conway, D. E. Anderson, Jr., P. D. Feldman, R. W. Eastes, E. P. Gentieu, and A. B. Christensen, The Ultraviolet Dayglow at Solar Maximum, 3. Photoelectron-Excited Emissions of N_2 and O, *J. Geophys. Res.*, **90**, 6608, 1985.

Mende, S. B., R. H. Eather, M. H. Rees, R. R. Vondrak, and R. M. Robinson, Optical Mapping of Ionospheric Conductances, *J. Geophys. Res.*, **89**, 1755, 1984.

Metzger, P. H. and G. R. Cook, A Reinvestigation of the Absorption Cross Sections of Molecular Oxygen in the 1050–1800 Å Region, *J. Quant. Spectrosc. Radiat. transfer*, **4**, 107, 1964.

Nagy, A. F. and P. M. Banks, Photoelectron Fluxes in the Ionosphere, *J. Geophys. Res.*, **75**, 6260, 1970.

Nagy, A. F., E. G. Fontheim, R. S. Stolarski, and A. E. Beutler, Ionospheric Electron Temperature Calculations Including Protonospheric and Conjugate Effects, *J. Geophys. Res.*, **74**, 4667, 1969.

Nicholson, D. R., Introduction to Plasma Theory, 292 pp., John Wiley & Sons, New York, 1983.

Opal, C. B., W. K. Peterson, and E. C. Beaty, Measurements of Secondary-Electron Spectra Produced by Electron Impact Ionization of a Number of Simple Gases, *J. Chem Phys.*, **55**, 4100, 1971.

Opal, C. B., E. C. Beaty, and W. K. Peterson, Tables of Secondary Electron-Production Cross Sections, *Atomic Data*, 4, 209, 1972.

Pitchford, L. C. and A. V. Phelps, Comparative Calculations of Electron-Swarm Properties in N_2 at Moderate E/N Values, *Phys. Rev. A*, 25, 540, 1982.

Pulliam, D. M., H. R. Anderson, K. Stamnes, and M. H. Rees, Auroral Electron Acceleration and Atmospheric Interactions, *J. Geophys. Res.*, 86, 2397, 1981.

Rairden, R. L., L. A. Frank, and J. D. Craven, Geocoronal Imaging With Dynamics Explorer, *J. Geophys. Res.*, 91, 13613, 1986.

Rapp, D. and P. Englander-Golden, Total Cross Sections for Ionization and Attachment in Gases by Electron Impact. I. Positive Ionization, *J. Chem. Phys.*, 43, 1464, 1965.

Rees, M. H., Absolute Photometry in the Aurora–I The Ionized Molecular Nitrogen Emission and the Oxygen Green Line in the Dark Atmosphere, *J. Atmos. Terr. Phys.*, 14, 325, 1958.

Rees, M. H., Auroral Ionization and Excitation by Incident Energetic Electrons, *Planet. Space Sci.*, 11, 1209, 1963.

Rees, M. H. and V. J. Abreu, Auroral Photometry From the Atmospheric Explorer Satellite, *J. Geophys. Res.*, 89, 317, 1984.

Rees, M. H. and D. Luckey, Auroral Electron Energy Derived From Ratio of Spectroscopic Emissions 1. Model Computations, *J. Geophys. Res.*, 79, 5181, 1974.

Rees, M. H. and R. G. Roble, Excitation of $O(^1D)$ Atoms in Aurorae and Emission of the [OI] 6300-Å Line, *Can. J. Phys.*, 64, 1608, 1986.

Rees, M. H., A. I. Stewart, and J. C. G. Walker, Secondary Electrons in Aurora, *Plant. Space Sci.*, 17, 1997, 1969.

Rees, M. H., A. I. Stewart, W. E. Sharp, P. B. Hays, R. A. Hoffman, L. H. Brace, J. P. Doering, and W. K. Peterson, Coordinated Rocket and Satellite Measurements of an Auroral Event, 1. Satellite Observations and Analysis, *J. Geophys. Res.*, 82, 2250, 1977.

Robinson, R. M., R. R. Vondrak, K. Miller, T. Dabbs, and D. Hardy, On Calculating Ionospheric Conductances From the Flux and Energy of Precipitating Electrons, *J. Geophys. Res*, 92, 2565, 1987.

Roble, R. G., B. A. Emery, R. E. Dickinson, E. C. Ridley, T. L Killeen, P. B. Hays, and G. R. Carignan, Thermospheric Circulation, Temperature, and Compositional Structure of the Southern Hemisphere Polar Cap During October-November 1981, *J. Geophys. Res.*, 89, 9057, 1984.

Rottmann, K., Mathematische Formelsammlung, 2. Auflage, 174 pp., BI Wissenschafts-verlag, Mannheim, 1960.

Schunk, R. W. and P. B. Hays, Photoelectrons Energy Losses to Thermal Electrons, *Planet. Space Sci.*, **19**, 113, 1971.

Schunk, R. W., P. B. Hays, and Y. Itikawa, Energy Losses of Low-Energy Photoelectrons to Thermal Electrons, *Planet. Space Sci.*, **19**, 125, 1971.

Schunk, R. W., J. J. Soyka, and M. D. Bowline, Theoretical Study of the Electron Temperature in the High-Latitude Ionosphere for Solar Maximum and Winter Conditions, *J. Geophys. Res.*, **91**, 12041, 1986.

Sharp, W. E., Reply, *Planet. Space Sci.*, **34**, 393, 1986.

Sharp, W. E., M. H. Rees, and A. I. Stewart, Coordinated Rocket and Satellite Measurements of an Auroral Event, 2. The Rocket Observation and Analysis, *J. Geophys. Res.*, **84**, 1977, 1979.

Shettle, E. P. and J. A. Weinman, The Transfer of Solar Irradiance Through Inhomogeneous Turbid Atmospheres Evaluated by Eddignton's Approximation, *J. Atmos. Sci.*, **27**, 1048, 1970.

Shyn, T. W. and W. E. Sharp, Differential Excitation Cross Section of Atomic Oxygen by Electron Impact: (^{3}P–^{1}D Transition), *J. Geophys. Res.*, **91**, 1691, 1986.

Shyn, T. W., S. Y. Cho, and W. E. Sharp, Differential Excitation Cross Section of Atomic Oxygen by Electron Impact: (^{3}P–^{1}S Transition), *J. Geophys. Res.*, **91**, 13751, 1986.

Spence, D. and G. J. Schulz, Vibrational Excitation by Electron Impact in O_2, *Phys. Rev. A*, **2**, 1802, 1970.

Stamnes, K., Analytic Approach to Photoelectron Transport: Extension of Stolarski's (1972) Work, *J. Geophys. Res.*, **82**, 2391, 1977.

Stamnes, K., A Theoretical Investigation of the Interaction of Auroral Electrons with the Atmosphere, 219 pp., Ph.D. Thesis, University of Colorado, 1978.

Stamnes, K., Analytic Approach to Auroral Electron Transport and Energy Degradation, *Planet. Space Sci.*, **28**, 427, 1980.

Stamnes, K., On the Two-Stream Approach to Electron Transport and Thermalization, *J. Geophys. Res.*, **86**, 2405, 1981a.

Stamnes, K., Electron Transport and Energy Degradation: On the Numerical Solution of the Two-Stream Equations, *Sci. Report Geophys. Inst. Univ. Alaska*, UAG R-286, 1981b.

Stamnes, K., Multiple Scattering and Radiative Transfer in Planetary Atmospheres, *Mathematics Reports*, Institute of Mathematical and Physical Sciences, University of Tromsø, Norway, 1985a.

Stamnes, K., A Unified Theory of Interhemispheric Electron Transport and Energy Degradation, *Geophysica Norvegica*, **33**, 41, 1985b.

Stamnes, K., The Theory of Multiple Scattering of Radiation in Plane Parallel Atmospheres, *Rev. Geophys.*, **24**, 299, 1986.

Stamnes, K. and P. Conklin, A New Multi-Layer Discrete Ordinate Approach to Radiative Transfer in Vertically Inhomogeneous Atmospheres, *J. Quant. Spectrosc. Radiat. Transfer*, **31**, 273, 1984.

Stamnes, K. and M. H. Rees, Inelastic Scattering Effects on Photoelectron Spectra and Ionospheric Electron Temperature, *J. Geophys. Res.*, **88**, 6301, 1983.

Stamnes, K. and R. A. Swanson, A New Look at the Discrete Ordinate Method for Radiative Transfer Calculations in Anisotropically Scattering Atmospheres, *J. Atmos. Sci.*, **38**, 387, 1981.

Stamnes K. and G. Witt, The Effect of Light Scattering and Diffusive Reflection on Atmospheric Spectral Measurements, in: Proc. 13th Annual Meeting on Atmospheric Studies by Optical Methods, Oslo, Aug. 1985, in press, 1987.

Stamnes, K., W. J. Wiscombe, S. C. Tsay, and K. Jayaweera, An Improved, Numerically Stable Multiple Scattering Algorithm for Discrete-Ordinate-Method Radiative Transfer in Scattering and Emitting Layered Media, submitted to **Appl. Optics**, 1987.

St.John, R. M., F. L. Miller, and C. C. Lin, Absolute Electron Excitation Cross Sections of Helium, *Phys. Rev.*, **134**, A888, 1964.

Stone, E. J. and E. C. Zipf, Electron-Impact Excitation of the $^3S^0$ and $^5S^0$ States of Atomic Oxygen, *J. Chem. Phys.*, **60**, 4237, 1974.

Störmer, C., Polar Aurora, 438 pp., Oxford University Press, London, 1955.

Strickland, D. J. and D. E. Anderson, Jr., The OI 1304-Å Nadir Intensity/Column Production Rate Ratio and Its Application to Airglow Studies, *J. Geophys. Res.*, **82**, 1013, 1977.

Strickland, D. J. and P. C. Kepple, Preliminary Report on the Transport and Production of Energetic Electrons in Auroras, *NRL Memorandum Report*, **2779**, 1974.

Strickland, D. J., D. L. Book, T. P. Coffey, and J. A. Fedder, Transport Equation Techniques for the Deposition of Auroral Electrons, *J. Geophys. Res.*, **81**, 2755, 1976.

Strickland, D. J., J. R. Jasperse, and J. A. Whalen, Dependence of Auroral FUV Emissions on the Incident Electron Spectrum and Neutral Atmosphere, *J. Geophys. Res.*, **88**, 8051, 1983.

Swartz, W. E., Optimization of Energetic Electron Energy Degradation Calculations, *J. Geophys. Res.*, **90**, 6587, 1985.

Swartz, W. E., J. S. Nisbet, and A. E. S. Green, Analytic Expression for the Energy-Transfer Rate from Photoelectrons to Thermal-Electrons, *J. Geophys. Res.*, **76**, 8425, 1971.

Sykes, J. B., Approximate Integration of the Equation of Transfer, *Mon. Not. Roy. Astron. Soc.*, **111**, 377, 1951.

Tachibana, K. and A. V. Phelps, Excitation of the $C^3\Pi_u$ State of N_2 by Low Energy Electrons, *J. Chem. Phys.*, **71**, 3544, 1979.

Takayanagi, K. and Y. Itikawa, Elementary Processes Involving Electrons in the Ionosphere, *Space Sci. Rev.*, **11**, 380, 1970.

Toda, H. and H. Ono, A Topic in Numerical Analysis: Notes on Effective Usage of Double Exponential Formulae for Numerical Integration, (in Japanese) *Butsuri (Phys. Soc. of Japan)*, **37**, 8, 1982.

Trajmar, S., D. C. Cartwright, and W. Williams, Differential and Integral Cross Sections for the Electron-Impact Excitation of the $a^1\Delta_g$ and $b^1\Sigma_g^+$ States of O_2, *Phys. Rev. A*, **4**, 1482, 1971.

Trajmar, S., W. Williams, and A. Kuppermann, Angular Dependence of Electron Impact Excitation Cross Sections of O_2, *J. Chem. Phys.*, **56**, 3759, 1972.

Tsay, S. C., Numerical Study of the Atmospheric Radiative Transfer Process with Application to the Arctic Energy Balance, 251 pp., Ph.D. Thesis, University of Alaska, Fairbanks, 1986.

Valentine, J. M. and S. C. Curran, Average Energy Expenditure per Ion Pair in Gases and Gas Mixtures, *Rep. Prog. Phys.*, **21**, 1, 1958.

Vallance Jones, A., Aurora, 301 pp., D. Reidel Publishing Co., Dordrecht-Holland, 1974.

Volland, H., A Model of the Magnetospheric Electric Field Convection Pattern, *J. Geophys. Res.*, **83**, 2695, 1978.

Watson, C. E., V. A. Dulock, Jr., R. S. Stolarski, and A. E. S. Green, Electron Impact Cross-Sections for Atmospheric Species, 3. Molecular Oxygen, *J. Geophys. Res.*, **72**, 3961, 1967.

Wedde, T., Scattering Cross Sections—a Compilation of O, O_2, and N_2 Data between 1 and 1000 eV. I. Elastic Scattering, *Utah State University Report*, CRA 76-1, 1976.

Wedde, T. and T. G. Strand, Scattering Cross Sections for 40 eV to 1 keV Electrons Colliding Elastically with Nitrogen and Oxygen, *J. Phys. B*, 7, 1091, 1974.

Wingerden, B. van, E. Weigold, F. J. de Heer, and K. J. Nygaard, Elastic Scattering of Electrons by Molecular and Atomic Hydrogen, *J. Phys. B*, 10, 1345, 1977.

Winningham, J. D., J. L. Burch, N. Eaker, V. A. Blevins, and R. A. Hoffman, The Low Altitude Plasma Instrument (LAPI), *Space Sci. Instrum.*, 5, 465, 1981.

Williams, J. F., Electron Scattering from Atomic Hydrogen III. Absolute Differential Cross Sections for Elastic Scattering of Electrons of Energies from 20 to 680 eV, *J. Phys. B*, 8, 2191, 1975.

Williams, J. F. and B. A. Willis, Electron Scattering from Atomic Hydrogen I. Differential Cross Sections for Excitation of n=2 States, *J. Phys. B*, 8, 1641, 1975.

Wiscombe, W. J., The Delta-M Method: Rapid Yet Accurate Radiative Flux Calculations for Strongly Asymmetric Phase Functions, *J. Atmos. Sci.*, 34, 1408, 1977.

Wong, S. F., M. J. W. Boness, and G. J. Schulz, Vibrational Excitation of O_2 by Electron Impact Above 4 eV, *Phys. Rev. Lett.*, 31, 969, 1973.

Zipf, E. C. and P. W. Erdman, Electron-Impact Excitation of Atmospheric Oxygen: Revised Cross Section Values, *EOS*, 66, 321, 1985.

Zipf, E. C. and R. W. McLaughlin, On the Dissociation of Nitrogen by Electron Impact and by E.U.V. Photo-Absorption, *Planet. Space Sci.*, 26, 449, 1978.

Zipf, E. C., W. W. Kao, and P. W. Erdman, On the Simultaneous Ionization-Excitation of the OII(λ834Å) Resonance Transition by Electron Impact on Atomic Oxygen, *Planet. Space Sci.*, 33, 1309, 1985.